EPFL

Composition and Interface Engineering of High Performing Perovskite Solar Cells

Mousa Abdulla M E ABUHELAIQA

■ École
polytechnique
fédérale
de Lausanne

2022
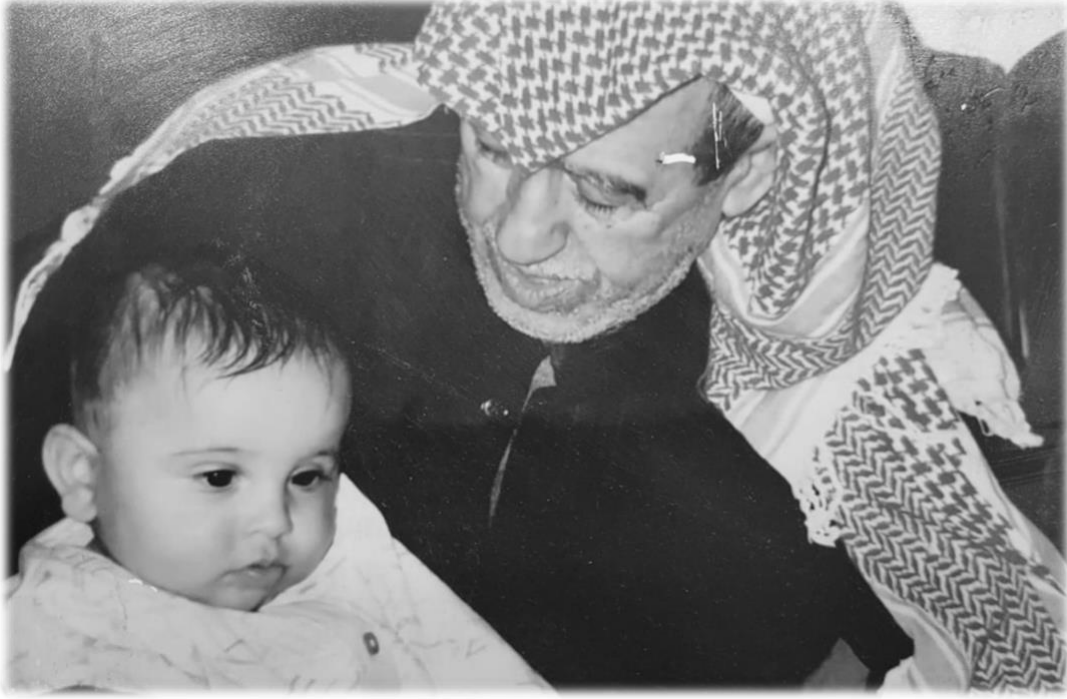
To my grandfather who has given me the gift of opportunity, I have inherited your name, and today I am a living proof of your legacy.

إلى جدي الذي منحني هذه الفرصة ، لقد ورثت اسمك ، واليوم أنا دليل حي على إرثك.

Acknowledgements

Alwani Rafieh and Pavel Culik. I am humbled to have met, exchanged conversations, and shared the laboratory space with all of you.

I must further acknowledge the support I received from individuals in Switzerland and in other parts of the world. Moiz Bohra, the one friend I got to bring with me from Qatar to London and now Switzerland, I am very thankful to have shared many experiences and GoPro adventures with you. I hope you are not still regretting the hike we had in Zermatt and the McDo afterwards. Anja Wettstein, thank you for inviting me for meals and yoga lessons with your family in Zurich, and for sharing with me your signature spaghetti Bolognese recipe. Thank you, Florence Gachaud, for being a reliable French teacher and for helping me translate the abstract section of the thesis. Thank you, Abdulrahaman Al-Malki, for being present in all phases of my PhD despite the distance, as you put it, "the strength of a bond is determined by the proximity and valence electrons." Thank you, Frank Tuschling, for your utmost support, especially in the last couple of days leading to my defence, you had given me the greatest gift.

Finally, a very big and heartfelt thank you to my family for their consistent and unconditional love and support. My dear parents, Abdulla Abuhelaiqa and Wedad Abuhelaiqa, thank you for all the times you picked me from and took me to Hamad International Airport, seeing you at the beginning and end of every Qatar trip brought me a lot of joy. Thank you, my dear sister Laila Abuhelaiqa, for all the cappuccinos we shared in Costa Coffee, I look forward to having one with you soon. My dear siblings, Essa Abuhelaiqa and Maryam Abuhelaiqa, the accomplishments you made were an inspiration behind this PhD, now this makes us even. My dear brothers, Ali Abuhelaiqa and Mohammed Abuhelaiqa, thank you for keeping contact on Saturday mornings, it was comforting to hear familiar voices from home every now and then.

To all the names I have mentioned, I have been touched by you in one way or another, and for that, I thank you once more for contributing towards my scientific and personal growth. I may not be geographically close in my next steps, but I look, very much, to hear from you sooner than later.

Rue de l'industrie 17, Sion
November 10th, 2021

Abstract

Perovskite solar cells have been established as a disruptive technology in the domain of photovoltaics. Their facile, low-temperature processing and high-power conversion efficiency make them stand-out among other mature solar technologies. The performance of perovskite solar cells is profoundly tied to an interplay of material properties of singular thin films that are assembled to form the photovoltaic device stack. An understanding of optoelectronic, morphological, and other key characteristics of each layer and its interfaces is instrumental in advancing the science of perovskite solar cells. Since their inception after just over a decade, much work on perovskite solar cell has been stagnant to bring the technology to the market. The long-term stability remains foremostly the main hindrance to facilitating technology transfer. Therefore, the work presented in this thesis explores multiple interface and compositional approaches to promote stability and other photovoltaic parameters of perovskite solar cells.

In the second chapter of the thesis, a light-soaking exploration was done on perovskite samples that utilize single (TiO_2 and SnO_2) and bilayered (TiO_2/SnO_2) electron transporting materials. The work aims to expand consensus on the optoelectronic and morphological features of light-soaked samples and link them with long-term stability. Upon preliminary testing, maximum power point tracking on each sample reveals efficiency preservation of SnO_2 and TiO_2/SnO_2 samples over the course of 1000 hours while prominent degradation was revealed for the TiO_2 sample. On a secondary investigation, light-soaking characterizations were performed where fresh and light-soaked samples were characterized to obtain photoluminescence, microscopic, and crystallographic features. The work reveals the added benefit of employing TiO_2/SnO_2 transporting bilayers to improve both the stability and power conversion efficiency of a perovskite solar cell.

Building on an effort to understand TiO_2/SnO_2 bilayer behaviors, the third chapter investigates the role of halide passivating elements in SnO_2 on the performance of perovskite solar cells. The study utilizes three metalorganic precursors based on acetylacetone complexes with chloride and bromide groups to fabricate SnO_2 layers at different annealing temperatures. Upon thermal and elemental investigations, the study clearly links the presence of amorphous halide elements in SnO_2 to the power conversion efficiency of perovskite solar cells. More-in-depth, the optimal SnO_2 annealing temperature for bromide containing samples 220 °C compared with 200 °C for chloride containing samples. The higher temperature tolerance tendency was correlated to bromide's lower

sublimation sensitivity. Overall, the study highlights the importance of amorphous passivating elements in SnO_2 for high performing planar perovskite solar cells.

Finally, the fourth chapter involves a novel cation mixing approach for 2D perovskites at the interface of the 3D perovskite and the hole transporting layer. Alkyl ammonium halides have been widely used to form light-stable 2D perovskite films upon interaction with excess PbI_2. In this study, different alkyl chain cations (propylammonium iodide and octylammonium iodide) were mixed in one solution to form a novel 2D perovskite crystal lattice. Photoluminescence and x-ray diffraction spectroscopy investigations reveal a unique crystal lattice and a uniform quasi-2D state (n = 2) for the mixed 2D perovskite samples, properties which are not found in singular propylammonium iodide and octylammonium iodide 2D samples. Moreover, the mixed 2D samples possessed superior power conversion efficiency and long-term performance. The study highlights the potential of mixing two cations in 2D perovskite layers to promote stability.

Keywords

Résumé

Les cellules solaires à pérovskite se sont imposées comme une technologie de rupture dans le domaine du photovoltaïque. Leurs traitements faciles à basse température et leur efficacité de conversion à haute puissance les distinguent des autres technologies solaires existantes. Les performances des cellules solaires à pérovskite sont profondément liées à l'interaction des propriétés d'uniques couches minces qui ensemble forment la pile de dispositifs photovoltaïques. Une compréhension des caractéristiques optoélectroniques et morphologiques (entre autres) de chaque couche et de ses interfaces est essentielle pour faire avancer la science des cellules solaires à pérovskite. Depuis leur création après un peu plus d'une décennie, de nombreux travaux sur les cellules solaires à pérovskite stagnent pour amener la technologie sur le marché. La stabilité à long terme reste avant tout le principal frein pour faciliter le transfert de cette technologie. Par conséquent, le travail présenté dans cette thèse explore les multiples approches compositionnelles et interfaciales pour favoriser la stabilité ainsi que d'autres paramètres photovoltaïques des cellules solaires à pérovskite.

Dans le premier travail présenté, une exploration par trempage de lumière a été réalisée sur des échantillons de pérovskite utilisant des matériaux de transport d'électrons simples (TiO_2 et SnO_2) et bicouches (TiO_2/SnO_2). Le travail vise à élargir le consensus sur les caractéristiques optoélectroniques et morphologiques des échantillons imprégnés de lumière et à les lier à la stabilité à long terme. Lors des tests préliminaires, le suivi du point de puissance maximal sur chaque échantillon révèle une préservation de l'efficacité des échantillons de SnO_2 et TiO_2/SnO_2 au cours de 1000 heures tandis qu'une dégradation importante a été révélée pour l'échantillon de TiO_2. Lors d'une analyse secondaire, des échantillons frais et imbibés de lumière ont été caractérisés pour obtenir des propriétés photoluminiques, microscopiques et cristallographiques. Le travail révèle l'avantage supplémentaire de l'utilisation de bicouches de transport TiO_2/SnO_2 pour améliorer à la fois la stabilité et l'efficacité de conversion de puissance d'une cellule solaire à pérovskite.

S'appuyant sur les efforts déployés pour comprendre les comportements des bicouches TiO_2/SnO_2, le deuxième travail étudie le rôle des éléments de passivation aux halogénures dans le SnO_2 sur les performances des cellules solaires à pérovskite. L'étude utilise deux précurseurs organométalliques basés sur des complexes d'acétylacétone avec des groupes chlorure et bromure pour fabriquer des couches de SnO_2 à différentes températures de recuit. Lors d'analyses

thermiques et élémentaires, l'étude identifie clairement les modèles de présence d'halogénures par rapport à l'efficacité de conversion de puissance des cellules solaires à pérovskite. En conséquence , la température optimale de recuit SnO2 pour les échantillons contenant du bromure est de 250 °C contre 220 °C pour les échantillons contenant du chlorure. La tendance à la tolérance à la température plus élevée s'explique par la sensibilité inférieure à la sublimation du bromure. Dans l'ensemble, cette deuxième étude met en évidence l'importance des éléments de passivation amorphes dans le SnO_2 pour les cellules solaires à pérovskite à haute performance.

Enfin, le dernier travail implique une nouvelle approche de mélange de cations pour les pérovskites 2D à l'interface de la pérovskite 3D et de la couche de transport de trous. Les halogénures d'alkylammonium ont été largement utilisés pour former des films de pérovskite 2D stables à la lumière lors du interaction avec PbI_2 excès. Dans cette étude, différents cations de chaîne alkyle (iodure de propylammonium et iodure d'octylammonium) ont été mélangés dans une solution pour former un nouveau réseau cristallin de pérovskite 2D. Les études de photoluminescence et de spectroscopie de diffraction des rayons X révèlent un réseau cristallin unique et un état quasi-2D uniforme (n = 2) pour les échantillons de pérovskite 2D mixtes, propriétés qui ne sont pas trouvées dans les échantillons singuliers d'iodure de propylammonium et d'iodure d'octylammonium 2D. De plus, les échantillons 2D mixtes présentent une efficacité de conversion de puissance supérieure ainsi que des performances à long terme.

Mots-clés

Transport de charge, couches de transport d'électrons, ingénierie d'interface, pérovskites 2D à cations mixtes, passivation, cellules solaires à pérovskite, photovoltaïque, efficacité de conversion de puissance, énergie solaire, stabilité, pérovskites bidimensionnelles.

Contents

List of Figures

List of Tables

List of Symbols and Abbreviations

AM	Air mass
BETL	Bilayered electron transporting layer
BF	Bright field
c	Speed of light constant
c-TiO$_2$	Compact TiO$_2$
CdTe	Cadmium telluride solar cells
CIGS	Cadmium indium gallium selenide solar cells
DF	Dark field
$\frac{dn}{dt}$	Rate of charge carrier density with respect to time
DSSC	Dye synthesized solar cell
e^-	Negatively charged electron carrier
E_a	Electron acceptor state
E_{bg}	Bandgap energy
E_d	Electron donor state
EDXS	Energy dispersive x-ray spectrometry
E_p	Energy of a photon
E_f	Fermi Energy
ETL	Electron transporting layer
FF	Fill factor
FTO	Fluorine doped tin oxide
h	Plank constant
h^+	Positively charged hole carrier
HAADF	High-angle annular dark-field imaging
HOMO	Highest occupied molecular orbital
HR	High resolution
HTL	Hole transporting layer
I	Current
I_m	Maximum point current
I_L	Light generated current
IRENA	International renewable energy agency
I_s	Dark saturation current
ITO	Indium doped tin oxide

J	Current density
J_{sc}	Short circuit current density
k	Boltzmann constant
λ	Light wavelength
LUMO	Lowest unoccupied molecular orbital
m-TiO$_2$	Mesoporous titanium dioxide
MAPI	Methyl ammonium lead iodide
MAPBr	Methyl ammonium lead bromide
MPPT	Maximum power point tracking
NREL	National Renewable Energy Laboratory
OAI	Octyl ammonium iodide-based samples
OAI+PAI	Mixed cation based samples
OIHP	Organic-inorganic hybrid perovskites
P	Electric Power
PAI	Propylammonium iodide-based samples
PCE	Power conversion efficiency
PIPE	Polyethyleneimine ethoxylated
PL	Photoluminescence
PSC	Perovskite solar cell
PTAA	poly[bis(4-phenyl)(2,4,6-trimethylphenyl)amine]
PTO	Passivated tin oxide
PV	Photovoltaic
SAEDP	Selected area electron diffraction pattern
SEM	Scanning electron microscopy
SQL	Shockley Queisser limit
STEM	Scanning transmission electron microscopy
T	Temperature
TCO	Transparent conductive oxide
TEM	Transmission electron microscopy
TDMASn	Tetrakis-dimethyl-amine-tin
TGA	Thermogravimetric analysis
TRPL	Time resolved photoluminescence
τ	Carrier recombination correlation constant
UPS	Ultraviolet photoelectron spectroscopy
UV	Ultraviolet

UV-VIS	Ultraviolet-visible spectroscopy
V	Voltage
V_b	Built-in potential
V_m	Maximum power point voltage
V_{oc}	Open circuit voltage
W_d	Depletion zone
XPS	X-ray photoelectron spectroscopy
XRD	X-ray diffraction

Chapter 1

Introduction

1.1   Background

With the growth of global populations and the rising human development index, the worldwide demand for electrical energy is forecasted to rise by roughly 64% in 2040 from today [1]. At present, highly CO_2 potent, natural resources account for most of the shares of global energy sources (31.2% for oil, 27.2% for coal and 24.7% for natural gas in 2020 [2]), posing an existential threat to economic prosperity, food and water security, and welfare of many thriving populations worldwide. For the sustainable development of the economy and environment, a more varied energy mix is needed, especially one with predominantly renewable and hydrocarbon-free sources, a measure necessary to keep economies afloat while preventing the devastating impacts of climate change. The International Renewable Energy Agency (IRENA) proposed in 2017 a complete decarbonization strategy of energy sources by 2060 to contain the effects of climate change, effectively requiring renewable deployment growth to surge seven times current rates [3].

To enable such an ambitious overhaul, alternative forms of CO_2-neutral energy should be cultivated. Among many forms of free, abundant, and green energy, solar energy shows immense potential due to its relatively high energy density per area (1000 W/m^2 on average). The cultivation of solar light is in fact not a novelty if we take inspirations from nature. In its most bare form, incoming light is composed of small energy packets (i.e., photons) which travel to Earth through blackbody radiation. As means to collect solar energy, plants convert photons (as well as H_2O and CO_2 molecules) to carbohydrates in a process called photosynthesis, a process which is profoundly responsible for our vast fossil fuel and biomass reserves [4]. In a similar fashion, photovoltaic (PV) devices (i.e., solar panels) collect light in the form of generated current which could be directly connected to electrical grids. These devices gained high traction due to their high power conversion efficiencies (PCEs) and integrability on both urban and non-productive land [5], [6]. Overall, the prospect of supplying the global energy demand through 150000 TW of incident solar power is highly viable.

At this moment, silicon-based modules are dominating the market share for PV technologies. These technologies are known to utilize thick wafers (roughly 100-500 μm) of high temperature processed mono- or multi-crystalline silicon [7]. However, in a bid to reduce production costs and expand the scope of applications, second and third generation thin film PV technologies have been rapidly developing, giving birth to new PV technologies such as cadmium telluride (CdTe), copper indium gallium selenide (CIGS), and organic photo absorbers. Among all developing solar technologies, perovskite solar cells (PSCs) have evolved most expeditiously, arriving at 25.5% PCE [8], [9] and 1-

year stability [10] within just over a decade since their inception. Many firms are looking to commercialize perovskite-based modules in the coming years including Oxford PV and Microquanta [11]. However, long term stability remains a challenge to be overcome to match silicon modules' 25-year life-expectancy. In the coming sections, the operation principles of PV technologies will be explained from first principles. Moreover, perovskite materials and their operation will be explained.

1.2   Semiconductors

Perovskite solar cells are largely composed of semiconductor units that each act either as photo absorbers, or charge carrier transporters, therefore, knowledge of semiconductor phenomena is instrumental for a comprehensive solar cell treatment. Unlike metals, semiconductors possess a bandgap (E_{bg}) between their conduction and valence bands as seen in the energy band diagram in Fig 1.1a. The bandgap effectively represents forbidden energy states that electron cannot occupy. Each band is composed of quantized energy-states that negatively charged electrons (e^-) could occupy. The conductivity in semiconductors is dependent on the ability of electrons to thermally migrate from the valence to conduction bands. At absolute zero, the valence band of semiconductors represents electronically filled states while the conduction band represents unfilled states (Fig 1.1a). The Fermi energy (E_f), situated in the middle point for charge intrinsic semiconductors, is the maximum energy an electron can achieve at absolute zero temperatures. At room or operating temperatures, electrons could disperse in the conduction band due to thermal vibrations, potential energies that promote bound electrons (in the valence band) to free state electrons (in the conduction band) by overcoming the bandgap. These electrons are considered free and could participate in current flow upon the application of an electric field. This property sets semiconductors apart from insulators which tend to have significantly larger bandgaps, and thus, a lower tendency of electrical conduction due to lower excited charge carriers.

The absence of an electron in the valence band creates a positively charged hole (h^+), a charge carrier, which also participate in semiconductor conductivity. Semiconductors could be classified based on the charge of majority carriers (carriers which carry most of the electric current). For example, n-type semiconductors possess excess electrons, therefore, electrons in the conduction band carry most of the current as shown in Fig 1.1b. The excess electrons create donor energy states (E_D) near the conduction band. In contrary, p-type semiconductors possess excess holes whereby most of the current is carried by holes in the valence band as shown in Fig 1.1c. The excess holes create accepter energy states near the valence band. The majority charge carriers could shift the position of the Fermi

energy upwards in n-type semiconductors or downwards in p-type semiconductors. The excess charge carriers could originate due to native crystal or bonding defects. For example, anatase TiO_2 bulk is considered n-type due to oxygen vacancies (O^-) that generate electron donors states [12]. In addition, the majority charge carriers could be modified by doping, a process by which impurity donor or accepter ions are deliberately added to the semiconductor bulk to create excess charge carriers.
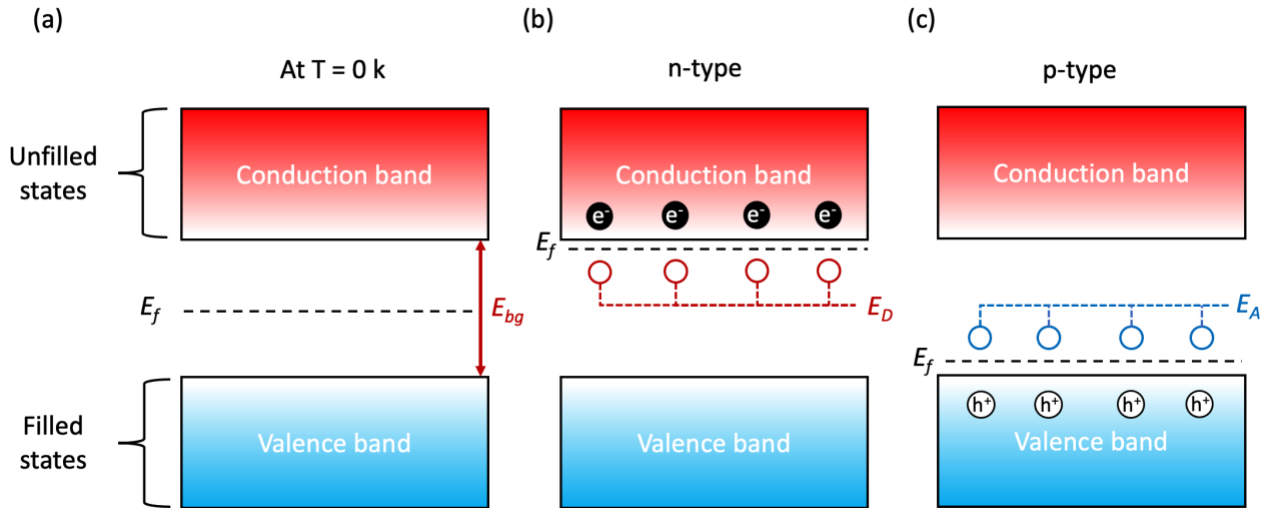
Fig 1.1 (a) Energy band diagram of a semiconductor (T = 0 k) with filled states at the valence band and unfilled states at the conduction band. (b) n-type semiconductors with electron majority carriers in the conduction band (c) p-type semiconductors with hole majority carriers in the valence band.

1.2.1 Semiconductor pn junctions

When p-type and n-type semiconductors are interfaced, a transient diffusion process occurs where excess electrons from the n-type semiconductor migrate into the acceptor states. Concurrently, excess holes from the p-type semiconductor occupy donor states. The left behind ion cores creates an electric field due to charge difference at the junction of the semiconductors that act in the opposite side of diffusion. This process creates the depletion zone (W_d) at the junction with a built-in potential (V_b) due to the electric field (caused by ionic charge difference) that generally hinders majority carrier diffusion as seen in Fig. 1.2a. When connected to a voltage source, the forward current of the pn junction can be modelled as is the case in the ideal diode (Fig. 1.2) as the following:

$$I = I_s(\exp\left(\frac{qV}{kT}\right) - 1) \hspace{3cm} \text{(eqn. 1)}$$

Where *I* and *V* is the diode current and source voltage respectively, $\frac{q}{kT}$ is the thermal voltage which is equivalent to 0.026 V in room temperature. *I*$_s$ the dark saturation current, a property proportional to semiconductor parameters such as recombination rates, thermal vibrations, pn junction area and majority carrier concentrations.
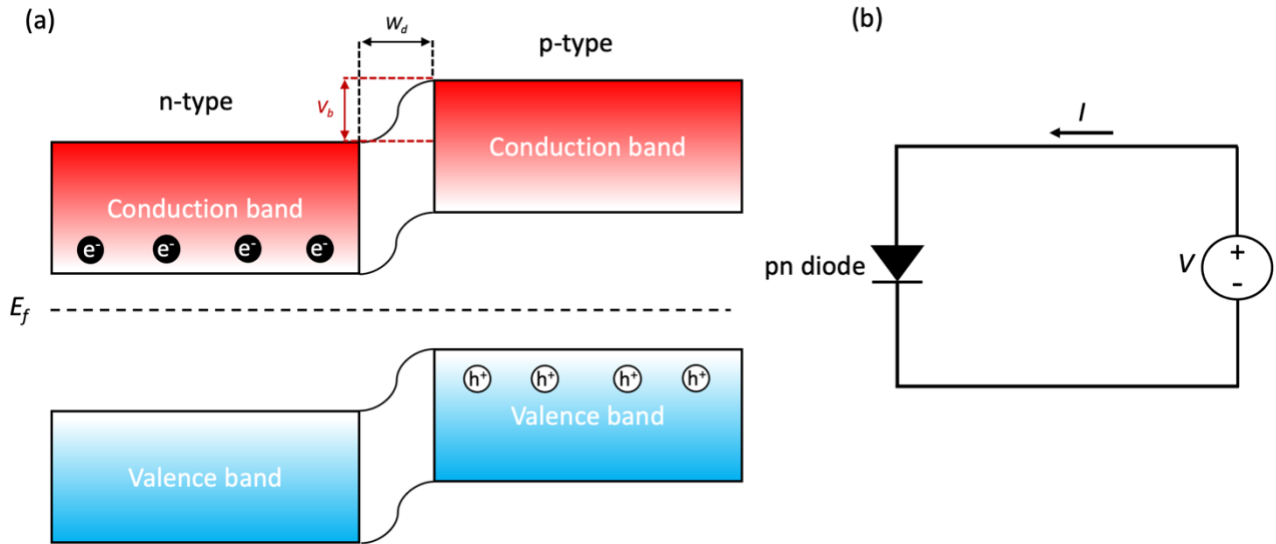
Fig 1.2 (a) Energy band diagram of a semiconductor of a pn semiconductor heterojunction. (b) equivalent circuit of an ideal pn semiconductor diode with voltage source.

1.2.2   The photovoltaic effect and *IV* Characteristic of a solar cell [15]

The prior configuration outlined in 1.2.1 showed the current behavior in the dark. However, when a semiconductor is exposed to a photon with energy (E_p) that equals or exceeds the semiconductor bandgap (eqn. 2), an electron-hole pair (exciton) is generated.

$$E_p = \frac{hc}{\lambda} \geq E_{bg}$$
(eqn. 2)

Where λ is the photon wavelength, *h* is the Plank constant and *c* is the speed of light. For instance, a photogenerated electron in the p-type semiconductor could be injected into the n-type semiconductor through the assisted junction built in potential as seen in Fig 1.3a. The photogenerated current (exciton pair) can be collected by the application of an external bias to the pn-diode. In this scheme, if the pn diode under light is connected to a voltage source, the ideal equivalent circuit (Fig 1.3b) will have the following current:

$$I(V) = I_L - I_d = I_L - I_s \left(\exp\left(\frac{qV}{kT}\right) - 1 \right) \qquad \text{(eqn. 3)}$$

Where I_d and I_L is the diode and photogenerated current respectively. Moreover, the power generated through the solar cell can be calculated from the total current and voltage as the following:

$$P(V) = IV \qquad \text{(eqn. 4)}$$

By plotting the current and power equations with respect to the current, the IV characteristic of an ideal solar cell can be extracted as seen in Fig. 1.4.
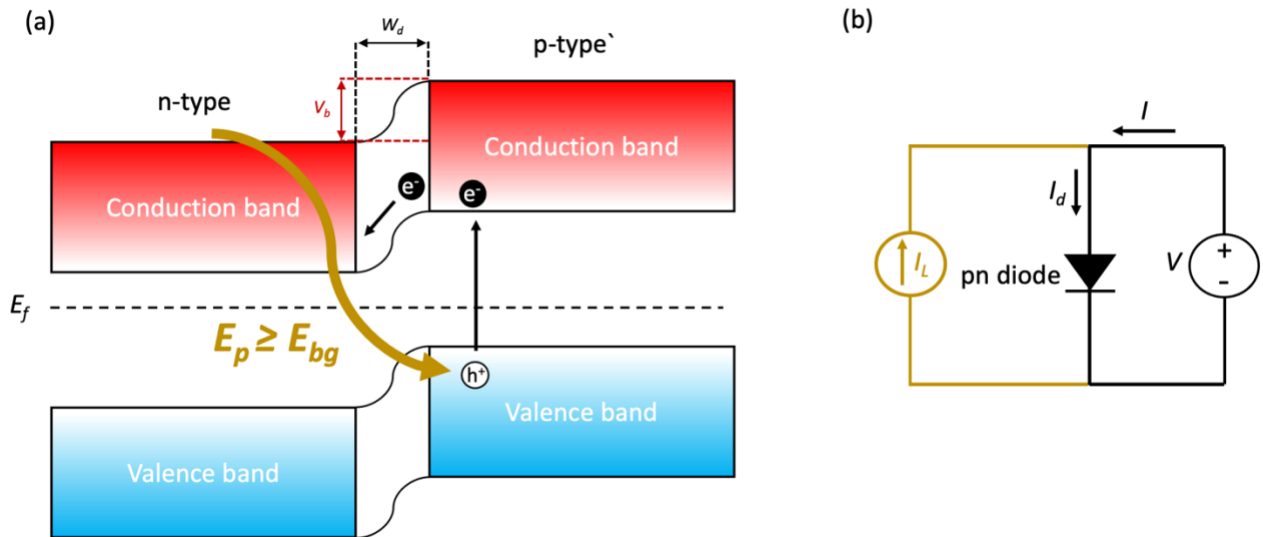
Fig 1.3 (a) Energy band diagram of pn heterojunction electron injection from p- to n-type semiconductor under the light. (b) equivalent circuit of an ideal pn semiconductor diode with voltage source under illumination.
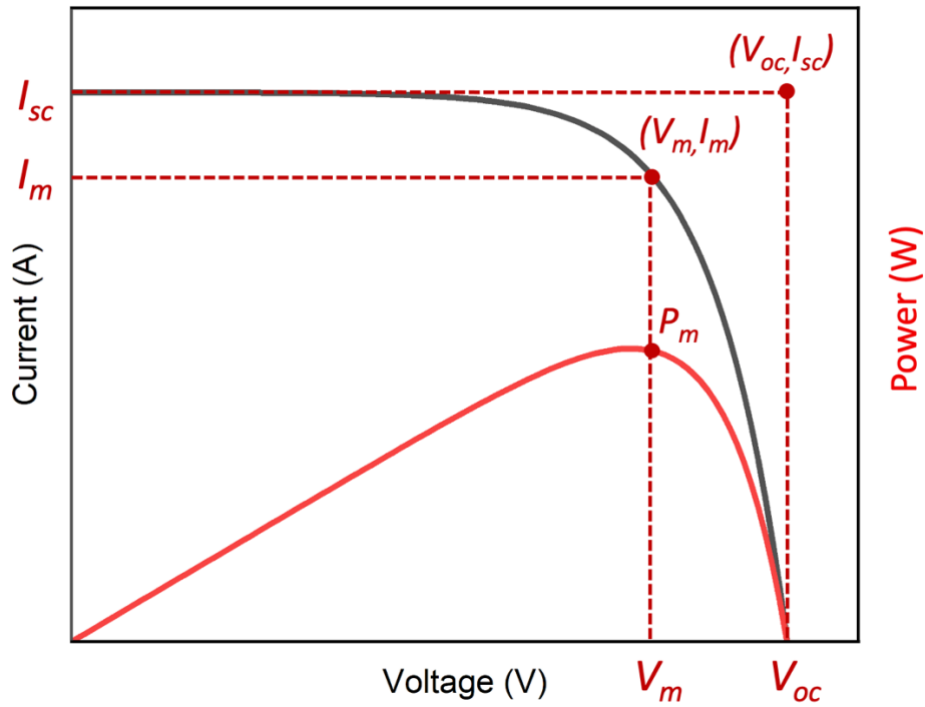
Fig 1.4 IV Characteristic and power with respect to voltage of an ideal pn junction diode with photogenerated current.

As can be seen from the IV characteristics, the power generated from a solar cell increases with voltage until a maximum is reached, a parameter identified as the maximum power point (P_m) and is achieved at maximum voltage and current (V_m and I_m respectively). This parameter is also known as the power conversion efficiency (*PCE*) of a solar cell. The open circuit voltage (V_{oc}) is another important parameter which describes the voltage required to produce zero net current. Moreover, the short circuit current (I_{sc}) is the current generated without voltage application and is commonly denoted per unit area as short circuit current density (J_{sc}). The fill factor (*FF*) of a solar cell is the rectangular ratio of the above-described parameters as could seen in eqn. 5:

$$FF = \frac{I_m V_m}{I_{SC} V_{oc}}$$ (eqn. 5)

A higher *FF* usually implies a higher performing solar cell device which is highly linked to the V_{oc}. Moreover, the power conversion efficiency could be obtained in terms of the fill factor by using the following correlation:

$$PCE = FF\,(I_{SC} V_{oc})$$ (eqn. 6)

1.3   Perovskite solar cells

Perovskite solar cells (PSCs) have endeavored the most rapid development among other photovoltaic based technologies in the basis of efficiency improvement with respect to time. Perovskite photovoltaics were first reported in literature when they emerged as a spin-off from dye-synthesized solar cells (DSSCs) in 2009 where perovskite nanoparticle sensitizers were applied on TiO_2 nanoparticles in a liquid electrolyte achieving an efficiency of 3.9% [16]. Since then, much development has been done with perovskite materials employed as standalone solid-state photo absorbers [17] among many profound architectural changes [18]. Today, the record efficiency is sitting at 25.5% [8], [9], exceeding mature technologies such as copper indium gallium selenide (CIGS) [19] and cadmium telluride (CdTe), and competing with crystalline silicon based cells [8]. In the following subsections, we go through the photo absorbing perovskite material (1.3.1), the operation principles of a full PSC (1.3.2) and outline the role of each layer in a complete stack architecture (1.3.3). Moreover, we outline challenges associated with recombination processes as well as types of imperfections that impact the PCE and stability of PSCs (1.3.4). Finally, we highlight passivation strategies that minimize defect-induced recombination in the state of the art of the domain of perovskite solar cells (1.4) including approaches that involve electron transporting layers (1.4.1) and 2D perovskites materials (1.4.2).

1.3.1   Perovskite photoabsorbing materials

Perovskites are a class of materials known for exhibiting unique crystal characteristics based on dimensionality governed by the Goldschemist's tolerance factor. The first example was identified by Gustav Rose in 1893 as a mineral (e.g., calcium titanate or $CaTiO_3$) in the Urai Mountains of Russia. However, in 1994, the semiconductivity of hybrid organic-inorganic halide perovskites (OIHP) was first highlighted, with the flexibility to tune electrical properties by organic layer modulation [20]. About a decade thereafter, the breakthrough with DSSCs was done where perovskites such as methylammonium lead iodide (MAPI) and methylammonium lead bromide (MAPBr) were used for the first time as dyes in solar cells [16]. OIHPs have been on the spotlight for photovoltaic development since then. The ideal cubic unit crystal cell (Fig. 1.5a) of a perovskite is composed of three main groups; a monovalent cation (A) such as methylammonium (MA^+) or formamidinium (FA^+); a bivalent metallic cation (B) such as lead (Pb^{2+}) or tin (Sn^{2+}), and a halide anion (X) such as

iodine (I^-) or chloride (Cl^-) or bromide (Br^-). Together these groups form the ABX_3 crystal structure, also known as a three-dimensional (3D) perovskite. To maintain the 3D framework, the A-site cation radius must be lower than 2.6 Å based on the Goldschmidt's tolerance factor [21]. Furthermore, 3D perovskite materials are known for their cheap and facile fabrication at low temperature (~100 °C) [22]–[25], high defect tolerance [26], [27], and superior diffusion length (over 1 μm) [28], [29]. Moreover, the tunability in perovskite components has opened the door to much compositional research, especially in the monovalent cation components, with multi-cation combinations with MA, FA, Cs and Rb paving the way for highly efficient and stable solar cells [30]–[34], in addition to work on halide component mixing (I, Br and Cl) [35]–[38]. The modification of these components affect lattice distortions caused by the AX_6 octahedra (Fig. 1.5b), an important parameter which is linked to the bandgap and other optoelectronic properties of the perovskite layer [39], [40].
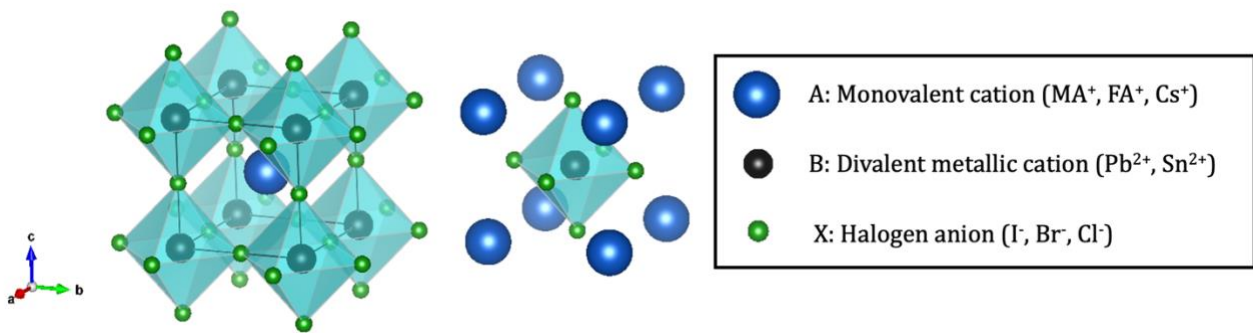
Fig 1.5 Hybrid organic-inorganic halide perovskites (OIHP) following the ABX_3 crystal structure with ideal cubic configuration. (a) Unit cell centered at the metallic cation and (b) centered around the BX_6 octahedra. The unit cell models in this figure were constructed through VESTA software package [41].

1.3.2   Operation of perovskite solar cells

To facilitate optimal charge generation and extraction, the perovskite layer is sandwiched between two charge transporting layers, the electron transport layer (ETL) and hole transporting layer (HTL), n-type and p-type semiconductors respectively. These charge transporting layers are each connected to a back and front contact respectively. The basic operation of perovskite solar cells starts with the photogeneration of exciton pairs upon the illumination with high energy photons. The photogenerated electron is extracted to the ETL while the photogenerated hole is extracted to the HTL. Ultimately, the photogenerated pairs are finally collected at the back and front contacts of the cell. Fig. 1.6 illustrates the three stages in terms of the energy band diagram.
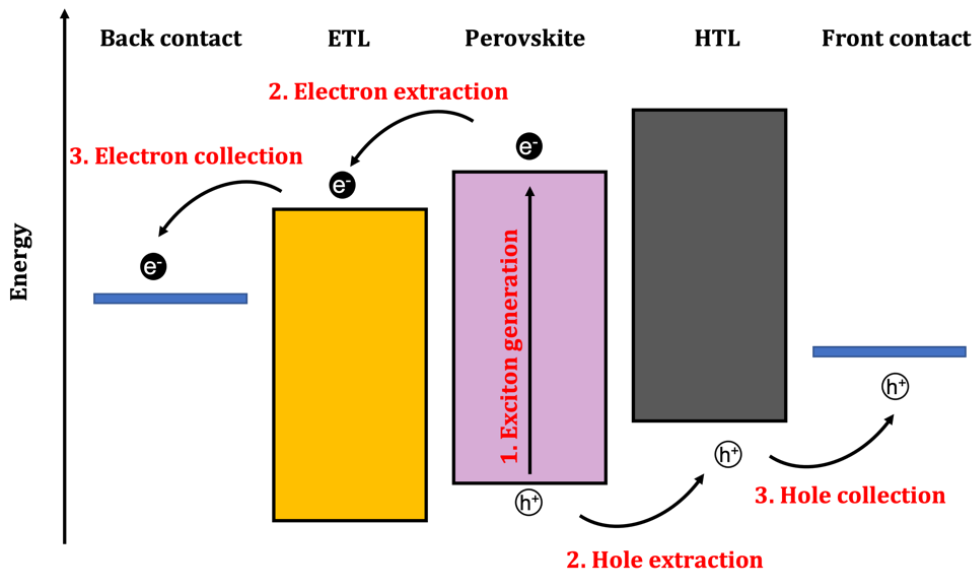
Fig 1.6 Operation of a PSC showing the three stages of photovoltaic processes; 1. Exciton generation at the perovskite layer as a response of high energy photon, 2. Charge carrier extraction through the charge transport layers and 3. Charge carrier collection in the front and back contacts.

1.3.3 Architecture of perovskite solar cells

The architecture of PSCs is classified based on the arrangement of the charge transporting layers and the nanostructures present within the device stack. Intrinsic (i) perovskite layers could be placed in two arrangements; conventional (n-i-p) or inverted (p-i-n) arrangements as demonstrated in Figures 1.7a and 1.7b respectively. For the n-i-p configuration the incident light passes through the ETL and for the p-i-n, the incident light passes through the HTL. The n-i-p configuration usually utilizes metal oxides such as TiO_2, SnO_2, and ZnO as ETLs (more on ETLs in section 1.3.1 in Chapter 1), and organic materials such as doped Spiro-OMeTAD and poly[bis(4-phenyl)(2,4,6-trimethylphenyl)amine] (PTAA) as HTLs. For the charge collecting contacts, the front contact is composed of a transparent conductive oxide (TCO) such as fluorine-doped or indium-doped tin oxide (FTO and ITO respectively), whereas the back contact is composed of a metal such as Au, Ag and Cu. The earlier perovskite device concepts employed a mesoporous scaffold (Fig. 1.7c) at the ETL due to the evolution from DSSC. The mesoporous configuration utilizes a metal oxide scaffold such as TiO_2 or SnO_2 for high area, electron extraction from the perovskite layer. Despite their higher PCE tendency, their fabrication requires high processing temperatures (>400 °C) which places a limit on

their scope of application. The n-i-p configuration was employed in the experimental work in this thesis.
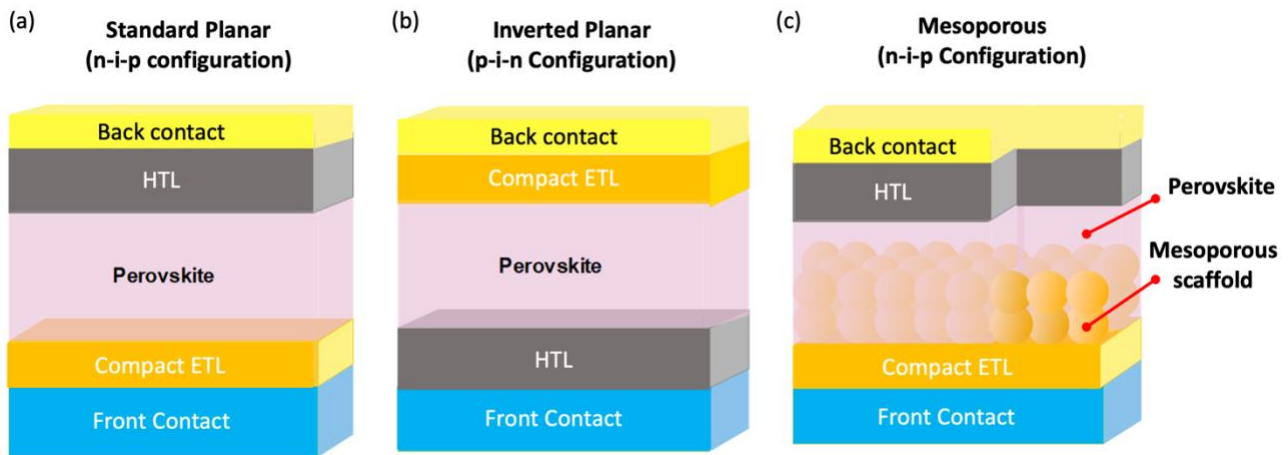
Fig 1.7 Perovskite solar cell (PSC) device architectures (a) n-i-p planar configuration, (b) p-i-n planar configuration (c) n-i-p mesoporous configuration

1.3.4 Recombination in perovskite solar cells

According to the Shockley-Queisser limit (SQL), the maximum performance power conversion efficiency for 1.5 eV bandgap perovskites is approximately ~32% [42], an approximation which far exceeds today's record of 25.5% [8]. Charge carrier recombination is the main reason behind the overestimation as the SQL does not put into account non-radiative recombination processes such as Auger and defect-assisted recombination. Recombination losses not only reduce the photovoltaic performance of PSCs but also could act as centers for degradation processes, impacting the long-term stability of the PSC device. Minimizing recombination is an important strategy to advance the global prospect for PSCs to enter the photovoltaic marketplace. Recombination could be categorized into radiative and non-radiative recombination. Radiative recombination is the band-to-band transition of photogenerated carriers which constitutes an insignificant proportion in recombination losses in the context of solar cells [43]. Auger (or many body) recombination is the energy loss due to direct recombination of an electron-hole pair followed by an energy and momentum transfer to a third-body (electron, hole or phonon) [44]. Defect assisted recombination is loss associated with monomolecular trapping of an electron or hole in a defect or impurity state. The equation below summarizes recombination induced losses [45]:

$$\frac{dn}{dt} = -\tau_1 n - \tau_2 n^2 - \tau_3 n^3 \qquad \text{(eqn. 7)}$$

Where $\frac{dn}{dt}$ describes the change in charge carrier density with respect to time, and τ_1, τ_2, and τ_3 are rate constant factors for defect-assisted, radiative and Auger recombination processes respectevely. These parameters could be estimated through time resolved photolumnesce (TRPL) spectroscopy [46]. Key parameters such as diffusion length and carrier lifetime are strongly affected by the recombination rate, therefore, minimizing recombination is an important approach in improving the power conversion efficiency of solar cells.

A considerable proportion of perovskite photovoltaics research aims to reduce trap-density as a measure to minimize defect-assisted recombination. Approaches that extend the carrier lifetime by reducing trap-density are usually referred to as defect passivation [47]. Within perovskite films, defect centers had been identified along the perovskite grain boundaries and film surface [48], [49]. The localization of traps around grain boundaries were verified by local PL lifetime investigations by De Quilettes *et al* where carrier lifetime was demonstrated to be shorter at grain boundaries than grain bulk [50], conforming to other studies [51]–[53]. Examples of possible defects within the perovskite lattice include uncoordinated ions, vacancies and Pb clusters which induce trap states at the perovskite grain boundaries and surfaces as shown in Fig 1.8 [33]. Recent advancements in perovskite fabrication processes produce monolithic, homogenous and controlled perovskite grains which minimize traps-states across the bulk [54]–[56]. Nevertheless, surface defects, a direct consequence of the discontinuity of perovskite lattice and surface remain a relevant challenge to be tackled.
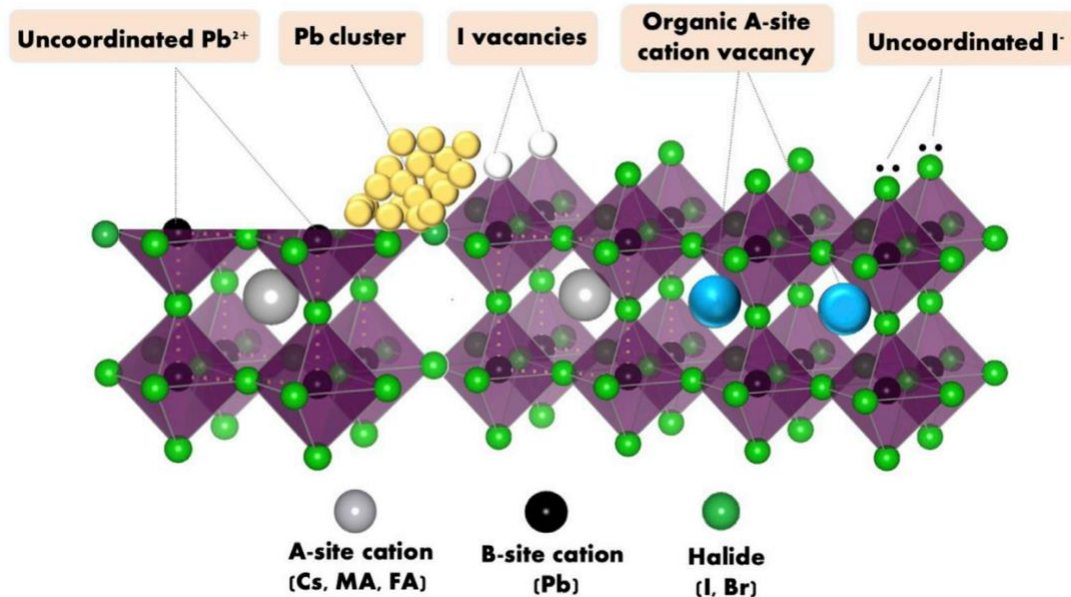
Fig 1.8 Possible defects across grain boundaries and surfaces which could be present in a OIHP lattice taken from reference 33.

1.4   Passivation approaches in perovskite solar cells

Surface passivation approaches had begun with the discovery of the positive impact excess PbI_2 has on reducing *J-V* hysteresis, improving device performance and stability in the work of Chen *et al* on perovskite films [57]. The study linked the annealing time of $CH_3NH_3PbI_3$ with PbI_2 content and conclusively found that samples annealed for 60 min produced the highest carrier lifetime and device efficiency as demonstrated in Fig. 1.9. This enhancement in PV parameters was associated with an extension in carrier lifetime in samples that possess excess PbI_2 concentrations due to defect passivation. This discovery led to further optimizations of perovskite compositions with excess PbI_2 [58]–[61]. Ultimately, Roldan *et al* showed that non-stoichiometric (>20% molar excess) ratio between PbI_2 and MAI in the perovskite precursor solution is beneficial for the electron transfer to TiO_2 [62], proving surface passivation at the ETL/perovskite interface. The excess PbI_2 approach had effectively inspired interfacial passivation approaches which involve the addition or modification of passivation layers at perovskite interfaces with electron and hole transporting layers. The perovskite scientific community explored a multitude of interfacial passivation approaches, including the addition of Lewis-bases [63]–[65], ionic liquids [66]–[68] and many other capping layers [69]–[71] at perovskite interfaces. For the purpose of this thesis, the scope of interfacial passivation approaches will be centered on electron transporting and 2D perovskite layers and will be covered in the forthcoming sections.
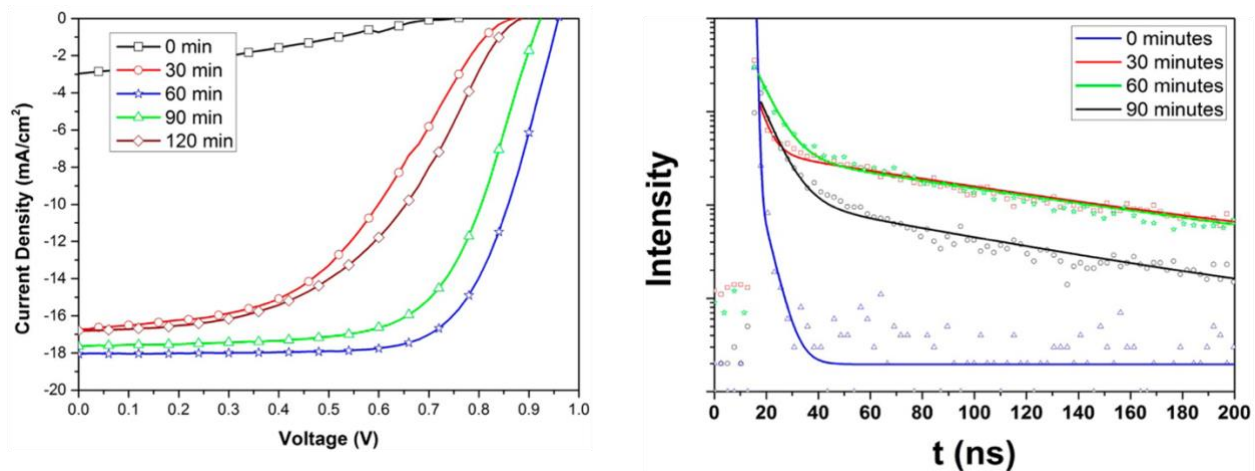
Fig 1.9 *J-V* characteristic (on the left) and carrier lifetime (on the right) of samples with different $CH_3NH_3PbI_3$ annealing times. Samples annealed for 60 min produced the highest device conversion efficiency and carrier lifetime due to excess PbI_2 content taken from reference 57.

1.4.1 Electron transporting layers

Principally, ETLs are semiconductors that extract photoelectrons from the perovskite film and inject them into the contact for current collection. For optimal electron extraction, a couple of ETL parameters must be considered, including favorable energy band alignment, high electron mobility, hole blocking capability and relatively high bandgap. Moreover, the perovskite film formability and quality are linked with the wettability of the underlying ETL [72] in n-i-p configurations, signifying the importance of interface in both charge extraction and perovskite crystal growth. Therefore, a careful selection of ETLs is necessary for enhancing the performance of PSCs. Metal oxides such as TiO_2, SnO_2 and ZnO have been widely used as ETLs in n-i-p configurations due to their suitable optoelectronic properties. Table 1.1 summarizes the electron mobility and bandgap of these metal oxides.

Table 1.1 electron mobility and bandgap values of metal oxides (TiO_2, SnO_2, and ZnO) commonly used as ETL.

ETL Material	Electron mobility $(cm^2V^{-1}s^{-1})$	Bandgap (eV)
TiO_2	1 [73]	3.03-3.20 [74]
SnO_2	250 [73]	3.6-4.1 [75]
ZnO	200 [73]	3.2 [75]

Early works on PSCs utilized dual (compact and mesoporous) TiO_2 as an ETL [76]. The mesoporous TiO_2 scaffold promotes higher charge injection at the ETL/perovskite interface when compared to ETLs with a single c-TiO_2 film [77]. However, this configuration poses a couple of challenges including the need of high processing temperatures (over 400 °C) and increasing the device fabrication complexity. In addition, TiO_2 has a low electron mobility compared to other metal oxides (Table 1.1) and was reported to promote perovskite degradation due to photocatalytic tendency [78], [79] and charge recombination [80]–[82] at the TiO_2/perovskite interface. These challenges had inspired the use of capping layers at the interface to passivate defects and eliminate the use of the mesoporous scaffold. TiO_2 and ZnO bilayers has shown potential particularly because of ZnO's high electron mobility and tendency to enhance the PCE [83]. However, the use of ZnO predisposes the

perovskite film to thermal instability due to the presence of surface hydroxyl groups and/or residual acetate ligands in ZnO [84].

Fortunately, the use of SnO_2 as an ETL has garnered success particularly in planar n-i-p configurations. SnO_2 films could be fabricated in facile and low temperature (<200 °C) solution processible methods including spin-coating [85], spray pyrolysis [86] and chemical bath deposition [87]. Moreover, not only does SnO_2 have favorable optoelectronic properties such as deep bandgap and high electron mobility (Table 1.1), SnO_2 also has high chemical stability and minimal photocatalytic activity [88], properties which are important to promote long term stability. In 2015, SnO_2 was first utilized in the work of Li *et al* where it was implemented as a mesoporous layer in PSCs to replace TiO_2 achieving 10.8% efficient devices [89]. Subsequently in the year after, the perovskite scientific community picked up work on low-temperature, compact SnO_2 bringing the performance of planar PSC configurations for the first time above 20% [81], [90]. The progress with SnO_2 has opened doors for planar n-i-p PSCs to compete with the more efficient mesoporous n-i-p counterparts. Work undertaken in this thesis aims to expand knowledge in passivation approaches targeting ETL layers. In Chapter 2, light soaking investigations were done to compare stability properties of perovskite samples utilizing TiO_2/SnO_2, SnO_2, and TiO_2 ETLs. The study aims to bring about consensus to the advantages of utilizing bilayered (TiO_2/SnO_2) configurations. In Chapter 3, the self-passivating properties of low temperature processed SnO_2 was studied to explain the benefit of present amorphous phase halides.

1.4.2   2D Perovskite Interfacial layers

Lower dimensional perovskite materials have drawn enormous attention due to new properties that they could bring into the fold. Particularly, Ruddlesden-Popper 2D perovskite structures were recently highlighted due to their high durability to heat, moisture, and other environmental parameters [91]–[93]. These 2D structures employ a $R_2A_{n-1}B_nX_{3n+1}$ crystal framework where R is a bulky organic cation (such as aliphatic or aromatic alkylammoniums) that acts as an organic spacer and n is the number of repeating inorganic units sandwiched between the organic spacers [94]–[96]. When n = 1, the structure is categorized as pure 2D perovskite, whereas when n ≥ 2, the structure is designated as quasi-2D. Fig 1.10 provides an illustration of 2D perovskite structures. Usually the length of the bulky cation (R) determines the hydrophobicity of the 2D perovskite [89], [98] [95], a critical property which determines the environmental stability of the 2D perovskite. Despite the impressive stability, 2D perovskite materials are known for their low efficiency due to the insulating nature of the organic

spacers (R) inducing a wide bandgap, high exciton binding and limiting charge transport especially at lower n values [92]. The highest performing PSC based on 2D perovskite photo absorbers has an efficiency of 19.3% (based on $GA_2MA_4Pb_5I_{16}$) [99] which is far away from the efficiency of 3D perovskite-based counterparts.
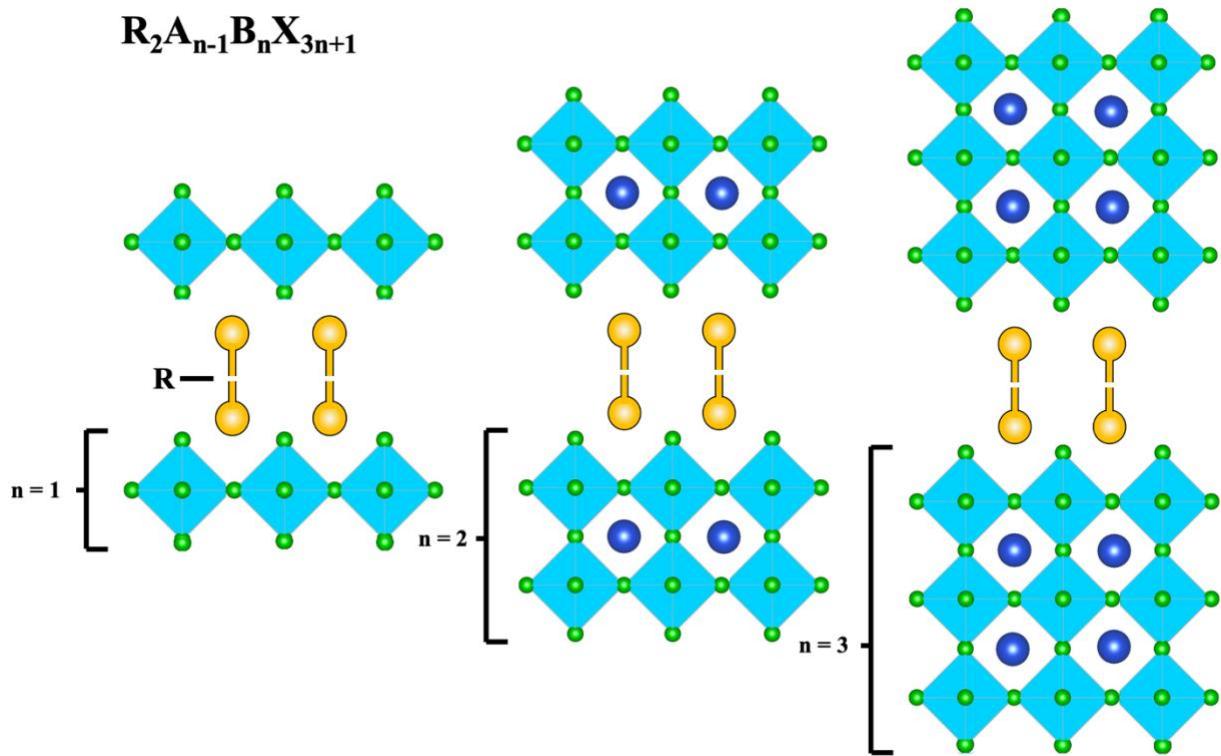
Fig 1.10 Illustration of 2D perovskite structures following $R_2A_{n-1}B_nX_{3n+1}$ frameworks where n = 1 signifies pure 2D structures and $n \geq 2$ signifies quasi 2D structures.

One strategy to bridge the stability of 2D perovskites with the performance of the 3D counterparts is by utilizing 3D/2D structures within the PSC device stack. An early example of this approach was done in the work of Cho *et al* where phenethyl ammonium iodide (PEAI) solution was deposited dynamically into a 3D perovskite film ($Cs_{0.1}FA_{0.74}MA_{0.13}PbI_{2.48}Br_{0.39}$) [100]. In this case, it was reported that the PEAI reacts with excess PbI_2 in the 3D perovskite surface to form a 2D perovskite (PEA_2PbI_4) layer. This work, undertaken in 2018, produced over 20% efficient PSCs with 85% efficiency retention under one sun illumination and ambient conditions for 800 h at 50 °C, demonstrating the potential for performance and stability improvement with 3D/2D structures. Moreover, samples with 3D/2D structures showed a higher photoluminescence lifetime and lower trap-state density than single 3D samples, indicating an interfacial passivation effect. Other studies showed similar phenomena with other organic salts such as 5-ammonium valeric acid iodide (AVAI)

[101], [102], 5-butylammonium iodide (BAI) [103]–[105] and other 2D perovskite precursors [106]–[109]. To capture the benefits of this approach, more fundamental work should be done to understand passivation mechanisms. Chapter 4 explores a novel 2D perovskite approach that involves mixing two alkylammonium halides precursors to form new 2D perovskite structures.

1.5   Summary

In this chapter, an overview was presented from the basics of solar energy to the state-of-the-art in the domain of perovskite photovoltaics. Solar cell devices are composed of semiconductors that participate in the generation, transportation, and collection of photocurrent. Many notable 3rd generation photovoltaic technologies have emerged over the last decades. However, the strides made in the short span of perovskite solar cell development have been rapid and promising. Despite their high-power conversion efficiency, perovskite solar cells suffer from low device stability, notably due to trap-assisted recombination processes that occur at perovskite grain boundaries and surfaces. Passivation approaches are strategies developed to minimize trap-states density to tackle recombination and enhance the parameters of perovskite solar cells. The perovskite scientific community have implemented many passivation strategies, particularly modifying interfaces of perovskite surfaces with transporting layers. This thesis explores interface and composition approaches with the aim to reduce trap-assisted recombination to promote the performance and stability of perovskite solar cells.

Chapter 2

Examining the performance and stability improvement by utilizing bilayered TiO$_2$/SnO$_2$ electron transporters

In this work, we aim to gain insight of electron transporting layer (ETL)/perovskite interfacial degradation by characterizing perovskite films with TiO$_2$, SnO$_2$, and TiO$_2$/SnO$_2$ ETLs. Our results demonstrate SnO$_2$ and TiO$_2$/SnO$_2$ maintained long-term stability of 1000 h under maximum power point tracking while the TiO$_2$ sample degraded upon onset. We attempt to link this analogy to the perovskite film properties by monitoring the optoelectronic and morphological features under light-soaking for each electron transporting layer configuration. Our results demonstrate reduced photoluminescent emission and decay, perovskite film morphological degradation, and a surge in PbI$_2$ in TiO$_2$ samples, trends which were not found in SnO$_2$ and TiO$_2$/SnO$_2$ samples. We highlight the passivation effect of SnO$_2$ films in bilayered ETL configuration (TiO$_2$/SnO$_2$) that result in stability enhancement phenomena as speculated from our constructed energy diagram. The results show that the SnO$_2$ layer could suppress charge recombination with the perovskite layer and improves the optical durability of the PSC device.

2.1   Introduction

Operational stability of PSCs remains to this day remains a challenge mostly attributed to the interfacial decomposition of sensitive components in the PSC stack including the perovskite film under light irradiation, among other factors.[110], [111] Compact TiO_2 (c-TiO_2) has been favored as an electron transporting layer (ETL) due to its intrinsic electron extraction properties and suitable wide bandgap of ~3.2 eV. Nevertheless, various reports have pointed out that perovskite films degrade due to photo-electron accumulation and trapping at the c-TiO_2/perovskite interface.[112]–[114] The addition of capping layers has been an effective approach to reduce degradation. Leijtens *et al.* had reported a sharp degradation in PSCs with TiO_2 in direct contact with $MAPbI_3$ and that c-TiO_2/mesoporous Al_2O_3 layers accomplished a steady photocurrent over 1000 h under full light spectrum.[82] In addition, Ji *et al.* recently reported a similar stabilization of the PSC device by adding a polyethyleneimine ethoxylated (PEIE) layer at the c-TiO_2/perovskite interface retaining ~75% of initial performance for 72 days.[115] Other candidates such as ZnO [83], WO_3 [116], and Sb_2S_3[112] have been used as capping layers between c-TiO_2 and perovskite. These studies highlight the potential of interfacial capping as an approach for stabilizing PSC devices.

Stacking two different ETLs, essentially creating a bilayered electron extraction film, is another promising approach to enhance stability without compromising device performance. SnO_2 is an excellent candidate since it has an ideally broad bandgap and excellent carrier extraction capability.[90] Therefore, bilayered TiO_2/SnO_2 ETLs have been widely explored and have yielded high performing PSC with PCEs well over 20% [117]–[121] owning to enhance hole-blocking ability. However, more light stability investigations should be done to compare the impact of sole TiO_2 and SnO_2 films as well as bilayered TiO_2/SnO_2 on the perovskite film in an operating device. In this work, stability of perovskite samples with different ETL configuration was explored through a light-soaking setup to observe morphological and photoluminescence properties before and after light exposure. Device fabrication and sample preparation procedure could be found in section 6.1.1 in Chapter 6. Moreover, characterization and supplementary information could be found in section 6.1.2 and 6.1.3 respectively in Chapter 6.

2.2   Results and discussion

Planar PSCs were fabricated with the following architecture fluorine-doped tin oxide (FTO)/ETL/perovskite/spiro-OMeTAD/Au where the ETL film was varied as shown in the schematic in Fig. 2.1a. Triple cation perovskite based on $(FAPbI_3)_{0.875}(MAPbBr_3)_{0.125}(CsPbI_3)_{0.1}$ was utilized as a photoactive layer. Three different ETL configurations were fabricated with the same PSC architecture with TiO_2, SnO_2, and TiO_2/SnO_2. Scanning electron microscopy (SEM) images were taken for perovskite surface and device cross-section for all ETLs (Fig. S2.1 and S2.2 respectively in section 6.1.3). Fig. S2.1 shows no change in perovskite grain-size and Fig. S2.2 shows no change in the perovskite thickness across the device cross-section when ETL configurations are varied. These SEM images indicate identical grain growth during device fabrication irrespective of ETL. PSC devices were placed inside an encapsulated stability apparatus in ambient nitrogen with an approximate relative humidity of 0% and exposed to light intensity equivalent to AM 1.5 G illumination. The bias was maintained at MPPT and cells were kept at room temperature during the stability testing. Fig. 2.1b demonstrates the normalized PCE against time for the three PSC samples with the different ETLs. SnO_2 and TiO_2/SnO_2 samples show excellent PCE retention of 95% and 97% respectively after 1000 h while the PCE of the TiO_2 sample abruptly deteriorated upon the start to 25% after 1000 h. The sharp decrease in TiO_2 samples is identical to stability behavior previously reported as a result of direct contact of TiO_2 with the perovskite layer [115], [122], causing perovskite degradation. The stability enhancement in SnO_2 and TiO_2/SnO_2 samples prove the detrimental role ETL layers have on stability. To investigate the effect of the UV light on the stability, we measured MPPT with UV light (Supporting information, Fig. S2.3). The PCE of the TiO_2 sample dropped significantly to 49% from the initial efficiency at 50 h, a faster rate than the TiO_2 samples without UV light (82% at 50 h, Fig 2.1b). The sharper drop in PCE with UV light is a consequence of the photocatalytic tendency of TiO_2.[115], [123] Whereas, for the case without UV light, Ahn *et al* demonstrated that interfacial TiO_2/perovskite degradation occurs due to the accumulation of trapped carriers at the interface.[113] We further run a series of characterizations to understand features of stable and degraded perovskite samples.
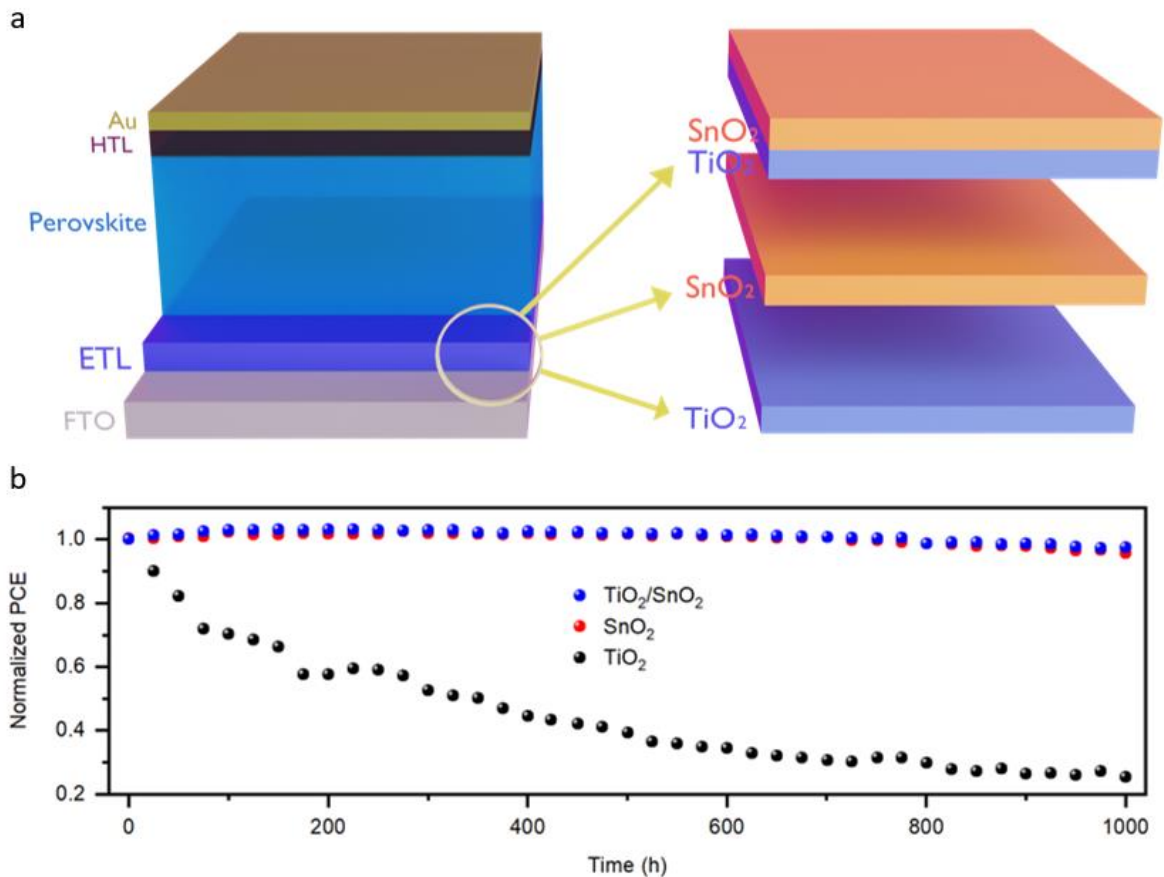
Fig 2.1 (a) Schematic of the planar-type perovskite solar cell architecture highlighting three different ETL configurations used. (b) Normalized stability of encapsulated PSCs operating at MPPT for 1000 h for TiO_2/SnO_2, SnO_2, and TiO_2 ETLs under AM 1.5G.

To understand better degradation processes with respect to carrier dynamics occurring with each ETL configuration, photoluminescence (PL) emission and decay characterization were performed to analyze charge generation and transport processes. Fig. 2.2a, b, and c demonstrate the PL emission spectra for TiO_2, SnO_2, TiO_2/SnO_2 PSC samples respectively before and after 50 h of MPPT operation. The PL emission analysis highlights sharp decrease of TiO_2 sample PL peak (Fig 2.2a) whereas SnO_2 and TiO_2/SnO_2 samples (Fig 2.2b and c, respectively) demonstrated no prominent changes in the peak before and after light soaking. The lower PL emission peak suggests faster and possibly more charge-carrier recombination,[115] resulting in reduction in the normalized PCE for TiO_2 with photovoltaic (PV) operation as observed in Fig 2.1b. Further, Fig. 2.2d, e, and f demonstrate PL decay curves for each TiO_2, SnO_2, and TiO_2/SnO_2 PSC samples, respectively. Most notably, the decay time has significantly decreased for the TiO_2 sample while for the other two samples, the decay time has no significant changes. The decay curves imply that the lifetime of charge-carriers in the TiO_2 sample is dramatically reduced from 90.9 to 34.0 µs (Table S2.1) by opening recombination

pathways after PV operation as compared with other ETL samples, which could be due to the photodegradation with TiO_2. To elucidate the charge-carrier recombination caused by the photodegradation of TiO_2, the diode factor was measured that is related to Shockley-Read Hall recombination using the SunsVoc method.[124], [125] Samples were measured after the light soaking for 100 h (Supporting information, Fig. S2.4). The diode ideality factor of TiO_2 was 4.25, whereas SnO_2 and TiO_2/SnO_2 were 2.02 and 1.48, respectively. This result implies that the TiO_2 sample has more charge carrier recombination, which is consistent with the trends observed with PL emission and decay (Fig. 2.2). These results demonstrate that the SnO_2 film was successful in suppressing perovskite degradation in the bilayered TiO_2/SnO_2 configuration by maintaining the carrier dynamics of the perovskite layer.
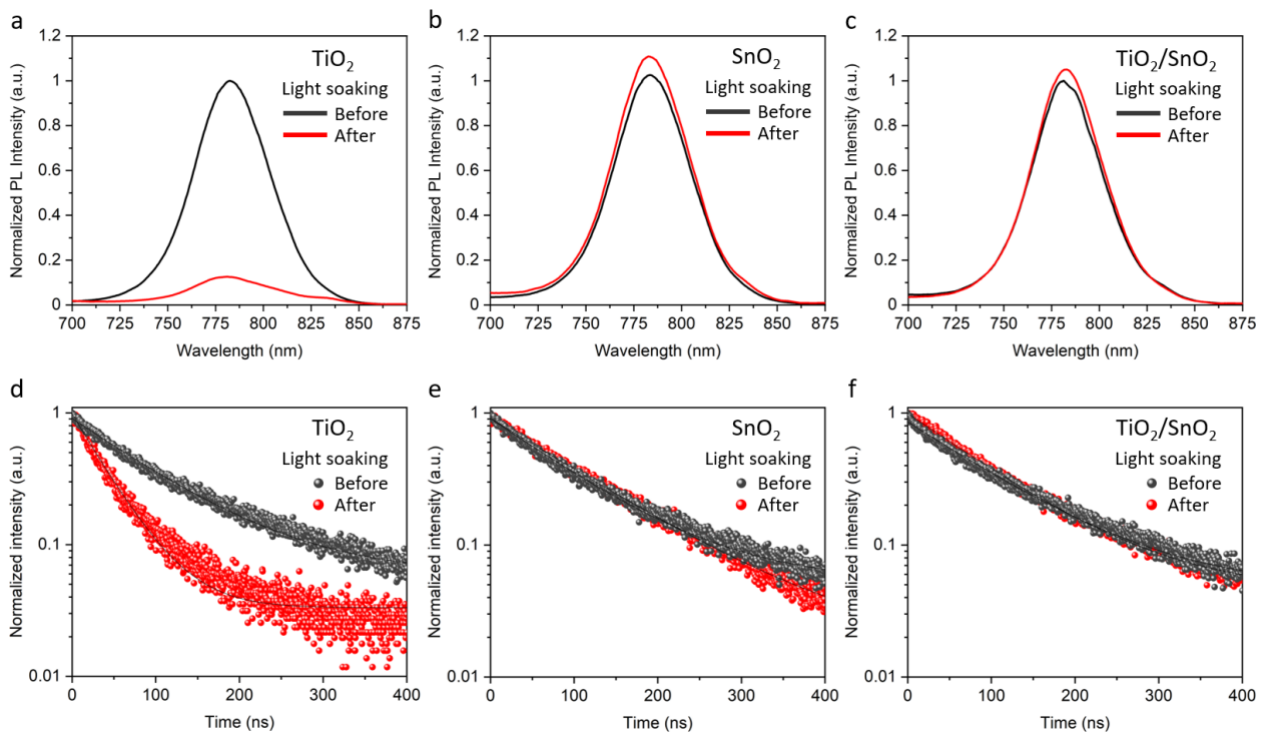
Fig 2.2 Photoluminescence analysis on fresh and 50 h MPPT. Normalized emission photoluminescence peak curves against wavelength operated with (a) TiO2, (b) SnO2, and (c) TiO2/SnO2 samples. Normalized decay photoluminescence curves with (d) TiO2, (e) SnO2, and (f) TiO2/SnO2 with intensity in logscale versus time.

Cross-sectional scanning electron microscopy (SEM) images were captured for perovskite samples with TiO_2, SnO_2, and TiO_2/SnO_2 ETLs respectively before and after subjecting the samples to AM

1.5G simulated light for 500 h as seen in Fig. 2.3. The images demonstrate a significant deterioration of perovskite film with TiO_2 after light exposure as seen in Fig. 2.3a and d while perovskite films for other ETLs have relatively maintained morphological integrity as seen with SnO_2 (Fig. 2.3b,e) and TiO_2/SnO_2 (Fig. 2.3c,f). This result, coupled with the PL measurements indicates that due to morphological deterioration, photoactive regions in the bulk of the perovskite have been diminished, explaining the quenching in PL emission peak and decay.
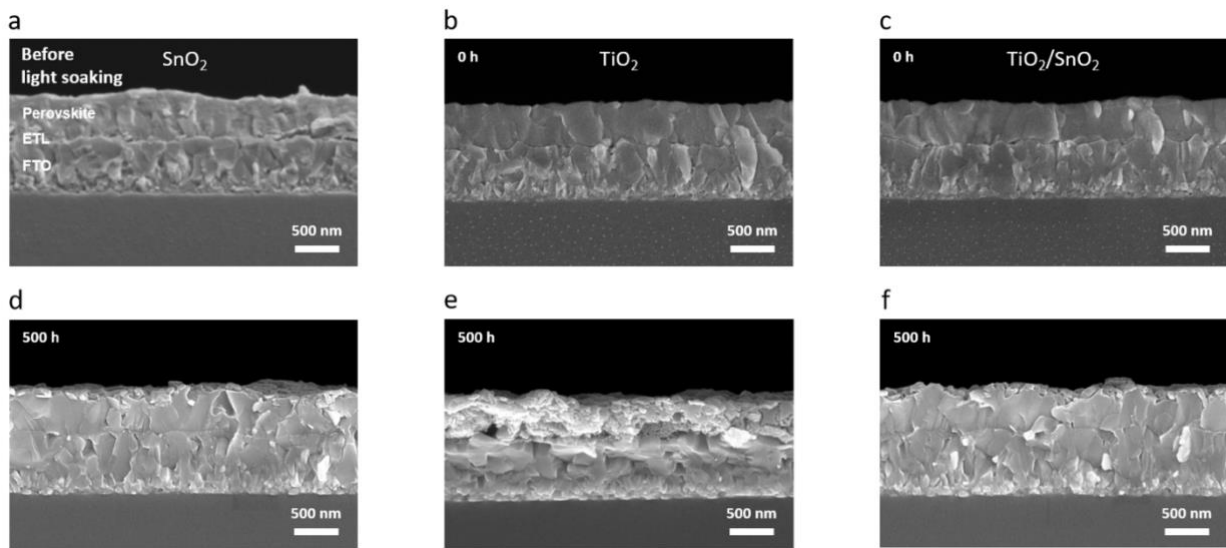
Fig 2.3. Cross-sectional SEM images before light-soaking perovskite samples with (a) TiO_2, (b) SnO_2, (c) TiO_2/SnO_2, and after light soaking with (d) TiO_2, (e) SnO_2, and (f) TiO_2/SnO_2.

To confirm this analogy, powder X-ray diffraction (XRD) and ultraviolet-visible (UV-VIS) spectroscopy have been conducted on light-exposed perovskite samples as demonstrated in Fig. 2.4. The XRD analysis was conducted on samples before light-soaking (Fig 2.4a) showing roughly equal initial PbI_2 peaks for all ETLs at 12.7 ° due to the excess PbI_2 in the perovskite recipe. After light-soaking (Fig 1.4b) the analysis shows a relatively higher increase in the PbI_2 peak at 12.7 ° in the TiO_2 sample when compared with SnO_2 and TiO_2/SnO_2 samples, suggesting perovskite decomposition as seen in Fig. 2.4b. Moreover, the UV-VIS analysis was carried out before and after light-soaking (Fig. 2.4c and d) for 500 h. The UV-VIS analysis clearly shows that the absorbance had in fact decreased for TiO_2 samples throughout the exposed light-spectrum (600 to 850 nm) being consistent with the SEM and XRD result.
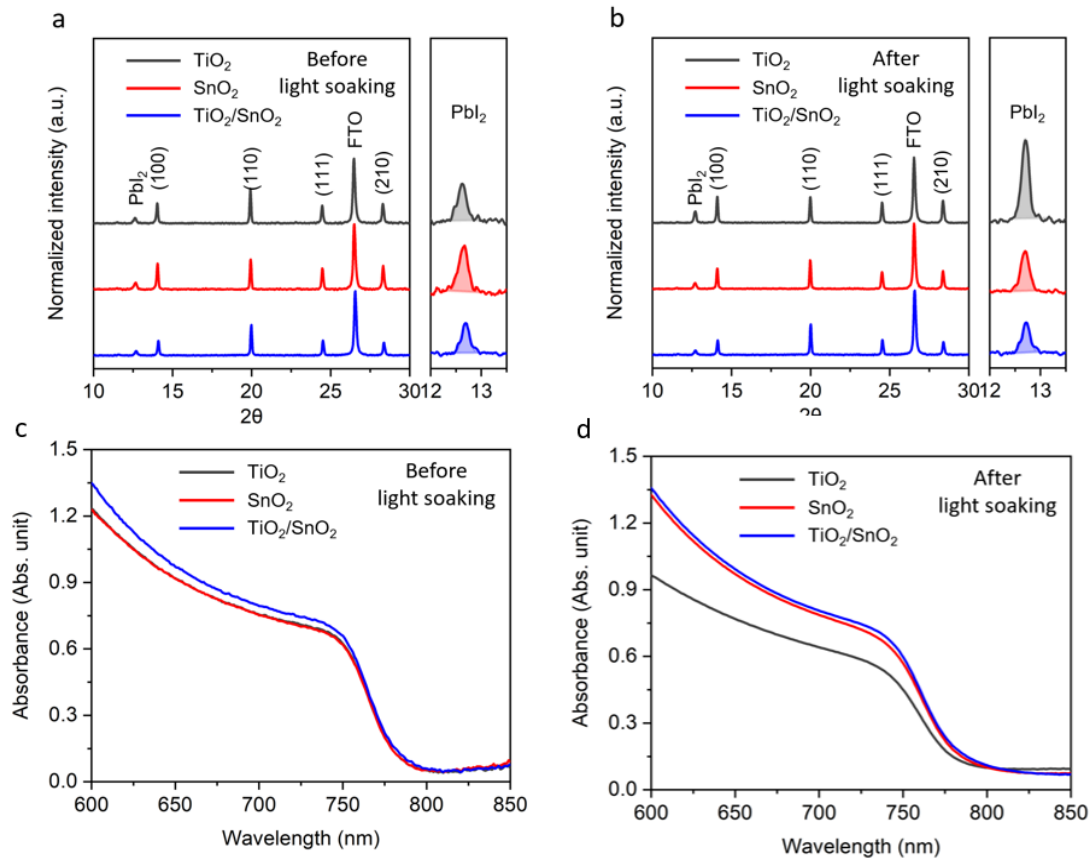
Fig 2.4 XRD spectra for 50 h operated of fully fabricated PSCs with different ETLs (a) before and (b) after light soaking. UV-VIS absorbance spectra for 500 h light-soaked perovskite films for TiO2, SnO2, and TiO2/SnO2 ETLs (c) before and (d) after light soaking.

Energy band diagram analysis was obtained for TiO_2, SnO_2, and TiO_2/SnO_2 as shown in Fig. S2.5. The energy band structure was measured by ultraviolet photoelectron spectroscopy (UPS) and optical bandgap measurement (Fig. S2.6,2.7). The conduction band edge of SnO_2/TiO_2 (-3.70 eV) is approximately the same as SnO_2 (-3.71 eV). However, the Fermi-level of TiO_2/SnO_2 (4.01 eV) is more aligned with TiO_2 (3.9 eV). We note that the different Fermi-levels between TiO_2/SnO_2 and SnO_2 could be due to the thin thickness (~10 nm) of the SnO_2 films. Due to the small thickness, the Fermi-level could be impacted by the underlying TiO_2 film. This phenomena is observed similarly for MoO_X where the Fermi-level of thin films was affected by the underlayer film.[126] We construct an ETL/perovskite interface band diagram as shown in Fig. 2.5 for the bilayered TiO_2/SnO_2 configuration. Our band analysis demonstrate how the SnO_2 could act as a potential barrier that prevents electrons in TiO_2 conduction band from recombining with holes in the perovskite layer. It was reported that when charge recombination occurred at the TiO_2/perovskite interface, perovskite will be decomposed and an increase of PbI_2 content would occur, which is consistent with our XRD

result (Fig. 2.4b).[113], [115] Thus, we presume that the SnO_2 plays a role as a passivation layer to suppress the degradation on the perovskite, resulting in high stability under the light illumination. In addition to stability improvement, TiO_2/SnO_2 bilayers results in improved PV performance when compared with TiO_2 and SnO_2 PSC devices (Fig. S2.8). The *IV* hysteresis was measured for each condition (Supporting information Fig. S2.9, Table S2.2). The hysteresis was suppressed in the TiO_2/SnO_2 sample while the TiO_2 sample suffered the most. The lower hysteresis index could be due to a reduced interfacial charge accumulation by adding SnO_2 layer.[113]
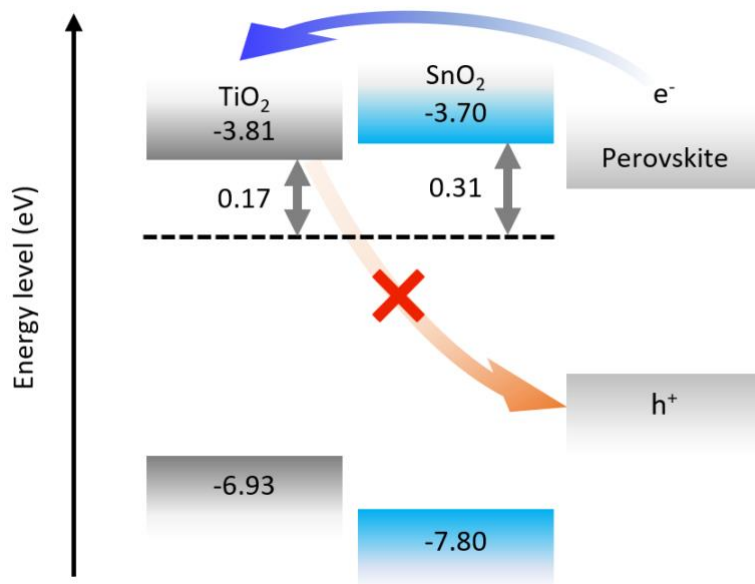
Fig 2.5 Energy diagram of the ETL/perovskite interface demonstrating the passivation effect of SnO_2 in the bilayered configuration (TiO_2/SnO_2).

2.3   Conclusion

We investigated perovskite degradation characteristics based on TiO_2, SnO_2, and TiO_2/SnO_2 underlying ETLs. Our MPPT testing showed strong performance decline in PSCs with TiO_2 whereas PSCs with SnO_2 and TiO_2/SnO_2 showed no significant drop over the course of 1000 h. Further, a series of characterizations were done on perovskite films to gain insight on stability trends observed with the different ETLs. TiO_2 sample characterizations after light-soaking show a prominent decline in charge dynamic processes as interpreted from PL peak and lifetime drop. Moreover, SEM images clearly show a morphological deterioration of the perovskite film after light-exposure. These trends were not observed with SnO_2 and TiO_2/SnO_2 samples demonstrating the passivation ability of SnO_2 films. Energy band diagram indicated the suppression of the charge recombination at the TiO_2/perovskite interface by SnO_2 passivation. This result indicates that the photostability can be enhanced by preventing charge recombination at the ETL/perovskite interface. Moreover, the results demonstrated in this work reinforces the superiority in performance of bilayered TiO_2/SnO_2 electron transporters could achieve while retaining the stability of the devices.

Chapter 3

Stable perovskite solar cells using tin acetylacetonate based SnO$_2$ electron transporting layers

Self-passivated SnO$_2$ as an electron transport layer has shown potential mainly due to the enhanced electron transfer, stability, and reduced hysteresis device features. Here we report on novel, non-colloidal tin oxide precursors based on acetylacetonate (one halide free and two halogenated with Cl and Br respectively). We explore the unique film morphology acquired from the non-colloidal precursors and the improved device performance they yield. Our results show that the halide residue in the films play an impactful role in the thermal durability of the fabricated SnO$_2$ film, as well as providing a passivation layer. Moreover, our optimized SnO$_2$ films, achieved an unprecedented power conversion efficiency of 22.19% in planar perovskite solar cells (21.4% certified by Newport), and once upscaled to large-area modules, 16.7% devices based on 15 cm^2 area were achieved.

Authors: Mousa Abuhelaiqa, Sanghyun Paek, Yonghui Lee, Kyung Taek Cho, Sung Heo, Emad Oveisi, Aron Joel Huckaba, Hiroyuki Kanda, Hobeom Kim, Yi Zhang, Robin Humphry Baker, Sachin Kinge, Abdullah M. Asiri, and Mohammad Khaja Nazeeruddin.

3.1   Introduction

Self-passivated SnO_2 as an electron transport layer has shown potential mainly due to the enhanced electron transfer, stability, and reduced hysteresis device features. SnO_2 based ETLs have been extensively used due to its high conductivity and superior charge collection ability compared to TiO_2 ETLs [81], [119], [127]. SnO_2 has a wide bandgap ranged between 3.6 to 4.1 eV, and its favorable conduction band edge in relation to perovskites makes SnO_2 a good candidate to overcome challenges which occur particularly with c-TiO_2 ETLs [128]. We have seen in Chapter 2 the impact of a bilayered TiO_2/SnO_2 and its impact on improving performance and preserving long-term stability at MPPT. In this chapter, we shed light on the SnO_2 thin film, particularly the importance of self-passivating halide components present.

Previously, high-temperature annealing was used to form uniform SnO_2 layers with minimum pinholes. However, this had posed a challenge due to the metal-like nature shown in degenerate semiconductors, i.e., carrier density of non-doped SnO_2 is ca. 10^{20} cm^{-3} (in the range of semimetals.) The semimetal nature consequently generate a serious shunting pathway which decreases the fill factor (FF) and open-circuit voltage (V_{oc}) [129], [130]. Lee *et al* demonstrated previously that the low PCE is due to the deteriorated hole-blocking ability of the SnO_2 ETL caused by loss of the self-passivating components such as $SnOCl_2$ and residual precursor of tetrakis-dimethyl-amine-tin (TDMASn) [131], [132]. By using different precursors and depositing them with various techniques such as spin-coating and atomic layer deposition methods, Lee *et al* proved the advantages of the low-temperature process are not limited to preventing pin-holes but also to electrically passivate the SnO_2 ETL. [131], [132]. In this work, we further study the role of passivation agents by investigating elemental and morphological SnO_2 film properties and device performance using tin acetylacetonate based precursors for SnO_2. To better understand the role of halides, one of the chosen precursors is halide-free and two are based on chloride and bromide respectively.

We explore the unique film morphology acquired from the non-colloidal precursors and the improved device performance they yield. Our results show that the halide residue in the films play an impactful role in the thermal durability of the fabricated SnO_2 film, as well as providing a passivation layer. Sample preparation procedure and characterization information could be found in sections 6.2.1 and 6.2.2 respectively in Chapter 6. Moreover, supplementary experimental information could be found in section 6.2.3 in Chapter 6.

3.2   Results and discussion

Fig. 3.1 shows the device architecture of a planar perovskite solar cell consisting of fluorine-doped SnO$_2$ (FTO)/c-TiO$_2$/SnO$_2$/perovskite/spiro-OMeTAD/gold layers. In our previous work, we confirmed that the 'Type 1' passivation ETL by combining a c-TiO$_2$ underlayer with the passivated tin oxide (PTO) top layer provides better hole-blocking ability than a single passivated SnO$_2$ layer, which resulted in the further enhanced PCE.[21,24] For tin oxide layers, we investigated three metalorganic tin precursors from the same family tin(II) bis(acetylacetonate) (hereafter Acac), tin(IV) bis(acetylacetonate) dichloride (hereafter Cl2) and tin(IV) bis(acetylacetonate) dibromide (hereafter Br2) with DMF as a solvent.
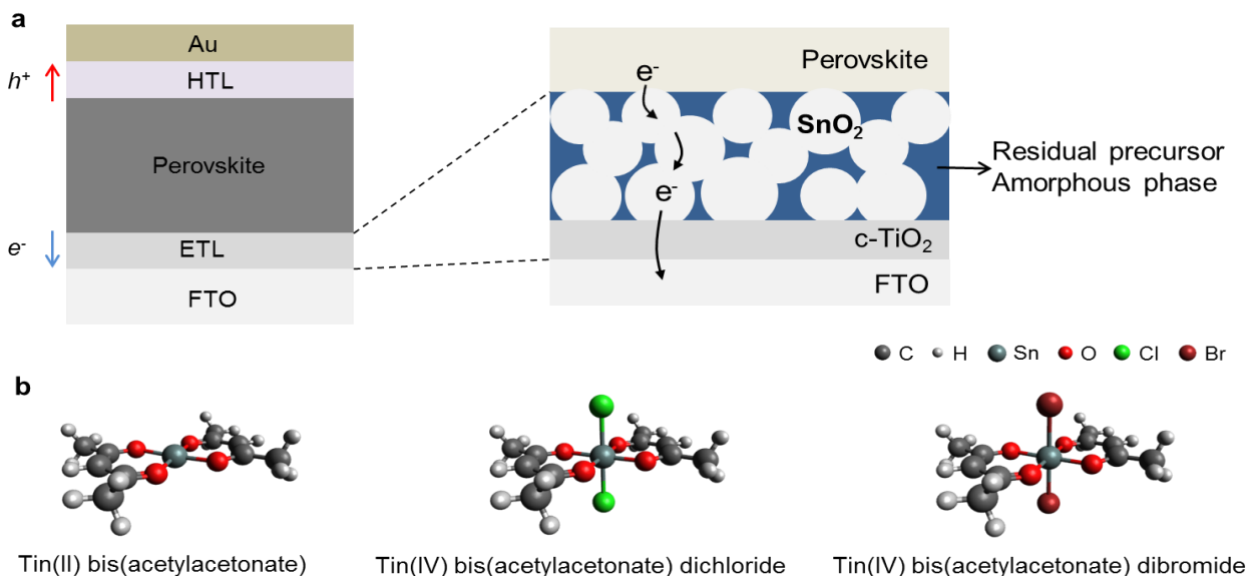
Fig. 3.1 Device structure**.** (a) Schematic of the planar-type perovskite solar cells using bi-layered electron transporting layers of c-TiO$_2$/SnO2. (b) Tin acetylacetonate based precursors used in this work.

The surface morphology of the SnO$_2$ films is characterized with transmission electron microscopy (TEM). Films are prepared by dropping precursor solutions on a carbon support grid and heat-treated at 180 °C for 1 h in air. Pairs of bright field (BF) and dark field (DF) TEM images and corresponding selected area electron diffraction pattern (SAEDP) are presented in Fig. 3.2. The SAEDP show reflection bands for [110], [101], [200], and [211] index planes for all films corresponding to rutile-type SnO$_2$. Moreover, the bright and dark spots in the BF represent low and medium crystallinity

domains respectively in the film. The acquired TEM images indicate the co-presence of crystalline and amorphous phases in the SnO_2 films, a property which Lee *et al* previously observed in SnO_2 films prepared with colloidal precursors such as $SnCl_4$ [119] and atomic layer deposited TDMASn [131] at low temperature. We monitored the composition of the films using Energy dispersive x-ray spectrometry mode in scanning TEM (EDXS-STEM). The high-angle annular dark-field (HAADF) TEM image at low resolution (Fig. S3.1) further demonstrates that the layer formed from all precursors are composed of partially crystalline and amorphous regions. In addition, the corresponding elemental mapping show clear signals of Sn and O atoms as seen in Fig. S3.1, with Cl and Br signals from the Cl2 and Br2 films respectively. These results indicate that the prepared films are comprised of Sn and O elements, as well as residual halogenated by-product after post-annealing at 180 °C for Cl2 and Br2. High-resolution (HR) TEM images are shown in Fig. S3.2. For the Acac film, plenty of pinholes and randomly sized crystallites are observed. On the other hand, other precursor films have compact surfaces with an average crystallite size of 2 nm and 1 nm respectively for Cl2 and Br2.
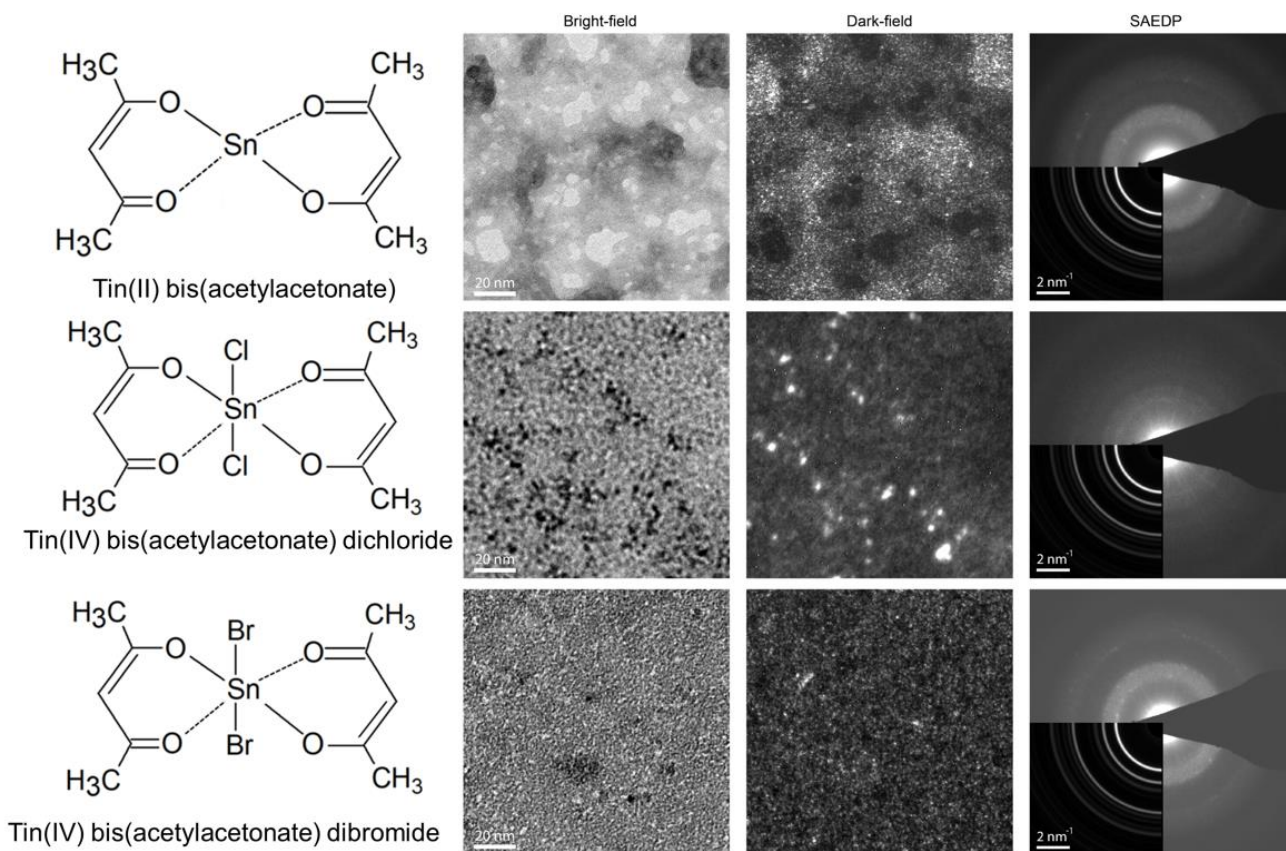
Fig. 3.2 Characterization of the SnO$_2$ layer annealed at 180 °C. Bright-field (BF) and dark-field (DF) TEM images of SnO$_2$ films deposited on a carbon support grid, and corresponding selected area electron diffraction patterns (SAEDP). Simulated electron diffraction patterns are included at the lower left part of SAEDP.
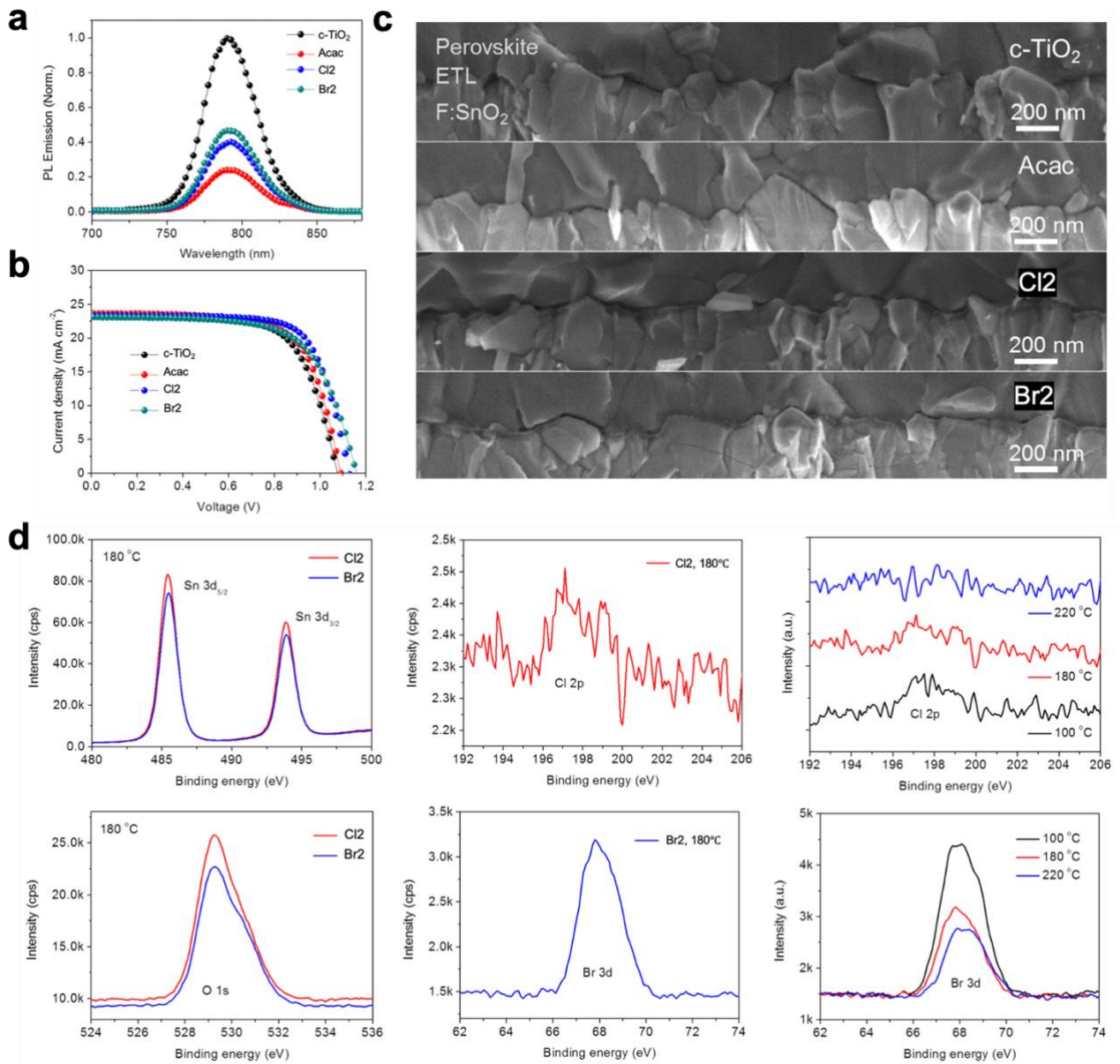
Fig. 3.3 Influence of annealing temperature on the film and device. (a) Photoluminescence (PL) spectra with tin acetylacetonate precursors. (b) *J-V* curves of perovskite solar cells with tin oxide films. (c) SEM cross-sectional images of the complete perovskite solar cells. (d) X-ray photoemission spectroscopy (XPS) spectra as a function of annealing temperature.

To evaluate the compatibility for ETL, we measured photoluminescence (PL) of the bi-layered electron transporting layer (BETL)/perovskite films as seen in Fig. 3.3a. Despite differences in PL intensity, all BETLs show a faster electron quenching efficiency than the c-TiO_2 film. According to the result, Acac shows the fastest quenching rate, and Cl2 and Br2 show slightly slower electron transfer as indicative of the PL peaks. Therefore, a higher PCE was expected with Acac devices, but the device performance demonstrated in Fig. 3.3b shows that the trend of the PL measurement does not match well with the device efficiency. The highest PCE is gained from the Cl2 precursor due to contribution of enhanced *FF* and V_{oc}. For Br2, the high V_{oc} is promising. However, Br2 devices show relatively low *FF* and slightly lower short-circuit current density (J_{sc}) than c-TiO_2. Unlike the PL result, we found that Acac precursor may not contribute to the distinct efficiency enhancement.

To explain this observation, we utilized scanning electron microscopy (SEM) to examine the surface morphology of SnO_2 fabricated with Acac. The full-size image of the complete cells is shown in Fig. S3.3. Moreover, we performed absorbance and x-ray diffraction analysis (XRD) on SnO_2 samples spin-coated with perovskite as seen in Fig. S3.4 and examined perovskite surface morphologies with SEM as seen in Fig. S3.5. The absorbance, XRD pattern and SEM imaging confirm that the perovskite films deposited on SnO_2 have roughly similar thickness and morphology regardless of SnO_2 precursor. However, in the cross-sectional SEM images in Fig. S3.5, Cl2 and Br2 films clearly show an increase in SnO_2 film thickness. However, for Acac devices, there is no observable increase of ETL thickness when compared with c-TiO_2 SEM cross-sectional image. Fig. S3.6 shows SEM top-view images of c-TiO_2 and c-TiO_2/PTO films formed on the FTO substrate. The magnified images show all SnO_2 precursors form a thin and similarly uniform top layer over the c-TiO_2 underlayer. However, different film morphology can be observed for SnO_2 prepared with Acac when the magnification is increased. Randomly distributed big particles potentially caused by the aggregation of precursor are detected on the film surface. The particle sizes range from 1 to 2 um in diameter and induce huge bumps on the perovskite film as seen in Fig. S3.7. The poor morphology in Acac films could be due to the meta-stability of the tin oxidation state. For Acac, the Sn^{2+} metal center is four coordinate with two bidentate acetylacetonate ligands. While for Cl2 and Br2, the Sn^{4+} metal atom is six coordinate with two bidentate with acetylacetonate ligands and two monodentate with halogen ligands. Under this configuration, Sn^{4+} is more likely to be stable in a DMF solution, unlike the case with Sn^{2+} which could be oxidized more readily in DMF. In a preliminary test, we found that Acac dissolves easily in DMF and form a transparent solution, but starts to precipitate in a couple hours as seen in Fig. S3.7.
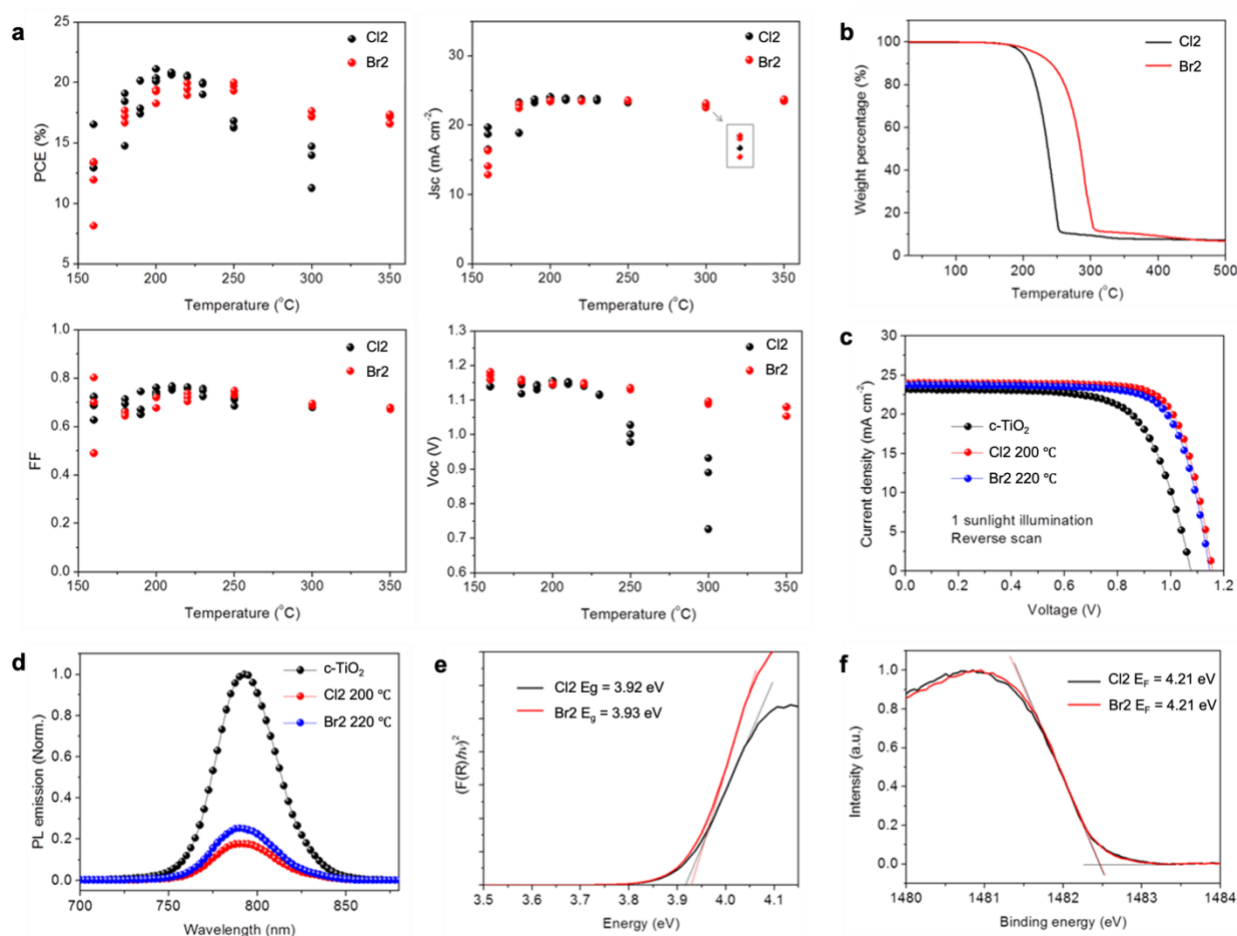
Fig. 3.4 Film and device performance at optimal annealing temperature. (a) Statistical data of the device efficiency with Cl2 and Br2 tin oxide films prepared at differentiated annealing temperature. (b) Thermogravimetric analysis (TGA) spectra. (c) *J-V* curves with optimal annealing temperature. (d) PL spectra of with optimal temperature. (e) Bandgap estimation from reflectance. (f) Calculation of Fermi-level from UPS. $E_F = 40.8 eV$ (He II source) $- E_{cut-off}$..

Whereas for Cl2 and Br2 dissolved in DMF, the solutions do not lose transparency over a month. For Acac, the bumps observed in Fig. S3.7 could potentially provide a shunting route particularly for planar-type cells by forming a thin PTO layer which increase the possibility of pinhole formations. These findings indicate that there are complex challenges associated with Acac in terms of film reproducibility and performance. X-ray photoemission spectroscopy (XPS) analysis was further performed to characterize the Cl2 and Br2 films. Strong peaks at 486 and 494 eV attributed to Sn^{4+}

ions indicate the formation of SnO_2 as seen in Fig. 3.3d. A weak asymmetry shown in all spectra can be reasoned by Sn^{2+} ions originating from oxygen vacancy (V_o) on the SnO_2 surface, which is assumed to be the origin of the high conductivity of the SnO_2 film. [131] Strong asymmetry of the spectra indicating the presence of sub-bonds is also observed in O 1s region (Fig. 3e), which is associated with the binding energy for O-S bond (Sn^{4+}) with higher intensity at 529.2 eV. The smaller peak at 530.5 eV can be associated with oxygen impurities such as OH ligands and water adsorption on the film. [133] In addition, we found a small peak assigned to Cl 2p at 197 eV from the Cl2 film, and a strong peak of Br 3d at 68 eV from the Br2 film. This is in good agreement with the result of EDX analysis in Fig. S3.1. For the Cl2 film, when varying the annealing temperature, the highest intensity peak of the film slightly decreases from 100 °C to 180 °C annealing. Moreover, The Cl bond peak is still present at 220 °C but is significantly minimized. A similar trend is observed from the Br2 film, however, it is noteworthy that the intensity of Br 3d peak remains strong even when annealing at 220 °C.

To find the optimal annealing temperature, we carefully prepared SnO_2 films between 160 °C and 350 °C for Cl2 and Br2. Fig. 3.4a shows a statistical summary of the device efficiency with respect to temperature. The best PCE is found at 200 °C for Cl2, while the highest PCE is obtained at 220 °C for the Br2 device. It should be noted that Br2 devices show a relatively gentle drop of PCEs at high temperatures while Cl2 devices demonstrate a steep decrease after the maximum value. Both devices show a rapid increase of J_{sc} according to the ramping of the temperatures until the maximum J_{sc} is reached (close to 24 mA cm^{-2} at 200 °C). An analogous trend is observed in FF. Although the high FF is shown with the 160 °C devices, we found severe drop of electron transfer as seen in Fig. S3.8. Here, it is noteworthy to remember the film formation of the tin oxide layer from $SnCl_4$ and other chloride-based precursors. Unlike Cl2/Br2 precursors in DMF, $SnCl_4$ immediately reacts with H_2O to form SnO_2 nanoparticles and amorphous $SnOCl_2$ which are not reversibly dissolved in water indicating the solution is in fact colloidal. [127] As with water-based colloidal SnO_2 precursors i.e., AlfaAesar 15% SnO_2, an impressively low temperature processing is required 150 °C. [81] However, surface passivation can potentially occur by $SnOCl_2$ and base sources potentially added for stable dispersion of the colloid, i.e. NaOH, KOH [134], if SnO_2 nanoparticles are synthesized using chlorine based tin precursors (Fig. S3.9). Therefore, despite a lower device performance, the film contains more crystalline SnO_2, therefore, no current loss (decrease of J_{sc}) is found despite film drying at 100 °C. However, Cl2/Br2 precursors do not visibly react with DMF and sustain their solution form, which means smaller or less SnO_2 crystallites can be formed at low temperatures, and more residual

precursor exists on the film which can cause higher series resistance at a low-temperature annealing. This explains the reason of the differentiated behavior shown in Fig. 3.4a,b. With the same reason, high V_{oc} is measured at 160 °C film probably caused by electron accumulation. An unexpected result is found from the V_{oc} trend of Br2 devices. A gradual drop of V_{oc} is seen when increasing annealing temperature beyond 250 °C. Nevertheless, Br2 devices maintain a V_{oc} over 1.1 V even at 350 °C. This result implies that the bromide residue is more strongly bound to the film than chloride counterparts, even at exceptionally high annealing temperature.

To supplement this analogy, thermogravimetric analysis (TGA) was conducted and displayed in Fig. 3.4b. For both Cl2 and Br2 precursors start to lose weight ca. at 150 °C, mainly attributed to thermal decomposition. For Cl2, roughly 90% of weight ca. is lost by crystallization at 250 °C, followed by gradual weight drop implying complete removal of Cl on the film. Br2 shows rather slower weight loss, and the conversion to SnO_2 appears to finish roughly at 300 °C. The subsequent drop that goes up to 500 °C can be attributed due to removal of residual Br. Considering Cl sublimes more easily than Br. The TGA curves further support the result and agree well with EDX and XPS results. *J-V* curves at the optimal conditions are depicted in Fig. 3.4c. PTO layers clearly show better PCEs. The highest PCE of 21.12% is obtained from Cl2. The PCE is slightly lower with Br2 with overall performances over 20%, which are still higher than that with a single c-TiO$_2$ ETL. We confirmed the optimized bi-layered c-TiO$_2$/PTO layers show lower PL emission than the 180 °C films. (Fig. 3.4d) We measured the reflectance of the films, and the determination of optical bandgap (E_g) was calculated by applying the Kubelka-Munk ($\boldsymbol{F(R)}$) method. By plotting $(\boldsymbol{F(R) * h\nu})^{\boldsymbol{2}}$ as a function of energy. Subsequently, an E_g of 3.92 and 3.93 eV for Cl2 and Br2 respectively were estimated. (Fig. 3.4e) Fermi-levels (E_f) were measured by ultraviolet photoelectron spectroscopy (UPS), confirming that both Cl2 and Br2 films have the same E_f of 4.21 eV. The E_g and E_f estimations imply that Cl2 and Br2 films possess similar optical and electronic properties. Additionally, the c-TiO$_2$/Cl2 ETL was tested for a monolithic series module, and a 16.73% PCE was obtained with a 15 cm^2 aperture area (Fig. S3.11).

The champion small cell was fabricated using a two-step deposition method for the perovskite [55]. The best device seen in Fig 3.5a shows promising photovoltaic values in a planar structure with a J_{sc} of 24.78 mA cm^{-2}, a V_{oc} of 1.13 V, a FF of 0.79, and a PCE of 22.19% under 1 sunlight illumination conditions with backward scanning. With forward scanning, the values are slightly lower, and very small J–V curve hysteresis is measured in a planar-type device. We assume the better PCE is from extended light absorption and enhanced perovskite film quality as seen in the EQE and SEM top-view images (Fig. S3.12 and S3.13). We confirmed the J_{sc} value from the solar simulator agrees with the calculated J_{sc}. The device shows excellent performance in the stabilized condition measurement (Fig. 3.5b). We also found BETL based perovskite cells have outstanding long-term stability until 200 days when cells are stored in a drawer without encapsulation (Fig. S3.14). To get reliable data, our cells are measured again at Newport. Although a small loss of V_{oc} is found potentially due to use of a smaller active area and possible degradation in air, a similar and certified PCE of 21.37% on average was confirmed (Fig 3.5 and Fig. S3.14). We further conduct PCE statistics to compare device performances conducted in this work with devices utilizing m-TiO$_2$ in Fig S3.15, demonstrating generally better performance of devices employing SnO$_2$.
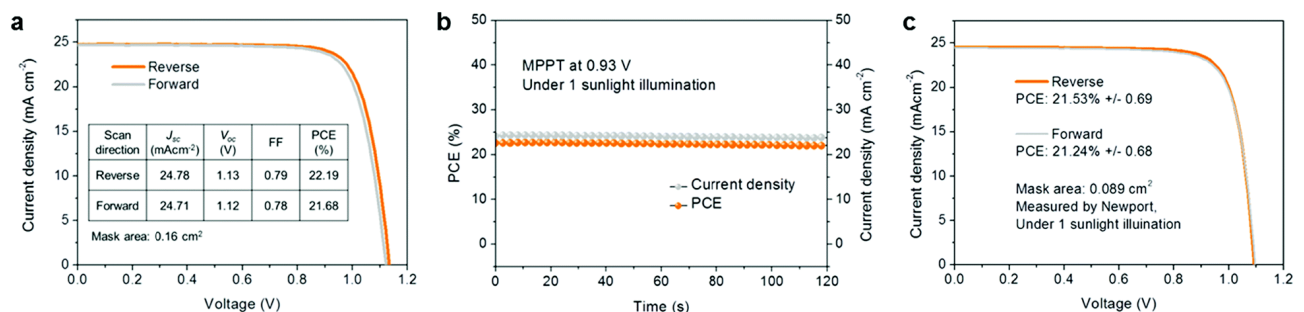
Fig 3.5 Performance of the best device with the c-TiO$_2$/Cl2 BETL. (a) J–V curve hysteresis of the champion cell. (b) Stabilized power output. The values are obtained under a maximum power point tracking condition under 1 sunlight illumination. (c) J–V curve hysteresis measured at Newport.

3.3   Conclusion

We investigated film and device performance with non-colloidal SnO_2 precursors based on acetylacetonate, namely tin(II) acetylacetonate (Acac), tin(IV) bis(acetylacetonate) dichloride (Cl2) and tin(IV) bis(acetylacetonate) dibromide (Br2). We have confirmed with TEM the presence of rutile type SnO_2 in the film with varying degrees of crystallinity, contributing to self-passivation and improved device performance. Moreover, while the Acac precursor produced randomly sized and distributed SnO_2 crystallites, Cl2 and Br2 produced dense SnO_2 films with passivating, halogenated by-product. In addition, we demonstrated the ability of Br_2 to retain the V_{oc} of the devices up to 350 °C annealing post-treatment due to the delayed sublimation of bromide by-product as confirmed with TGA. This finding could extend the application of passivated tin oxide to high-temperature processed perovskites such as lead-free $CsSnI_3$. Ultimately, we confirm the importance of surface passivation for SnO_2, particularly in the scope of perovskite solar cells due to the metal-like nature of pristine crystalline SnO_2. Cl2 and Br2 are proved to provide excellent surface passivation to enhance the hole-blocking ability in electron transporting layers. Our findings highlight the importance of passivation for SnO_2 and suggest inspiring ideas for broader and diverse passivation routes for SnO_2 based solar cells.

Chapter 4

Mixed cation 2D perovskites: a novel approach for enhanced perovskite solar cell stability

The integration of thin 2D perovskite layers at the 3D perovskite/ HTL interface is known to improve the power conversion efficiency and stability of perovskite solar cells (PSCs). In this work, we report a novel approach consisting of mixing two alkyl-based cations that form 2D perovskites (propylammonium iodide (PAI) and octyl ammonium iodide (OAI)) to form mixed-2D halide perovskite layers. The solar cells containing the mixed cations demonstrate enhanced device stability retaining 95% of performance after 1000 h under power point tracking, far exceeding PSC samples with single OAI, 88% and PAI, 80% 2D layers. By cation mixing, the formation of a novel 2D perovskite crystal structure was confirmed by XRD and PL analysis and was shown to have a uniform quasi-2D perovskite state ($n = 2$), a feature not found in single OAI and PAI samples. Notably, the novel morphology of the crystal structure leads to improved carrier dynamics and enhanced PSC stability.

Authors: Mousa Abuhelaiqa, Xiao-xin Gao, Yong Ding, Bin Ding, Zhang Yi, Hiroyuki Kanda and Mohammad Khaja Nazeeruddin

4.1   Introduction

A common approach to enhance PSC stability is to modify the interfaces, specifically the interface between the perovskite film and hole-transporting material, an approach that aims to minimize interfacial recombination by defect passivation [42], [120], [121]. To this end, interfacial 2D perovskite films are ideal candidates due to their electron-blocking, wide bandgap and facile formation on 3D perovskite surfaces containing excess PbI_2 [109], [135]–[137]. Examples of this approach include using precursors such as phenyl ethyl ammonium iodide [100], [138], n-butylammonium iodide[104], N-(3-aminopropyl)-2-pyrrolidinone [139], and 5-ammoniumvaleric acid iodide (5-AVAI) [140], [141]. Such 2D materials could be characterized by their respective lattice structure, which follows a Ruddlesden Popper with $R_2A_{n-1}B_nX_{3n+1}$ formula where R represents an organic (alkyl chain or aromatic ring) component, B is a divalent metal cation, X is a halide anion, and n is the number of repeating inorganic units bound by the A^+ cation [96], [142], [143]. 2D perovskite materials are known to be relatively stable as demonstrated by their exceptional exciton binding energy [96], [97] remarkable photoluminescence yield [144], bandgap tunable properties [98], [145], band-alignment, and defect passivation capability, making them ideal interfacial layers. However, further strategies are necessary to exploit the enhancements in stability provided by 2D perovskites.

The integration of mixed-cation 2D perovskite films in PSCs is an unexplored frontier. Combining two different cations has been thoroughly explored in 3D perovskite systems where different size cations (e.g. methylammonium, formamidinium and cesium)[30], [146], [147] were used to optimize the Goldschmidt tolerance factor [147], [148]. Many studies reported improved PSC stability due to highly uniform perovskite grains with minimal phase impurities. In this work, we apply the cation mixing approach to 2D perovskites, by mixing two alkylammonium based cations with different alkyl chain lengths (octyl ammonium and propylammonium) in an isopropanol solution. Through this approach, we confirm the formation of novel 2D perovskite crystals with a uniform quasi-2D state (n = 2). Moreover, the novel 2D perovskite exhibits unique surface morphology, improved carrier dynamics and extended stability when applied at the interface of the 3D perovskite/HTL in devices. Information on sample and device fabrication can be found in section 6.3.1 in Chapter 6. Moreover, characterization parameters and supplementary information can be in sections 6.3.2 and 6.3.3 respectively in Chapter 6.

4.2   Results and discussion

We introduce mixed cation 2D perovskite films at the interface of the 3D perovskite/HTL by depositing a mixed solution of n-propylammonium iodide (PAI) and n-octyl ammonium iodide (OAI) to form a 2D layer (denoted as OAI+PAI), as illustrated conceptually in 4.1a. Reference samples were based on single cation 2D perovskite samples deposited on 3D perovskites (denoted as OAI and PAI). An initial analysis was conducted with X-ray diffraction (XRD) on the 3D perovskite/2D perovskite FTO films with OAI, PAI and OAI+PAI, as shown in Fig 4.1b and S4.1 for short and full spectra, respectively. As shown in Fig 4.1b, each individual 2D cation produces different low angle XRD peaks that are synonymous with different 2D crystal structures. The peaks of OAI correspond with n = 1 and n = 2 quasi-2D states, whereas PAI correspond to n = 2 and n = 3 quasi 2D states, which is consistent with previous reports [149]–[151]. Notably, the cation mixed 2D perovskite, i.e. OAI+PAI, showed a novel XRD peak pattern not observed in the individual cation samples. Since the OAI and PAI have different alkyl chain lengths of 8 and 3, respectively, a different 2D lattice parameter spacing for OAI+PAI may be expected, which could explain the difference in XRD peak positions. In Fig 4.1(c), the different 2D lattice configurations that could be obtained with the different cation configurations are illustrated. Further crystallographic analysis of the cation mixed 2D perovskite was performed to model lattice parameters using the LeBail method (Fig S4.2, Table S4.1).

Interestingly, the lattice parameter of the *a* axis for OAI+PAI is 43.6 Å, a value between OAI (44.9 Å) [151] and PAI (33.7 Å) [150] as demonstrated in Table S4.1, indicating that the 2D cation mixing approach could be used to tune the lattice distance by combining cations with different lengh alkyl-chains. The LeBail method was further used for OAI and PAI as seen in Table S4.2 and S4.3 respectively. The mixed 2D cation forms a homogenous quasi-2D layer at n = 2, determined from the measured and fitted XRD spectra (Fig S4.2). Moreover, the formation of a 2D perovskite was confirmed by conducting X-ray photoelectron spectroscopy (XPS) for all samples in addition to a control (3D only sample) as shown in Fig S4.3. In the N 1s range, all samples demonstrate a C-N peak (400.8 eV), however, all but the control sample showed a C=N peak (402.2 eV) which is characteristic in 2D perovskite spectroscopy [152], [153].
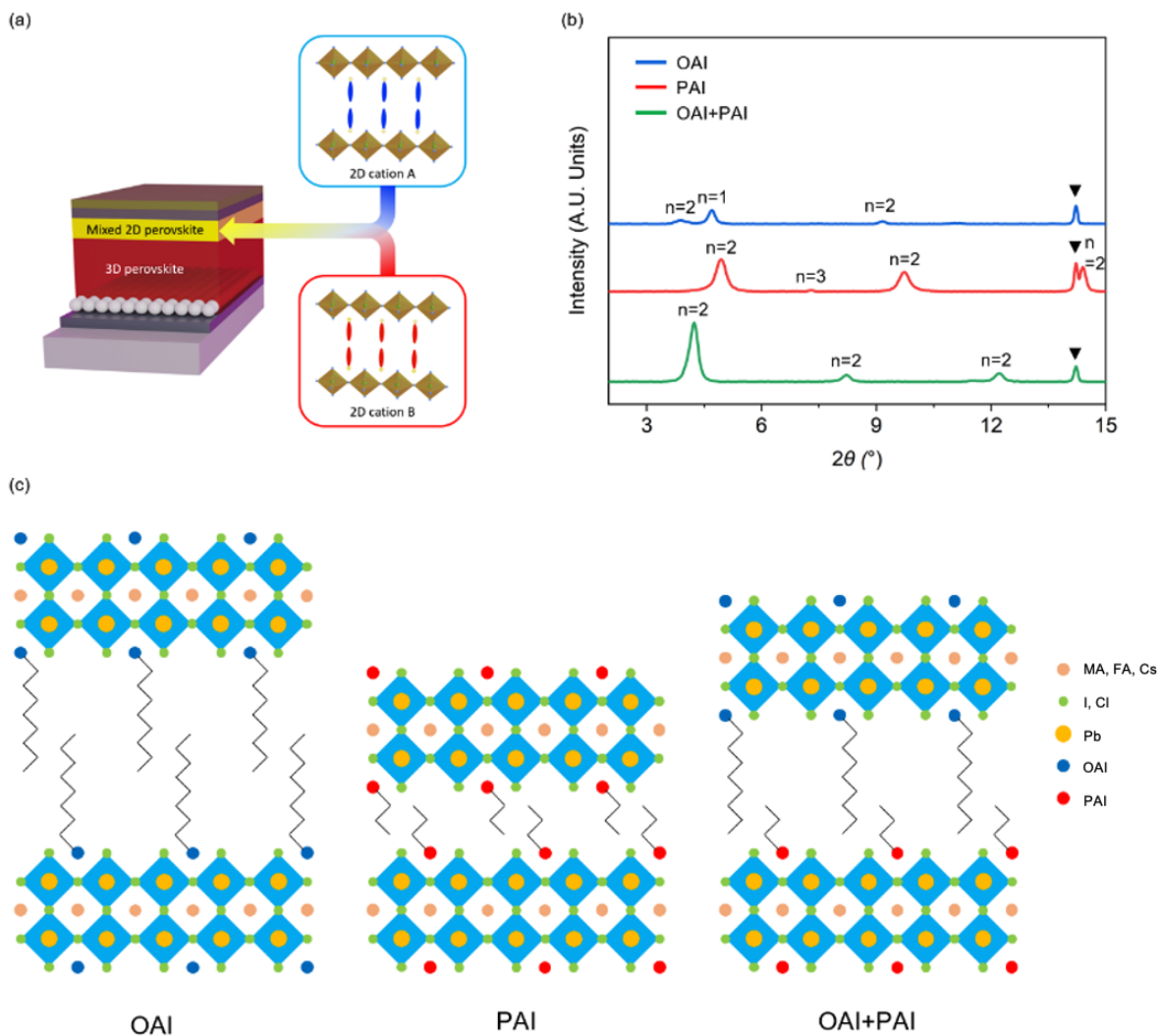
Fig 4.1 (a) Mixed 2D perovskite layer concept, (b) XRD spectra for the 3D/2D perovskite films with OAI, PAI and OAI+PAI, (c) schematic illustrating the quasi-2D state n = 2. perovskite with PAI, OAI and OAI+PAI.

To confirm the presence of the quasi-2D states analogy from XRD, photoluminescence (PL) emission analysis was conducted, as shown in Fig 4.2a, b and c for OAI, PAI and PAI+OAI, respectively. Each sample was structured as glass/3D perovskite/2D perovskite, and the PL scan was conducted from the direction of the 2D perovskite (Fig S4.4 shows the PL emission analysis from the direction of the glass substrate). All samples showed multiple emission peaks, one at approximately 800 nm, which is associated with the 3D perovskite peak in addition to other peaks at high energy, a result which implies the existence of multidimensional (2D and 3D) perovskite layers in all samples. For the OAI sample (Fig 4.2a), there are two peaks at 520 nm and 580 nm corresponding with the quasi-2D perovskite states n = 1 and n = 2. The PAI sample (Fig 4.2b) contains peaks at 580 nm (n = 2) and

630 nm (n = 3), which is consistent with previous studies [149], [150]. Interestingly, the PAI+OAI spectra show only one 2D peak at 580 nm (n = 2), consistent with the XRD pattern. Fig S4.4 shows the PL emission from the glass direction and contains no 2D emission peaks, indicating that the 2D layer is deposited on the 3D perovskite layer. Moreover, when comparing the peak intensity for all the samples, the PAI+OAI sample was found to have the most intense peak, followed by OAI and PAI, indicating a possible passivation effect by mixing different 2D cations [154], [155].
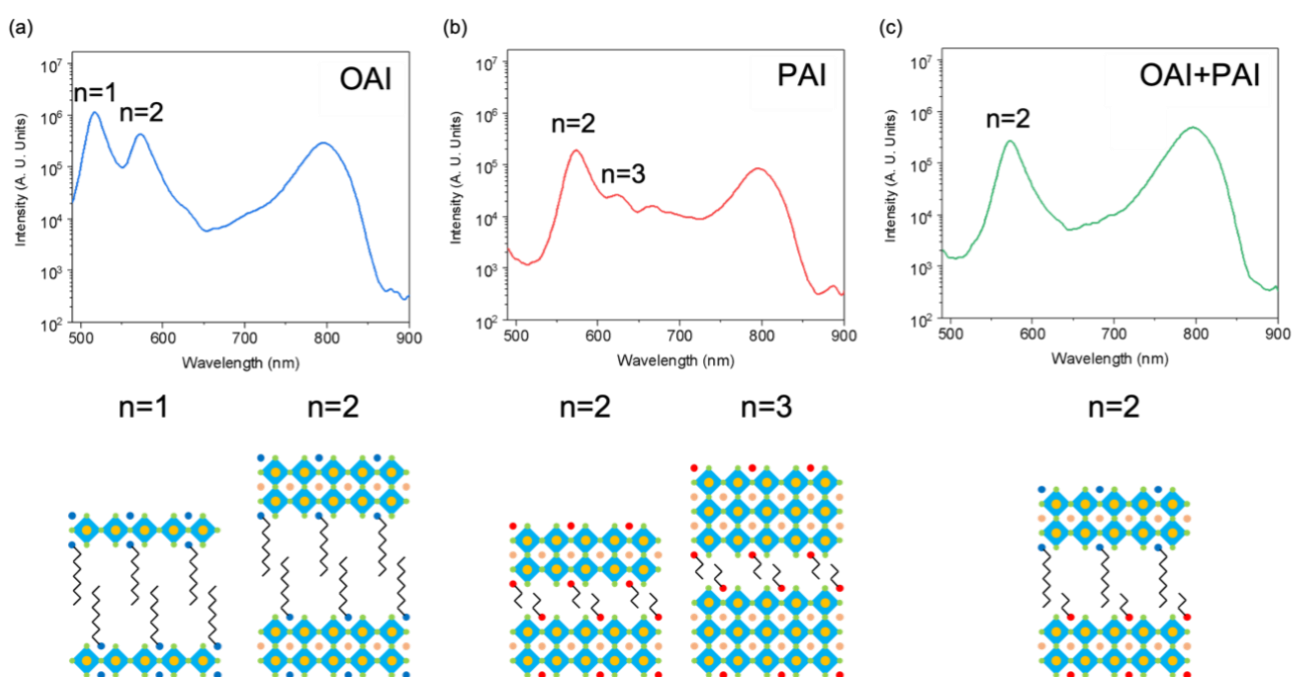
Fig 4.2 Photoluminescence (PL) emission analysis of the 2D/3D perovskite films with the proposed quasi-state 2D schematics for (a) OAI, (b) PAI, (c) OAI+PAI.

Additional PL emission mapping analysis was conducted as shown in Fig 4.3a, b, and c for OAI, PAI, and OAI+PAI, respectively. The maps reveal a similar trend to the PL emission spectra, where OAI+PAI produces the highest intensity spectrum, followed by OAI and then PAI. Surface scanning electron microscopy images were captured to explore the passivation phenomena, see Fig 4.3d, e, and f for OAI, PAI, and OAI+PAI, respectively. The PAI morphology has plenty of pinholes, whereas the OAI morphology possesses fewer pinholes. In comparison, the OAI+PAI sample shows a novel morphological profile with better binding, indicating the elimination of pinholes through 2D cation mixing, which may rationalize the higher PL emission. Note that the thickness of the 2D layers is

essentially the same for the three samples as determined by cross-sectional SEM (Fig S4.5). Time-resolved photoluminescence (TRPL) analysis was conducted as shown in Fig 4.3g, demonstrating the highest carrier dynamics lifetime for OAI+PAI followed by OAI and PAI (Table S4.4), which compliments the PL emission spectra and could be an indication of defect suppression at the 3D perovskite surface [154], [155]. Moreover, ultraviolet photoelectron spectroscopy (UPS) and UV-visible (UV-vis) spectrophotometry were performed (Fig S4.6 and S4.7) in order to construct an energy band diagram for OAI, PAI and OAI+PAI (Fig S4.8). Accordingly, the fermi-level for OAI+PAI is shifted to higher energy compared to OAI and PAI, thus indicating the potential of fermi level tuning with 2D cation mixing and overall enhancement of the carrier dynamics in PSC devices.

The performance of fully fabricated devices was evaluated and the *JV* characteristics and maximum power point tracking are shown in Fig 4.3h and i, respectively. The devices with OAI+PAI achieve the highest power conversion efficiency (PCE) of 21.17% compared to 20.41 and 20.03% for the OAI and PAI devices, respectively (Figure 4.3h). Importantly, the OAI+PAI device retained the highest PCE of 95% over 1000 h compared to 88 and 80% for OAI and PAI devices, respectively. The enhanced photovoltaic parameters presumably result from the unified 2D-quasi states achieved by cation mixing as well as defect passivation indicated by PL emission and decay analysis. We Further demonstrate the hysteresis behaviors and incident power conversion efficiency (IPCE) respectively in Fig S4.9 and S4.10. The OAI+PAI showed the least hysteresis index compared with OAI and PAI samples as well as the highest current.
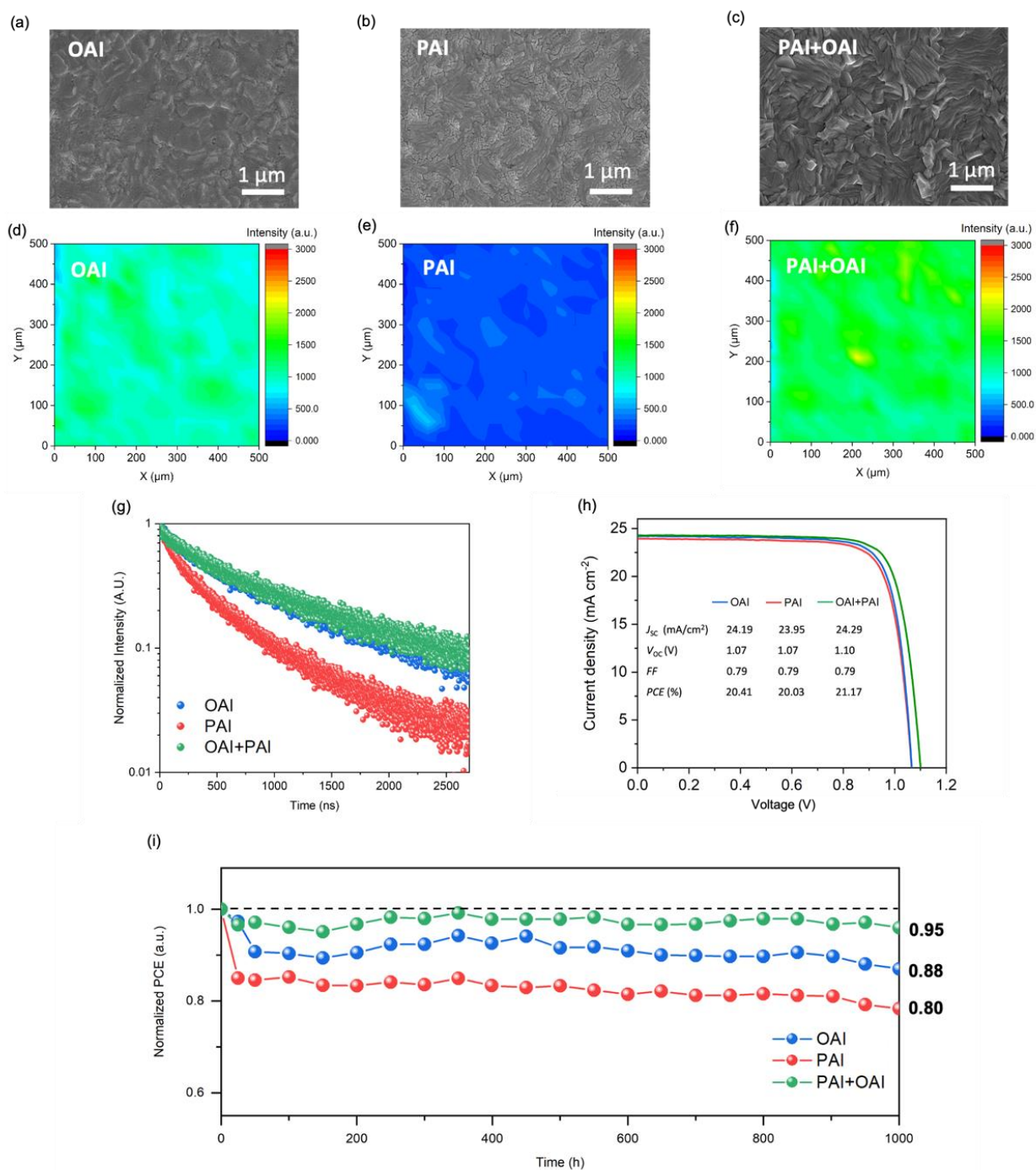
Fig 4.3 Scanning electron microscopy surface image of the 2D/3D (a) OAI, (b) PAI, (c) OAI+PAI perovskite films. PL emission mapping of the 2D/3D (d) OAI, (e) PAI, (f) OAI+PAI perovskite films. (g) Time-resolved photoluminescence spectroscopy (TRPL) for OAI, PAI and OAI+PAI. (h) JV characteristics and (i) normalized PCE versus time for devices with OAI, PAI and OAI+PAI 2D/3D perovskite configurations.

4.3   Conclusion

We investigated the effect of mixing two alkylammonium based cations to form interfacial 2D perovskite films at the 3D perovskite/HTL interface. 2D cation mixing produces a 2D perovskite crystal structure, with a pinhole-free surface morphology and an enhanced set of carrier dynamic parameters, including the highest photoluminescence emission and carrier lifetime among single OAI and PAI, properties which justify the improved photovoltaic performance and stability of PSCs. Notably, the crystal structure of mixed-2D perovskite samples possess unique lattice length parameters and maintain a homogenous quasi-2D state (n = 2). Furthermore, the mixed-2D cations significantly improve device stability under 1 sun irradiation retaining 95% efficiency over 1000 h. This facile approach based on 2D perovskite cation mixing is expected to pave the way for engineering different combination of 2D perovskite-based cation mixing which could simulate highly stable PSCs in the future.

Chapter 5
Conclusions and prospects

The motivation of this thesis is to explore compositional and interface passivation approaches in perovskite solar cells to tackle trap-assisted recombination, and thus, improve photovoltaic parameters. Defects, which are localized in perovskite grain boundaries and surfaces, have been identified not only to reduce the power conversion efficiency and induce hysteresis behavior but also to stimulate degradation in operating perovskite solar cells. Defect passivation are approaches that aim to reduce trap density, and thereby, increase carrier lifetime and other key parameters in perovskite solar cells. The work conducted targets the modification of interfaces and compositions of layers in direct contact with the photo-absorbing perovskite layer, such as the electron transporting and 2D perovskite layers, and provide profound insights to the role of novel layers.

Chapter 2 deals with a light-soaking study on perovskite films that utilize three different ETL configurations based on compact metal oxides; TiO_2, SnO_2 and TiO_2/SnO_2. Initial maximum power point tracking demonstrated that the TiO_2 device experienced PCE deterioration immediately while SnO_2 and TiO_2/SnO_2 devices showed excellent PCE retention over the course of 1000 h. This finding was supplemented by characterizations of fresh and light-soaked perovskite samples to understand light-induced degradation based on ETL. After light soaking, the study reveals that perovskite films employing TiO_2 experienced severe carrier emission and lifetime loss, morphological degradation, and surge of PbI_2, while films employing SnO_2 and TiO_2/SnO_2 showed no significant carrier dynamics and morphological decline. Furthermore, TiO_2/SnO_2 devices produced the highest PCE. Energy-band diagrams revealed that samples utilizing TiO_2/SnO_2 possessed potentially a higher hole-blocking ability due to energy band alignment, that in return, reduce recombination at the ETL/perovskite interface. This study underpins the performance and stability benefit of utilizing TiO_2/SnO_2 electron transporting bilayers. Moreover, the prospect of applying TiO_2/SnO_2 to flexible perovskite solar cells has been raised due to reports demonstrating low-temperature (100 °C) and efficient c-TiO_2 colloid spray-coating [156], improving the scope of application of TiO_2/SnO_2 configurations.

Chapter 3 explores self-passivating halide agents in SnO_2 and their impact on the performance of perovskite solar cells. The study utilizes three different SnO_2 precursors based on acetylacetonate complexes; one without a halogen component (Acac), and two halogenated with chloride (Cl2) and bromide (Br2). Through thermal and elemental investigations, the study correlates a lower presence of halide elements with increasing annealing temperatures. Moreover, the study finds that the Br2 has a higher optimum annealing temperature than Cl2 based on the PCE yield. Further increase of annealing temperature causes a drop of V_{oc} which is correlated with the loss of halide content in the SnO_2 film. Furthermore, transmission electron microscopy revealed that optimum SnO_2 films are

composed of both crystalline and amorphous components reinforcing that halide amorphous components perform better than pristine and crystalline SnO_2. Another outcome of this study reveals that SnO_2 based on Br_2 resists thermal degradation up to 350 °C unlike Cl_2. This result demonstrates the possibility of integrating SnO_2 to perovskite films that require high temperature processing, such as formamidinium lead iodide ($FAPbI_3$) [157], further expanding the applicability of high performing SnO_2 films.

Chapter 3 investigates the mixing of two organic ammonium halides, based on octylammonium iodide (OAI) and propylammonium iodide (PAI), in one precursor solution to fabricate novel 2D perovskite films (OAI+PAI) at the 3D perovskite/HTL interface. Photoluminescence and x-ray diffraction patterns revealed the formation of novel and single quasi-2D perovskite state (n = 2) in OAI+PAI with unique lattice parameters uncharacteristic in single OAI and PAI samples. Furthermore, the OAI+PAI sample showed enhanced morphological binding and improved carrier emission and lifetime, potentially demonstrating a more pronounced passivation effect than single OAI and PAI samples. These results are supplemented by superior PCE, stability, and negligible hysteresis behavior in the mixed OAI+PAI sample. The results disclosed in this work demonstrate a clear advantage in 2D perovskite mixing and could inspire a roadmap of further investigations in mixed 2D perovskite combinations to enhance photovoltaic performance and stability.

While the presented passivation approaches had shown success in improving device performance and stability, the future prospect of their application on commercial settings will rely on further investigations. The introduction of these layers and interfaces could present yet unknown interactions over long-term operations with many parameters to put into consideration. Conducting long-term feasibility studies where the internal working dynamics of each interface is investigated will be the next big step. Moreover, upscaling is another challenge to consider. It had been demonstrated that the fabrication of larger area, perovskite modules reduce the efficiency due to the loss of homogeneity in each participating layer. Fortunately, the advancement of high-area fabrication had picked pace recently with techniques (such as inkjet-printing, slot-die and doctor coating) promoting crystallization control and conformity. Despite the pressing challenges, perovskite photovoltaic technologies have the potential to offsetting energy prices and stimulate further decarbonization efforts.

Chapter 6
Appendices

6.1 Appendix to Chapter 2

6.1.1 Experimental

Complete perovskite solar cell samples were prepared for the JV and stability measurements. Laser scribed FTO glass (Nippon Sheet Glass) was bath-sonicated with detergent diluted in water (1:4) for 20 minutes, in only-water for 10 minutes, and in ethanol and acetone for 5 minutes each. TiO_2 layers were deposited by spray pyrolysis of precursor (0.25 mL of titanium diisopropoxide bis(acetylacetonate) in 4.5 mL ethanol) on FTO at 450 ºC and left 30 minutes for sintering. The SnO_2 layers were deposited by spin-coating SnO_2 nanoparticles diluted in water (3.66%) at 3000 RPM for 30 seconds and annealed at 150 ºC for 30 minutes. The substrates were UV ozone treated for 15 minutes before depositing the perovskite layer. A triple cation perovskite recipe with excess lead $(FAPbI_3)_{0.875}(MAPbBr_3)_{0.125}(CsPbI_3)_{0.1}$ was prepared by adding methylammonium bromide (0.15 M), lead bromide (0.15 M), cesium iodide (0.13 M), formamidinium iodide (1.0 M) and lead iodide (1.2 M) into DMF : DMSO = 4 : 1 (volumetric ratio). The above perovskite solution was spin-coated on top of the substrate at a two-step program set at 1000 and 5000 rpm for 12 and 30 s, respectively. A 100 μL of antisolvent (chlorobenzene) was deposited on the substrate 15 s on the second step of the spin-coating program. The substrate was placed on a heating plate at 100 ºC for 1 h to allow perovskite thermal post-processing. The HTL (spiro-OMeTAD) precursor solution was prepared by dissolving 60 mg of spiro-OMeTAD in 768 μL chlorobenzene, 24 μL 4-*tert*-butylpyridine, 14 μL of bis(trifuoromethane)sulfonimide lihium in acetonitrile solution (517 mg mL^{-1}) and 11 μL of tris(2(1Hpyrazol-1-yl)-4-tert-butylpyridine)cobalt(III) tri[bis(trifloromethane)sulfonimide] in acetonitrile solution (376 mg mL^{-1}). The HTL precursor solution was deposited dynamically on the spin-coating samples at 5000 rpm for 20 s. Subsequently, 70 nm of gold was deposited through a sublimation procedure. Light soaking (for XRD and SEM) samples were prepared by depositing the ETL layer first (TiO_2, SnO_2, and TiO_2/SnO_2 configurations) on FTO substrate. The perovskite layer was deposited on top. The PL samples were similarly prepared, however, the substrate used is glass.

6.1.2 Characterization

The stability test was performed by keeping samples in the dark without encapsulation at 0% relative humidity with nitrogen atmosphere and 25 ℃. Microscopy images were captured by a cold field emission scanning electron microscope (SU8200, Hitachi high-tech. Co.)., with an active area mask of 4×4 mm^2. The scanning step and speed were set at 10 mV and 50 mV/s respectively. UV-VIS spectroscopy was measured by using a Lambda 950S (PerkinElmer, Inc.) instrument. Photoluminescence emission spectra were measured by using LS-55 fluorescence spectrometer (PerkinElmer, Inc.) and an excitation wavelength of 640 nm. Time-resolved photoluminescence spectroscopy was performed by Fluorolog TCSPC with an excitation wavelength of 640 nm (HORIBA, Ltd.). The ultraviolet photoelectron spectroscopy (UPS) equipped with He-I source (hν = 21.22 eV) (AXIS Nova, Kratos Analytical Ltd., UK) was done to determine the valence band energy and Fermi level. The Fermi level of the samples was referred to that of Au which was in electrical contact with a sample in UPS measurements. One dimensional X-ray diffraction (XRD) analysis was carried out using a D8 Advance diffractometer (Bruker Corporation) with Cu Kα radiation ($\lambda_{K\alpha}$ = 1.5418 Å). *I-V* measurements were made using an Oriel VeraSol solar simulator (Newport Corporation) by using calibrator LCE-50 (Centronics). The *I-V* measurement was performed from 1.2 to 0 V.

6.1.3 Supplementary Information

Table S2.1 Proportionality constant (A) and PL lifetime (τ) extrapolated from exponential decay fitting for the time-resolved photoluminescence measurement.

	Before light soaking		After light soaking	
	A	τ	A	τ
	(-)	(ns)	(-)	(ns)
TiO_2	0.916	90.9	0.971	34.0
SnO_2	0.903	91.1	0.940	106.8
TiO_2/SnO_2	0.887	96.6	0.956	93.3

†The equation for the fitting is $y=y_0+A\times exp(-(x-x_0)/\tau)$.
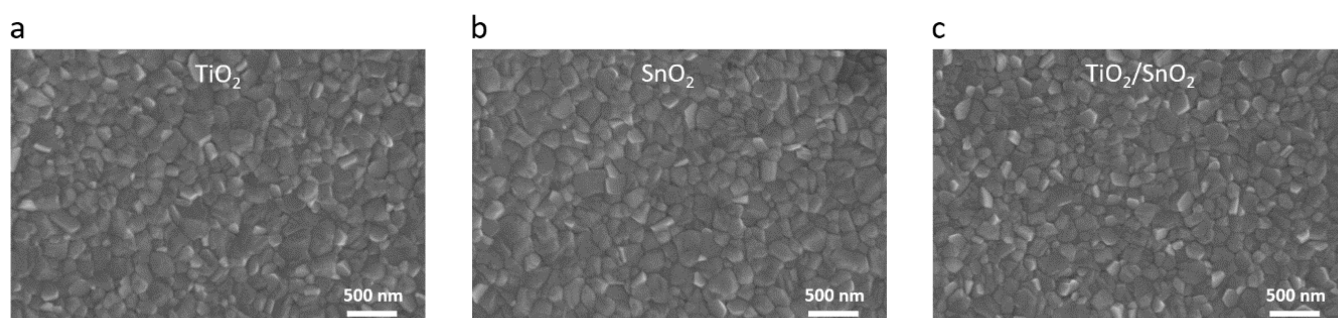
Fig S2.1 Top view SEM images of perovskite film samples on top of (a) TiO_2, (b) SnO_2 and (c) TiO_2/SnO_2 ETLs.
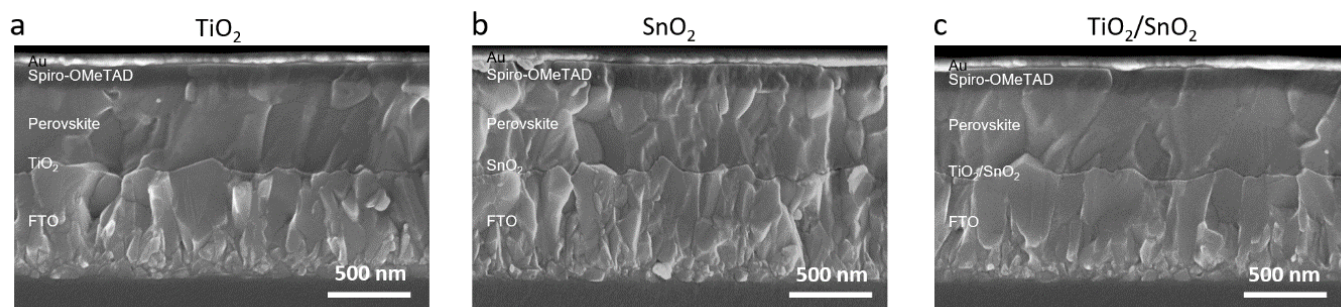
Fig S2.2 Cross-sectional SEM images of fully fabricated PSCs with (a) TiO_2, (b) SnO_2 and (c)TiO_2/SnO_2 ETLs.
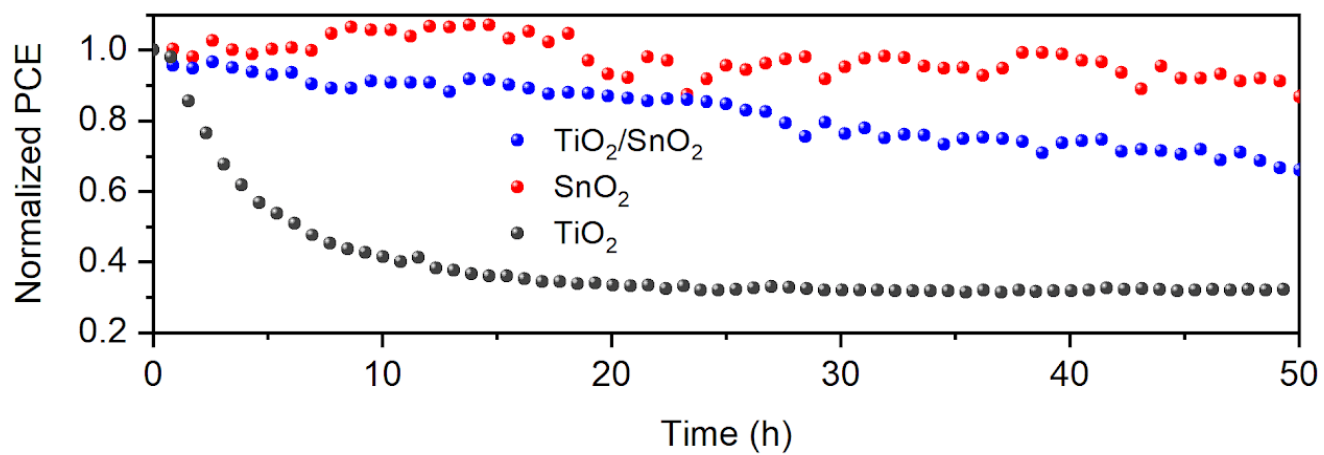
Fig S2.3 Maximum power point tracking (MPPT) under the light irradiation including UV-light.
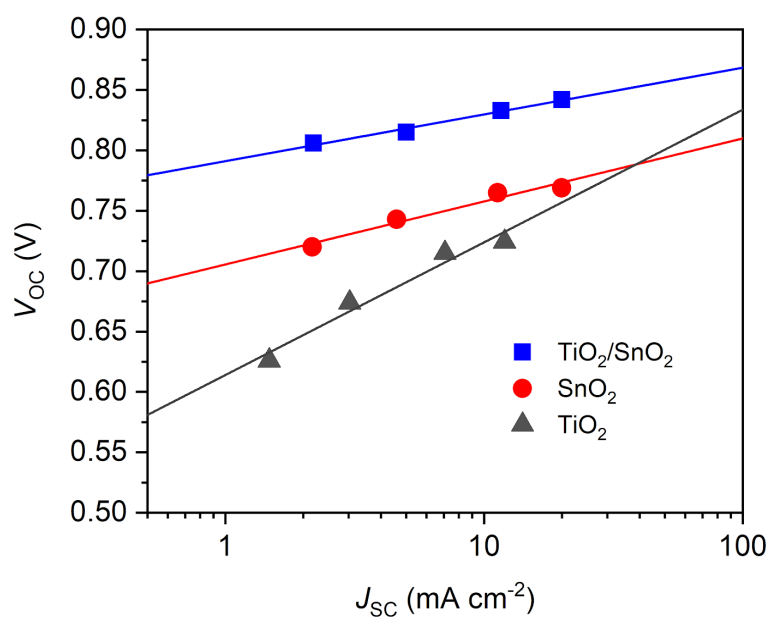
Fig S2.4 V_{OC} plotted against the logarithm of J_{SC} in the PSCs with TiO_2, SnO_2, and TiO_2/SnO_2 after 50 h light soaking.
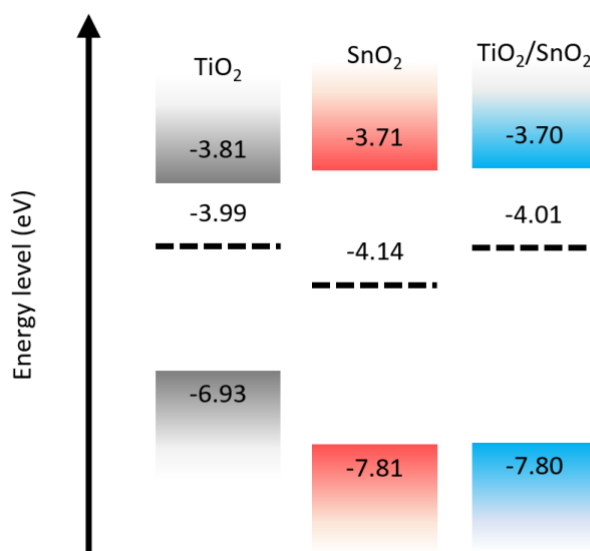
Fig S2.5 Energy band diagram for each electron transport layer. Noteworthily, we found that the Fermi-level for the SnO_2 layer in the bilayered configuration (TiO_2/SnO_2) is higher than sole SnO_2. The higher Fermi-level could increase the V_{OC} of PSCs.
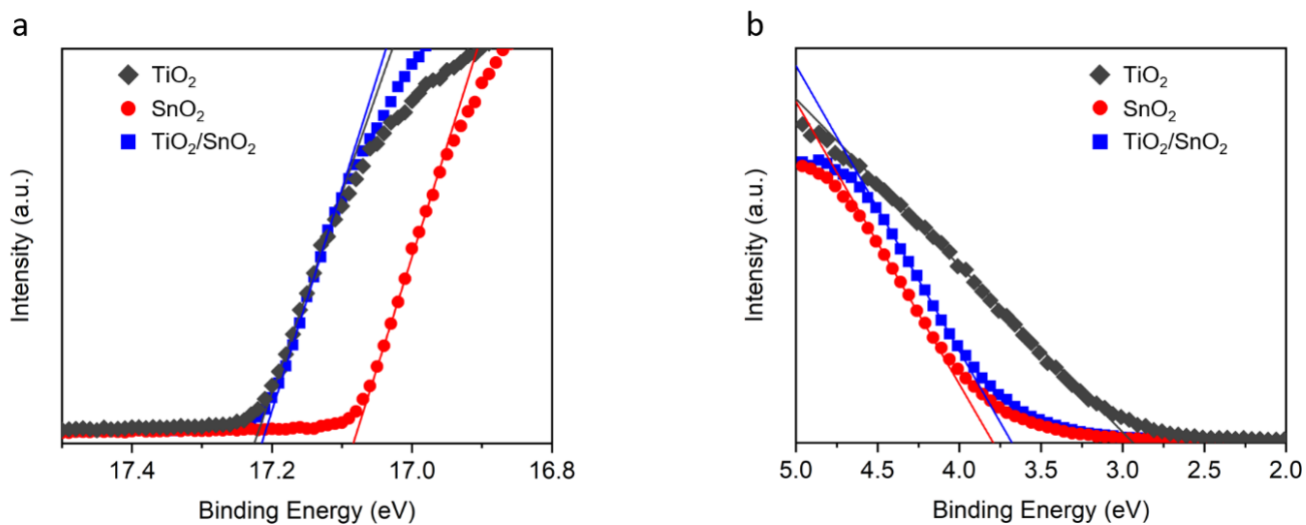
Fig S2.6 UPS spectra utilised for the determination of: (a) work-function (b) valence band for TiO_2, SnO_2 and TiO_2/SnO_2 ETLs.
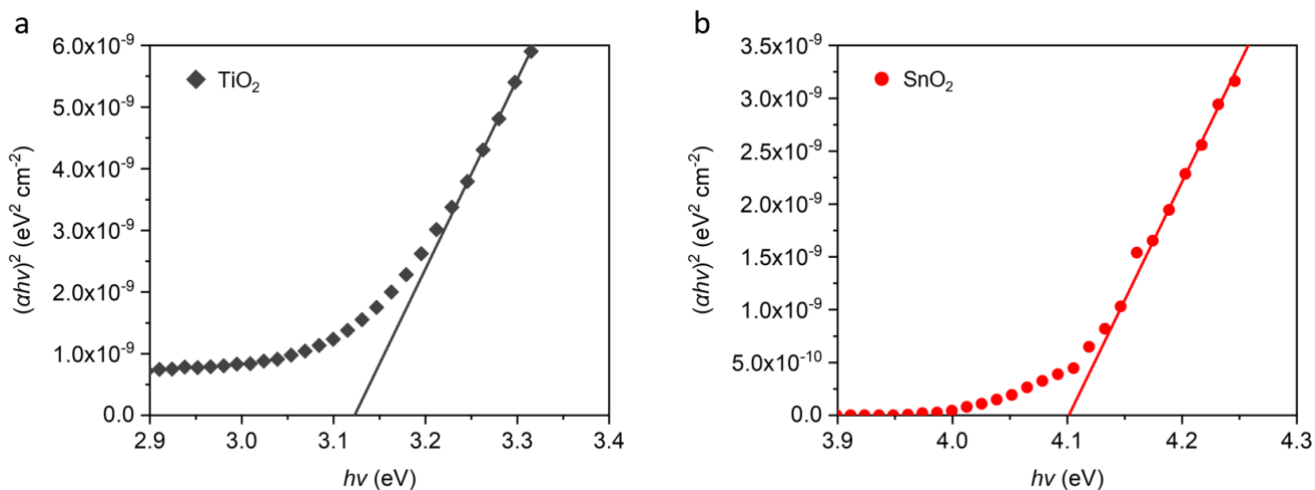
Fig S2.7 Tauc plots obtained from UV-Vis spectra for (a) TiO_2 and (b) SnO_2 films on glass to determine the optical bandgap.
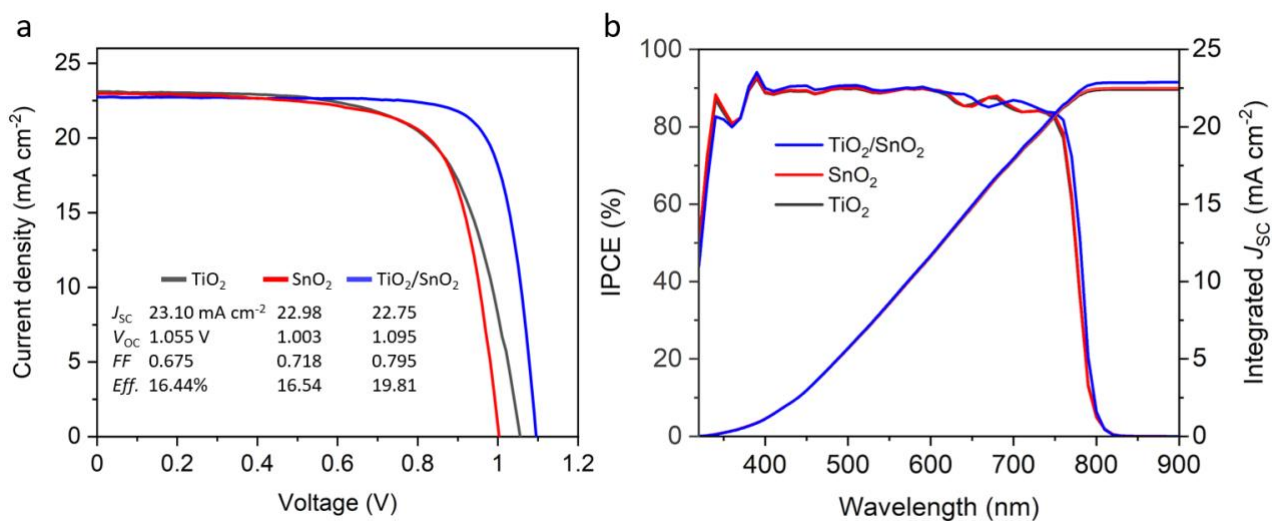
Fig S2.8 (a) J-V curves with reverse scan and (b) Incident photon-to-electron conversion efficiency (IPCE) spectrum and integrated current for devices with TiO_2, SnO_2 and TiO_2/SnO_2 ETLs.
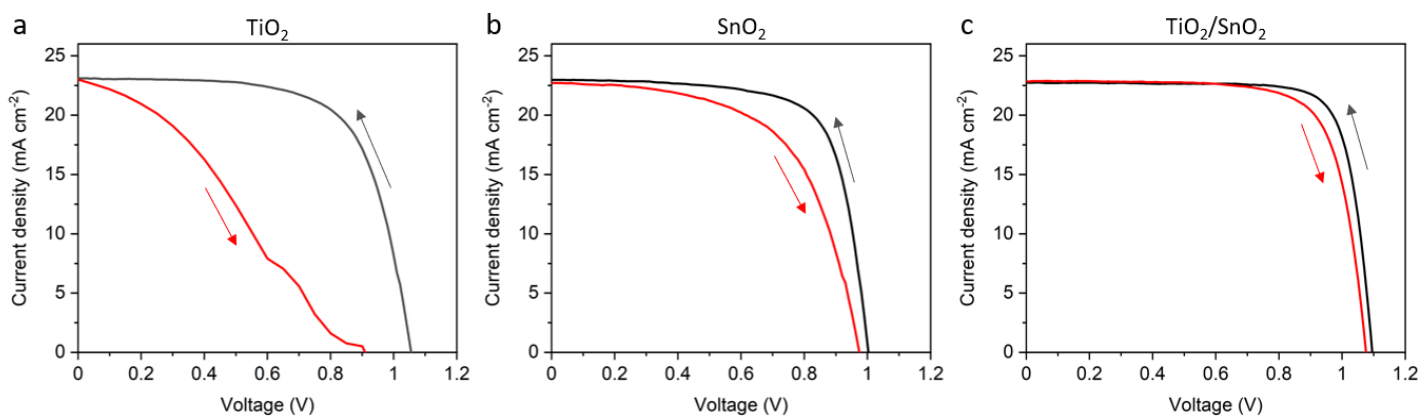
Fig S2.9 *JV* hysteresis of perovskite solar cells with (a) TiO_2, (b) SnO_2, and (c) TiO_2/SnO_2

Table S2.2 Photovoltaic properties of perovskite solar cells for IV hysteresis

ETL		J_{SC} (mA cm^{-2})	V_{OC} (V)	FF	Eff. (%)
TiO$_2$	Reverse	23.10	1.055	0.674	16.51
	Forward	23.00	0.908	0.908	6.51
SnO$_2$	Reverse	22.98	1.003	0.718	16.51
	Forward	22.63	0.963	0.585	12.95
TiO$_2$/SnO$_2$	Reverse	22.75	1.095	0.794	19.77
	Forward	22.84	1.076	0.747	18.23

6.2　Appendix to Chapter 3

6.2.1 Experimental

FTO glass substrates (Nippon sheet glass) were sequentially cleaned with detergent and ethanol. A compact TiO_2 layer was coated by spray pyrolysis deposition on the cleaned FTO substrates heated at 450 °C. SnO_2 layers are prepared by spin-coating a precursor solution of tin acetylaceontate based precursors dissolved in dimethyformamide. 0.1 M $SnCl_4$ aqueous solution was spin-coated at 5,000 rpm for 10 s on the substrates to get ~20 nm thickness. Then the substrates were transferred onto a hotplate and heated between 160 °C and 350 °C for 1 h and cooled down. The $(FAPbI_3)_{0.85}(MAPbBr_3)_{0.15}$ precursor solution was prepared by mixing PbI_2 (1.15 M, TCI), $PbBr_2$ (0.2 M, TCI), FAI (1.05 M, Dyesol), MABr (0.2 M, Dyesol) in a mixed solvent of DMF:DMSO = 4:1 (volume ratio). The precursor solution was spin-coated at 1,000 rpm for 10 s and, continuously at 5,000 rpm for 30 s. During the second step, 100 μL of chlorobenzene was poured on the film at 15 s. Films are post-annealed at 100 °C for 60 min. For the two-step deposition method, PbI_2 (1.3 M) containing 2.5 mol% $PbBr_2$ was dissolved in 1 ml of DMF and DMSO (ratio=4:1) solution at 80 °C. Then the solution was spin coated on the SnO_2 substrate at 3,000 rpm for 30 s, the mixture solution of FAI:MABr:MACl (80:10:10 mg in 1 mL IPA) was spin coated on the PbI_2 substrate at 5000 rpm for 30 s. Films were annealed at 150 °C for 25 min and 100 °C for 30 min. Finally, Spiro-OMeTAD was spin-coated at 4,000 rpm for 25 s. The 70 mM Spiro-OMeTAD solution was prepared by dissolving in chlorobenzene with 4-tert-butylpyridine, Li-TFSI in acetonitrile, and $Co[t-BuPyPz]3[TFSI]3$ (FK209, Dyesol) in acetonitrile at the molar ratio of Spiro : FK209 : Li-TFSI : TBP of 1 :0.03 : 0.5 : 3.3. Devices were completed with a thermal evaporation of 70 nm thickness gold counter electrodes.

6.2.2 Characterization

XRD analysis was carried out using Bruker D8 Advance diffractometer in an angle range of $2\theta = 10$ ° to 40 °. Scanning electron microscopy (SEM) measurements were carried out on ZEISS Merlin at 5 kV, and images were acquired by an in-lens secondary electron detector. Transmission electron microscopy imaging and energy-dispersive X-ray (EDX) analysis were performed on a FEI Tecnai Osiris at 200 kV. This microscope is equipped with a high brightness X-FEG gun and silicon drift Super-X EDX detectors and Bruker Esprit acquisition software. Samples for TEM imaging were prepared via depositing the SnO_2 film on a TEM grid with a carbon support film. The TEM grids were then heat-treated at 180 °C. XPS analysis was done by an equipment (Quantum 2000 system) with Al kα x-ray source (*hv*: 1487 eV) and a hemispherical electron analyzer. The XPS results provide the average chemical information on spatial area of 100 μm diameter and depth of 5~10 nm. Absorbance and reflectance were measured with an integrating sphere using the UV/Vis/NIR spectroscopy (PerkinElmer Lambda 950S). The photoluminescence emission was measured with the Fluorescence spectrometer (PerkinElmer LS 55). TGA analysis (TGA 4000 PerkinElmer) was done at a scan rate of 10 °C/min from 30 °C to 500 °C. The UPS measurements were performed in home-made photoemission spectroscopy system, which consists of ultraviolet source (VUV 5000) and electron analyzer (SES-100) in ultrahigh vacuum (UHV) chamber. The He II source of 40.8 eV, controlled using monochromator, enables to obtain precise electronic structures from UPS spectra.

The solar cell measurement was done using Oriel solar simulator (450W Xenon, AAA class). The light intensity was calibrated with a Si reference cell equipped with an IR-cutoff filter (KG3, Newport), and it was recorded prior to measurement. Current-voltage characteristics of the cells were obtained by applying an external voltage bias while measuring the current response with a digital source meter (Keithley 2400). The voltage scan rate was 100 mV s^{-1} and no device preconditioning such as light soaking or forward voltage bias applied for long time, was applied before starting the measurement. The cells were masked with the active area of 0.16 or 0.89 cm^2 to fix the active area and reduce the influence of the scattered light. EQE was measured with IQE200B (Oriel) without bias light.

6.2.3 Supplementary Information
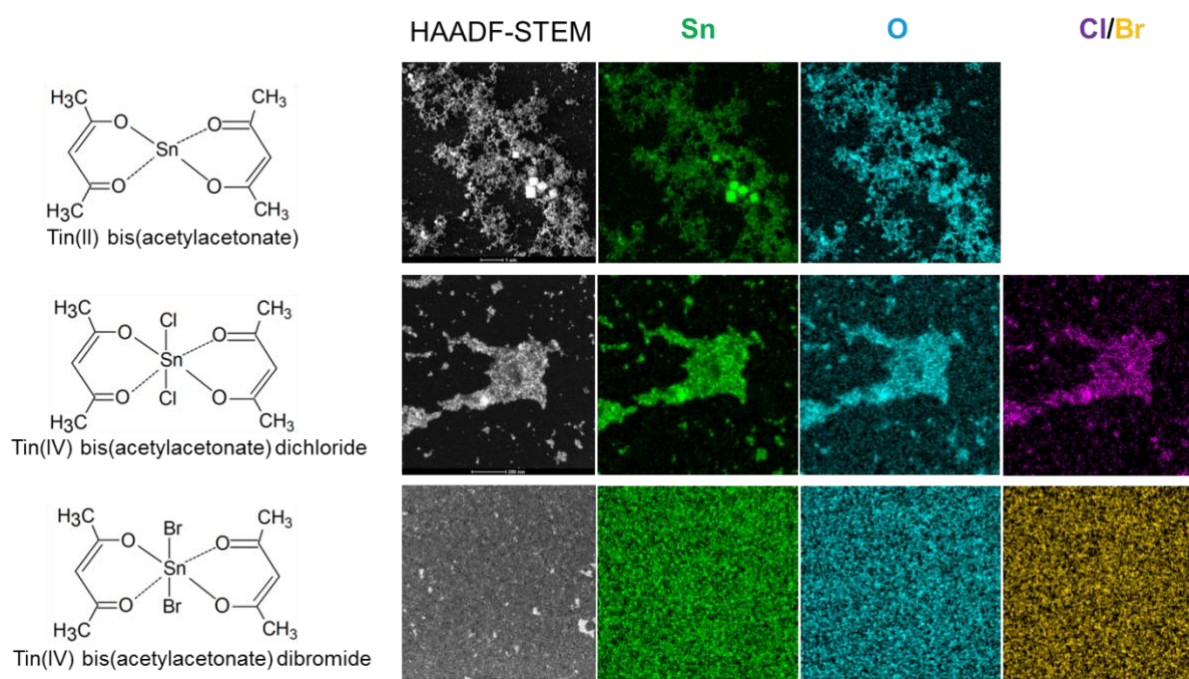
Fig S3.1 Energy dispersive X-ray (EDX) analysis. High-angle annular dark-field (HAADF) scanning TEM image and corresponding elemental maps of Sn, O, Cl and Br of the tin oxide films deposited on a carbon TEM grid.
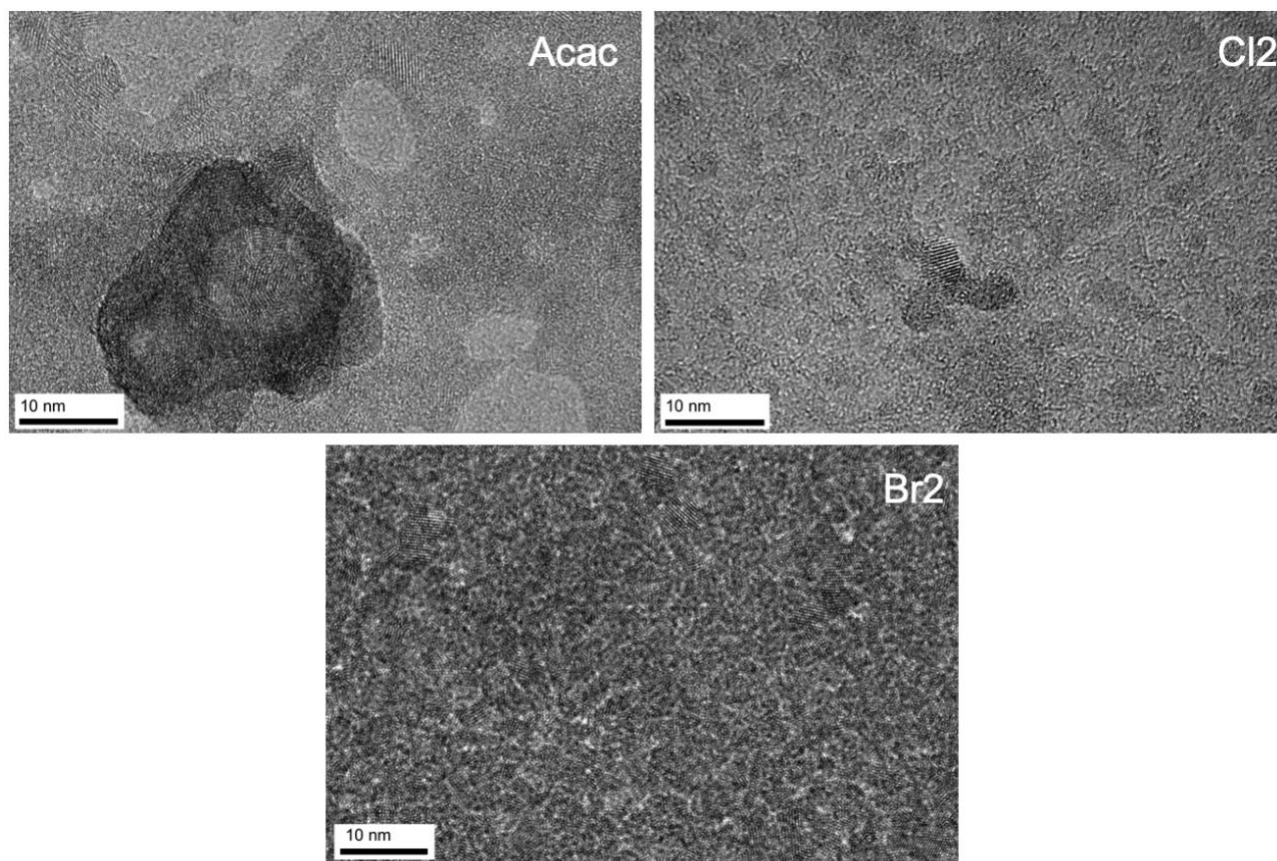
Fig S3.2 High-resolution TEM images of Acac, Cl2 and Br2 annealed at 180 °C.
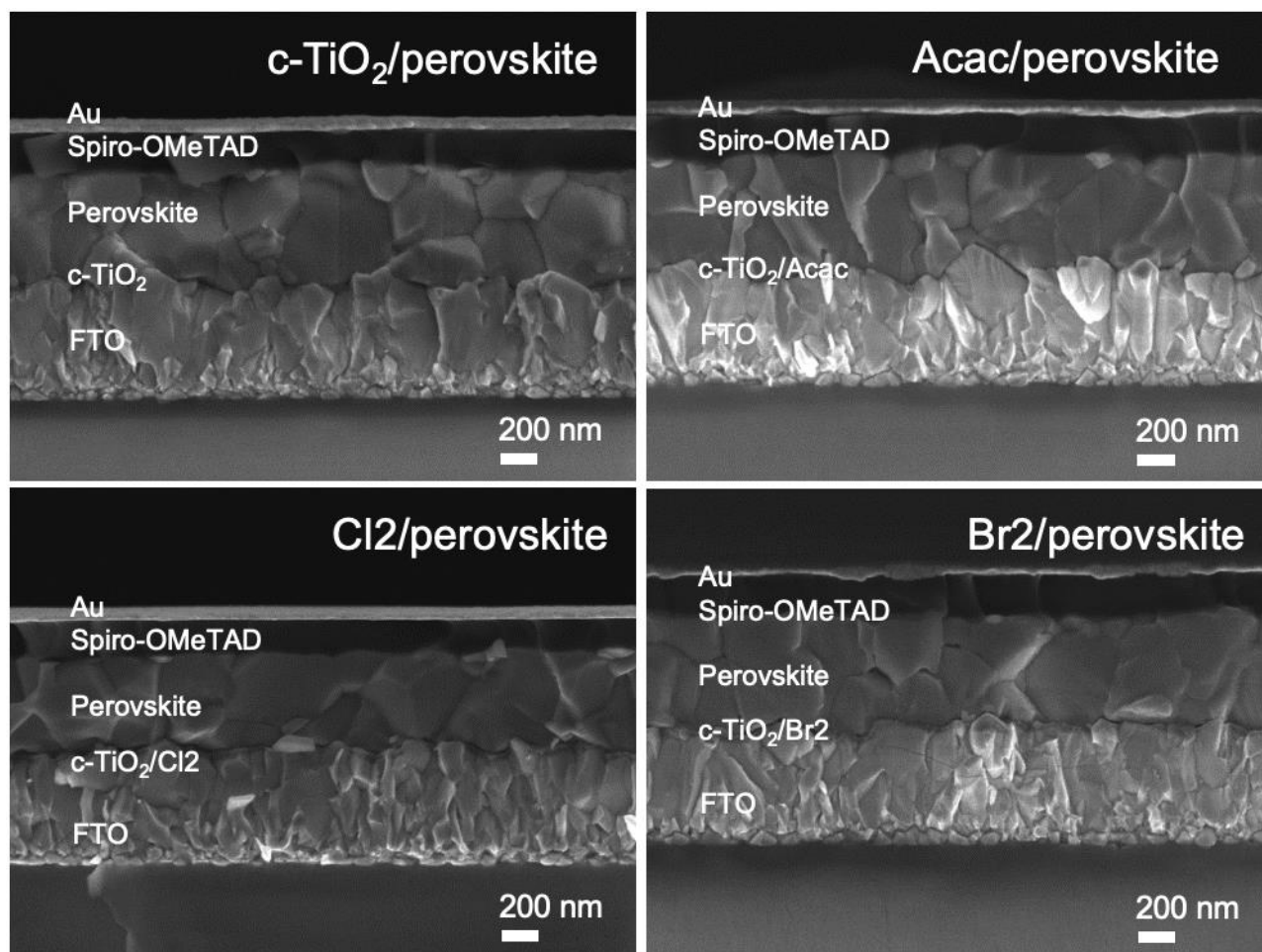
Fig S3.3 SEM cross-sectional images for the complete cells. The thickness of the ETL layer is higher for Cl2/Perovskite and Br2/perovskite than Acac/perovskite and c-TiO$_2$/perovskite.
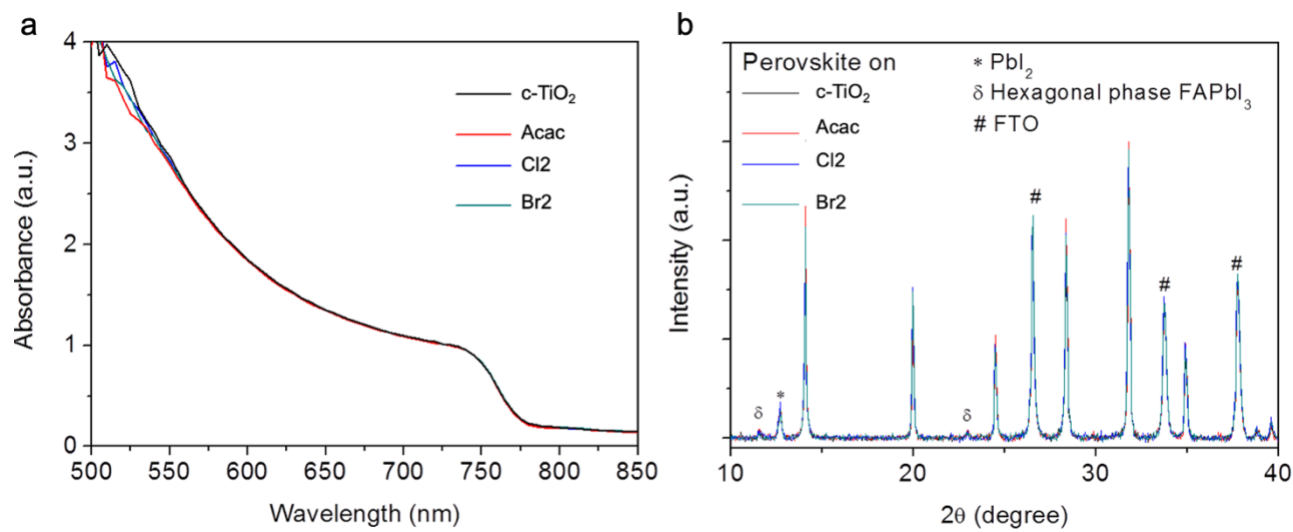
Fig S3.4 Absorbance (a) and X-ray diffraction patterns (b) of the perovskite film on the FTO/ETLs.
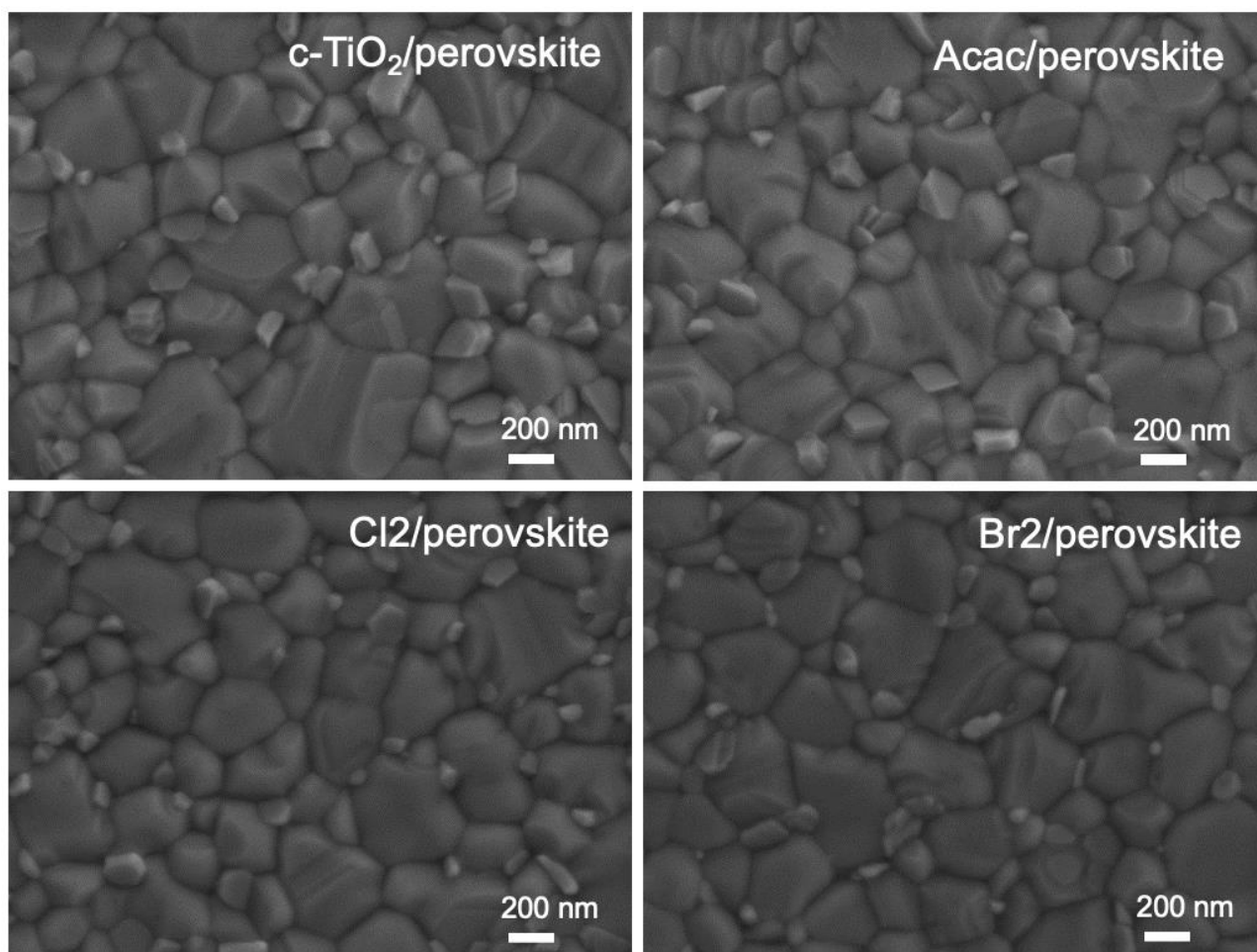
Fig S3.5 Top-view SEM images of the perovskite films formed on c-TiO$_2$, Acac, Cl2 and Br2 films, respectively.
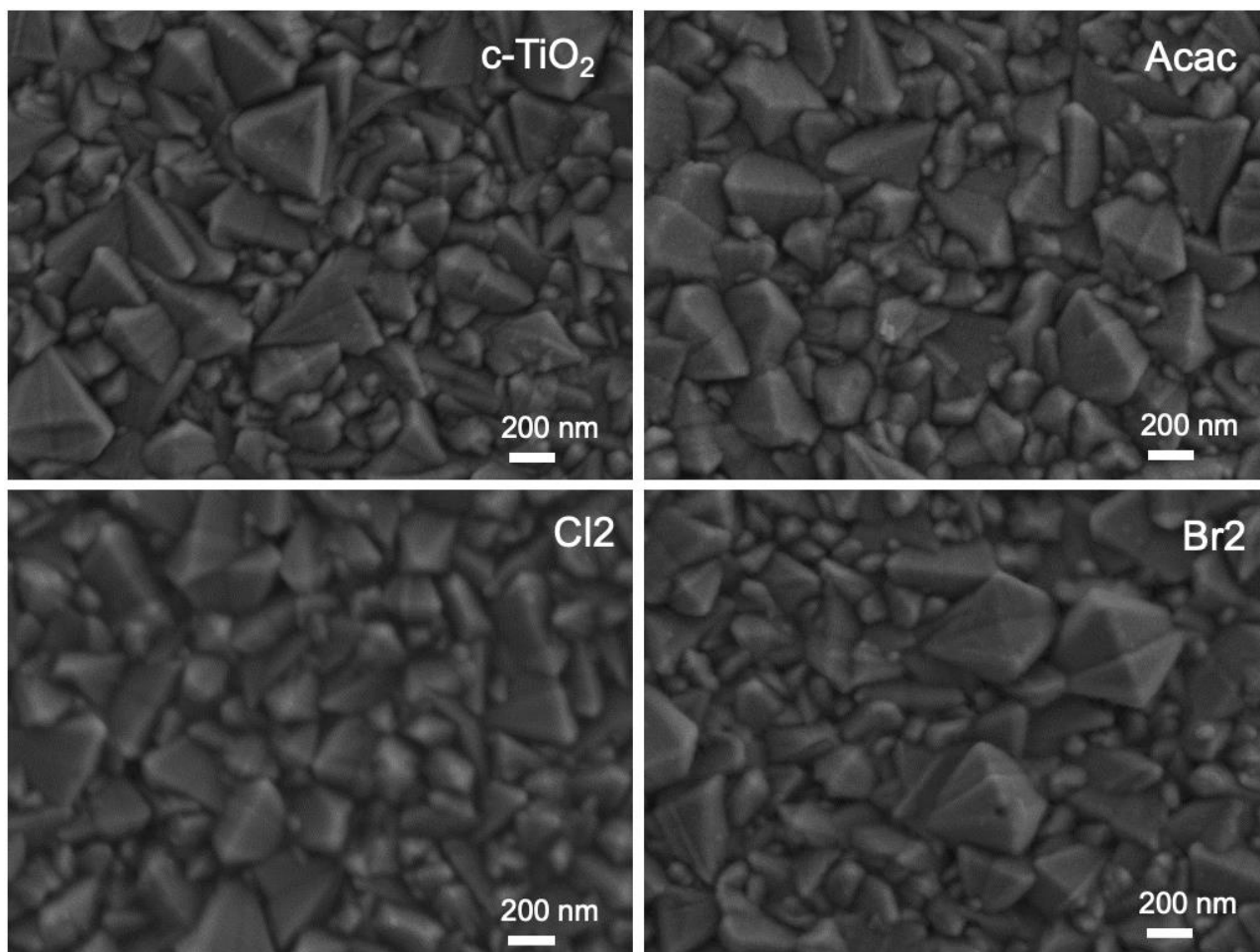
Fig S3.6 Top-view images SEM of c-TiO$_2$, Acac, Cl2 and Br2 on FTO, respectively. Films are annealed at 180 °C 1 h.
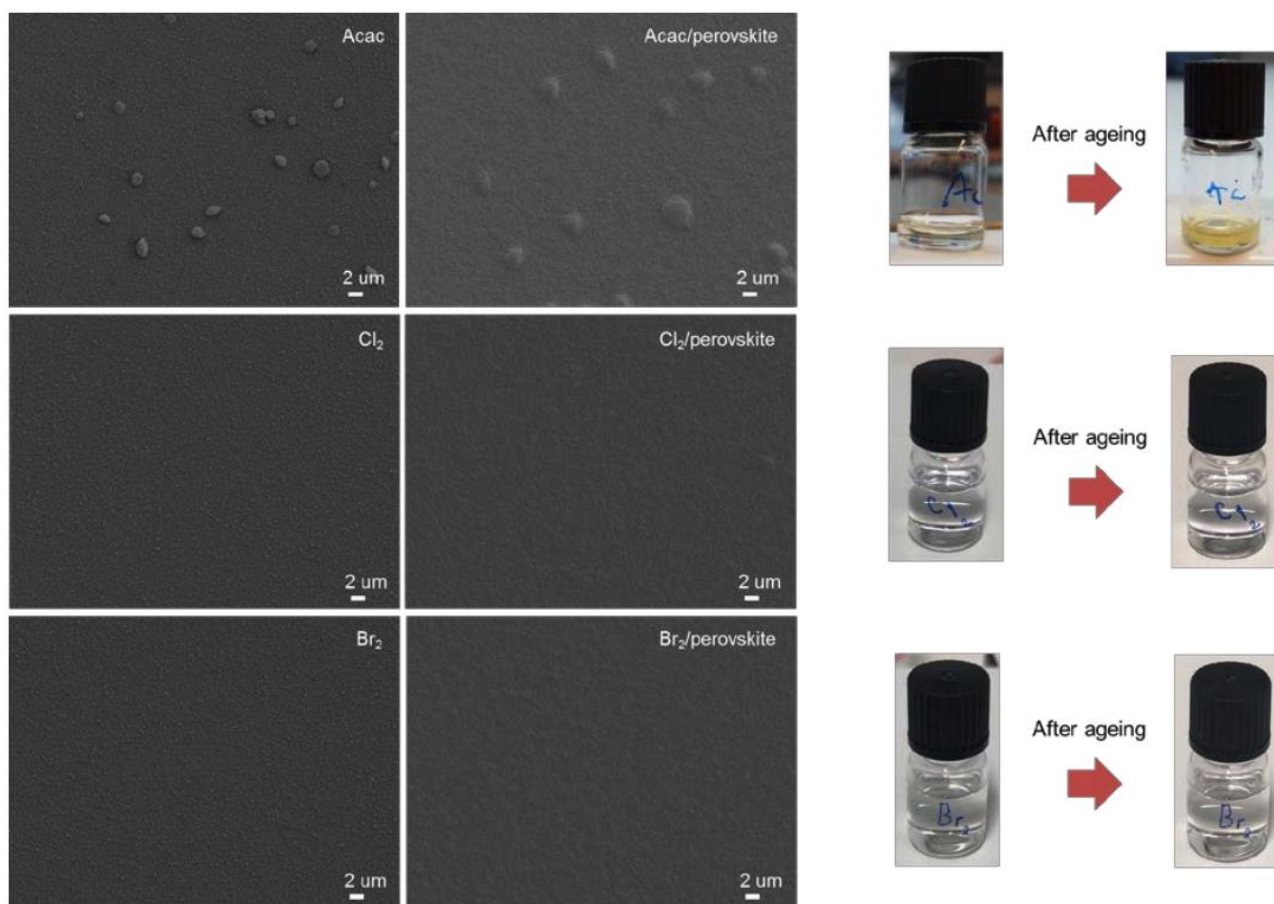
Fig S3.7 Top view SEM images of Acac, Cl2 and Br2 films on FTO/c-TiO$_2$ (left). An Acac solution in DMF turns into a turbid solution in a few hours while other solutions show no color or transparency change.
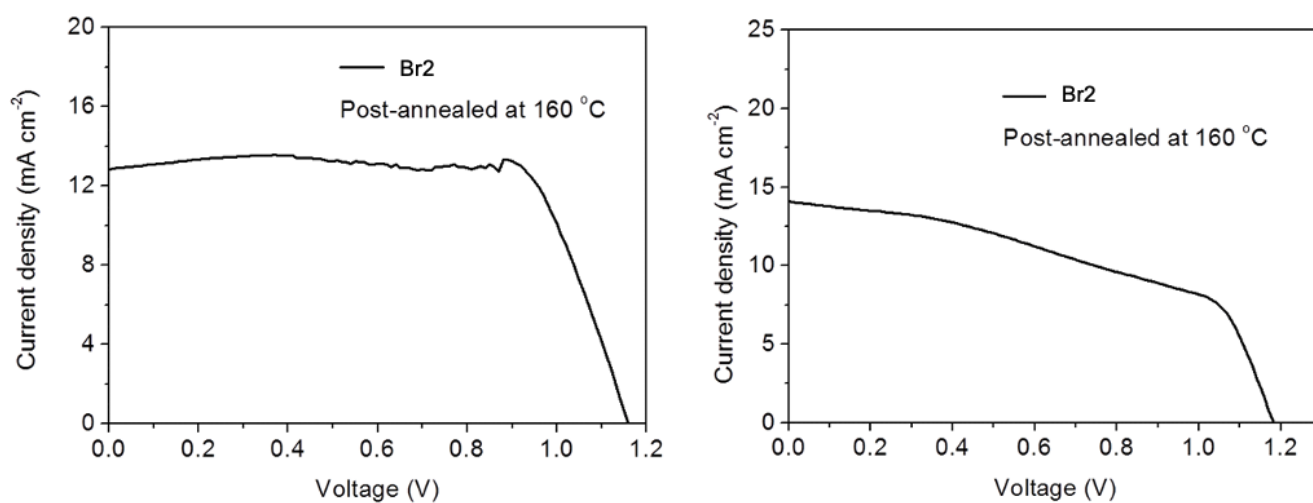
Fig S3.8 Typical *J-V* curves of perovskite solar cells with c-TiO$_2$/Br2 BETLs prepared at 160 °C.
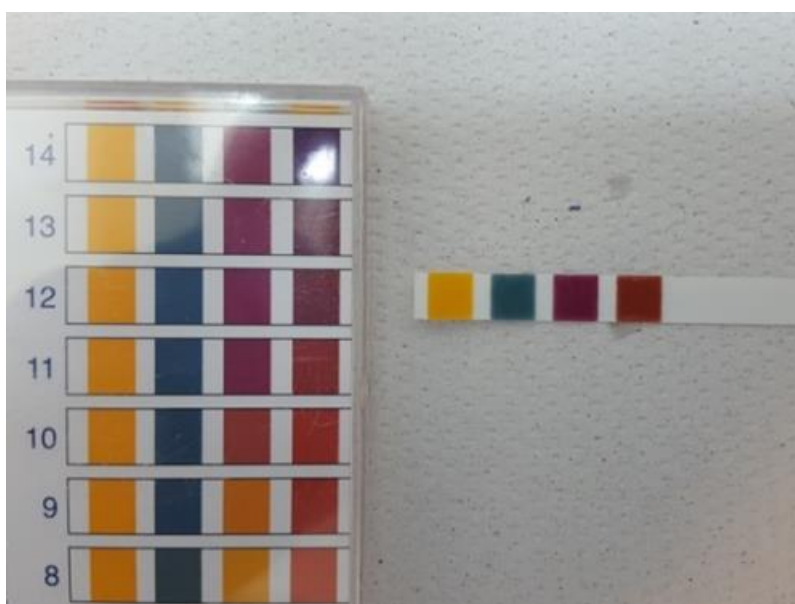
Fig S3.9 pH test of the colloidal SnO_2 15% in water (AlfaAesar). The result indicates the colloidal solution is in a highly basic condition with pH=11~12.
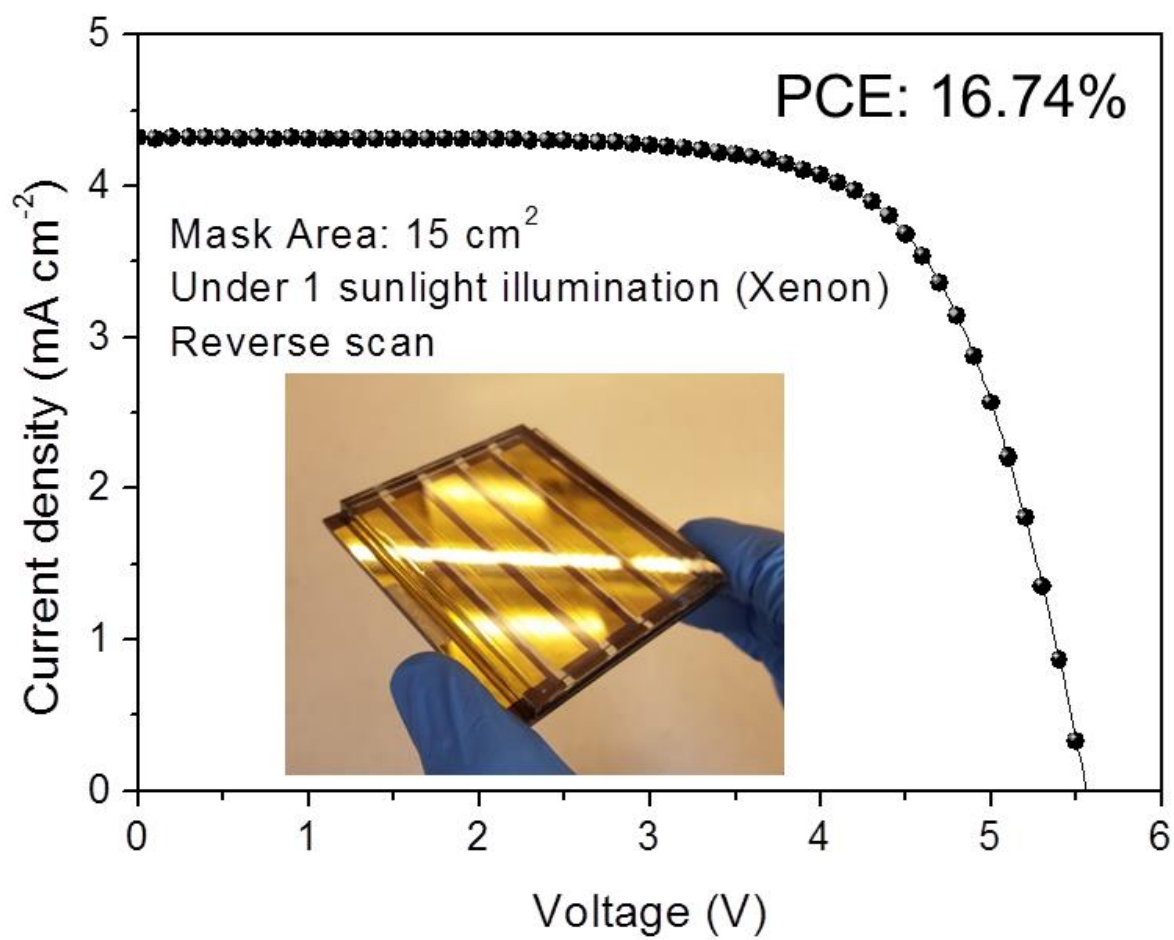
Fig S3.10 A J-V curve of the planar-type perovskite mini-module.
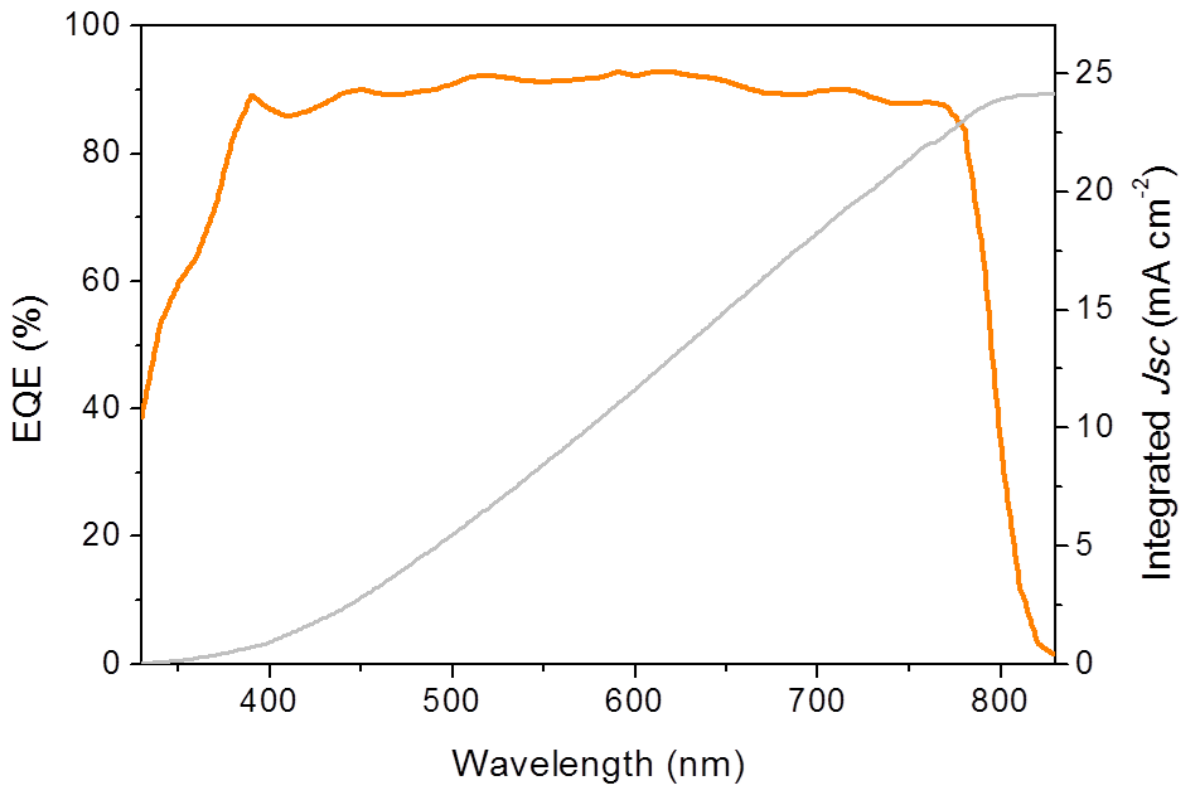
Fig S3.11 External quantum efficiency (EQE) of the champion cell.
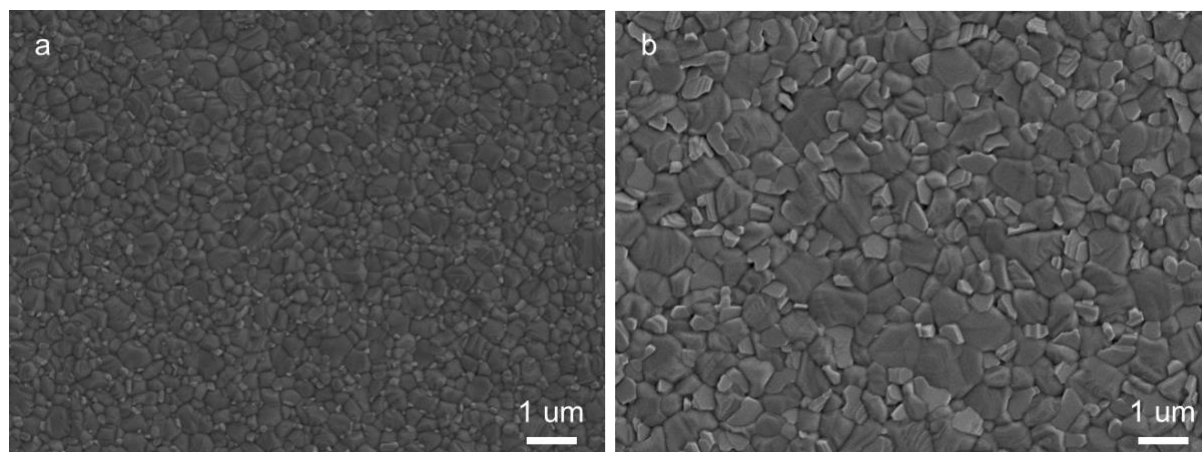
Fig S3.12 SEM top-view images of the perovskite films with one-step (a) and two-step method (b).
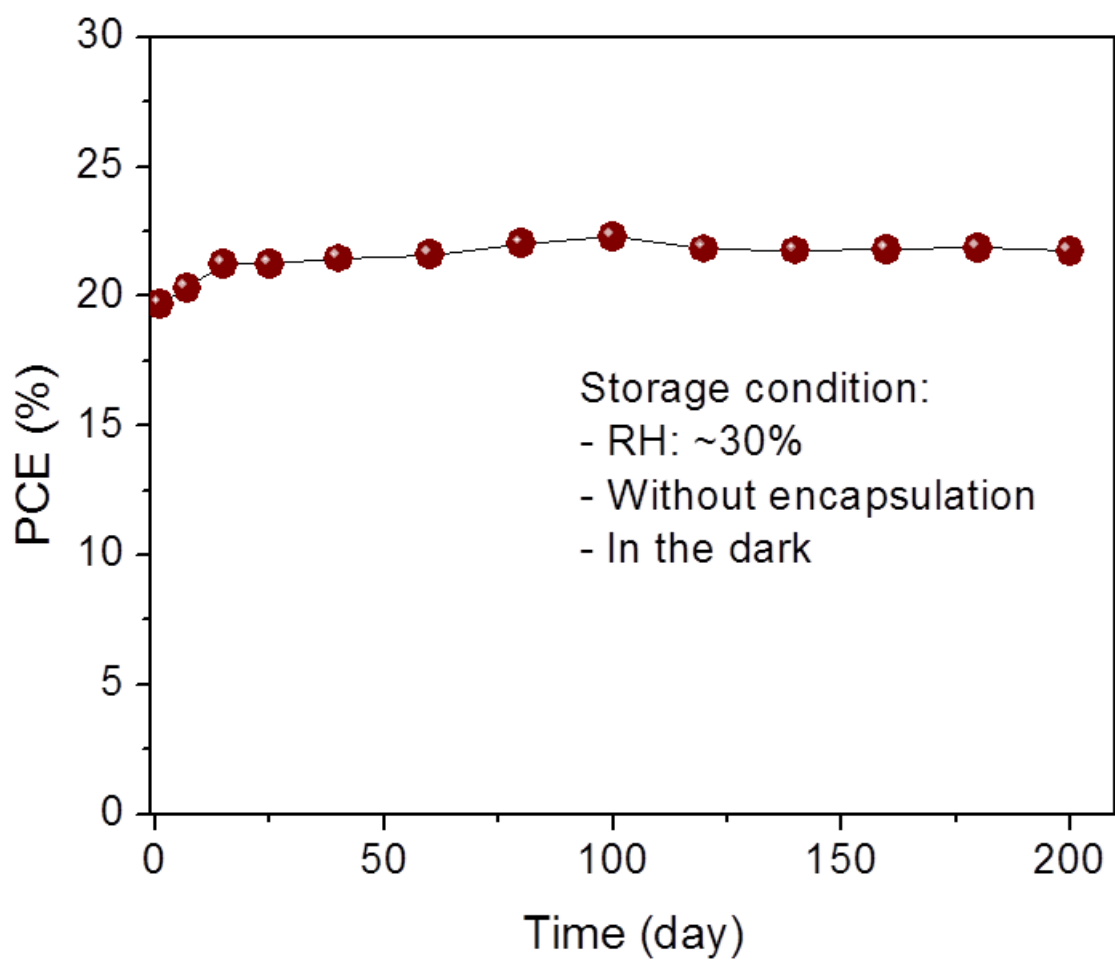
Fig S3.13 Long-term stability of the champion cell.
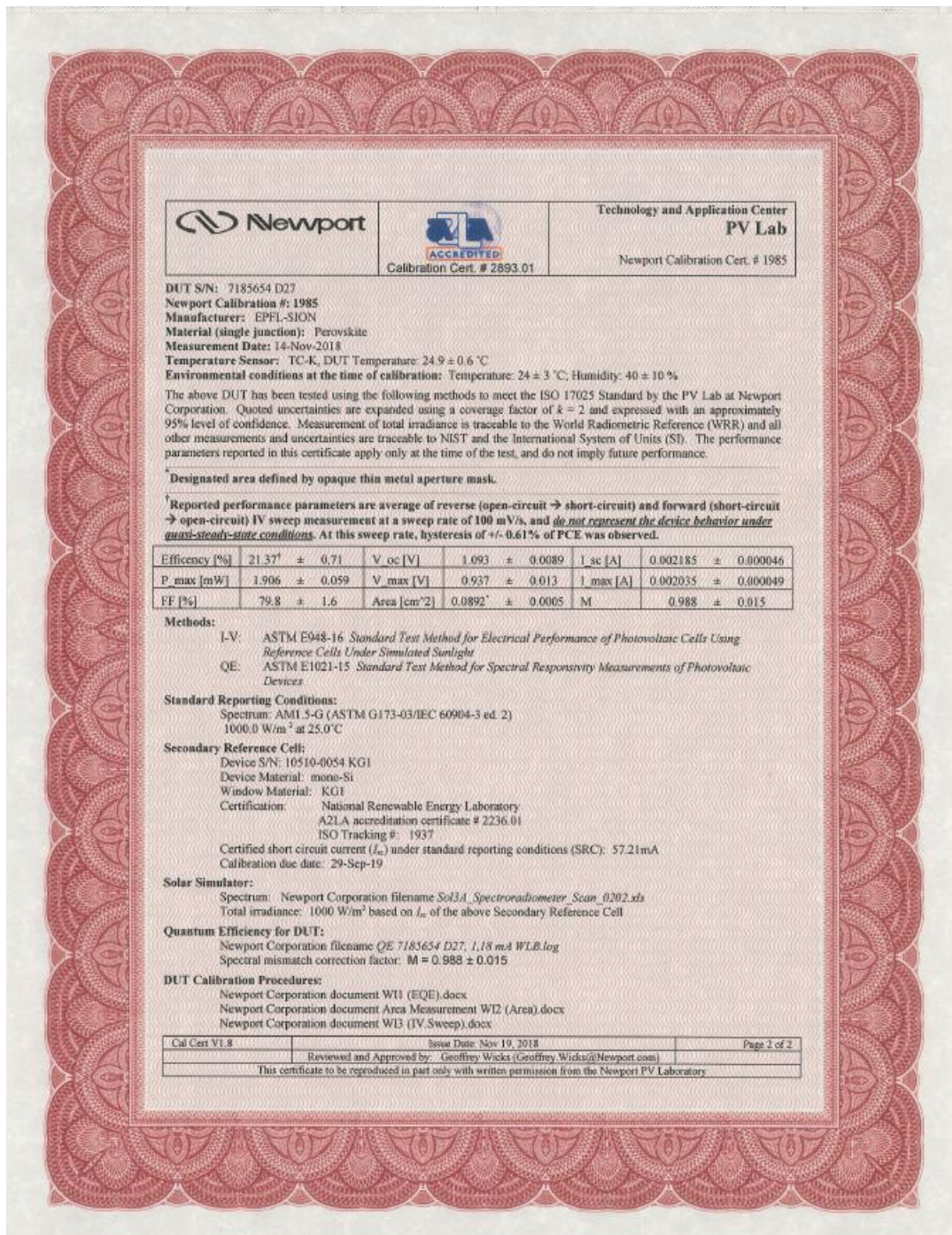
Fig S3.14 A certificate of the solar cell measured at the Newport.
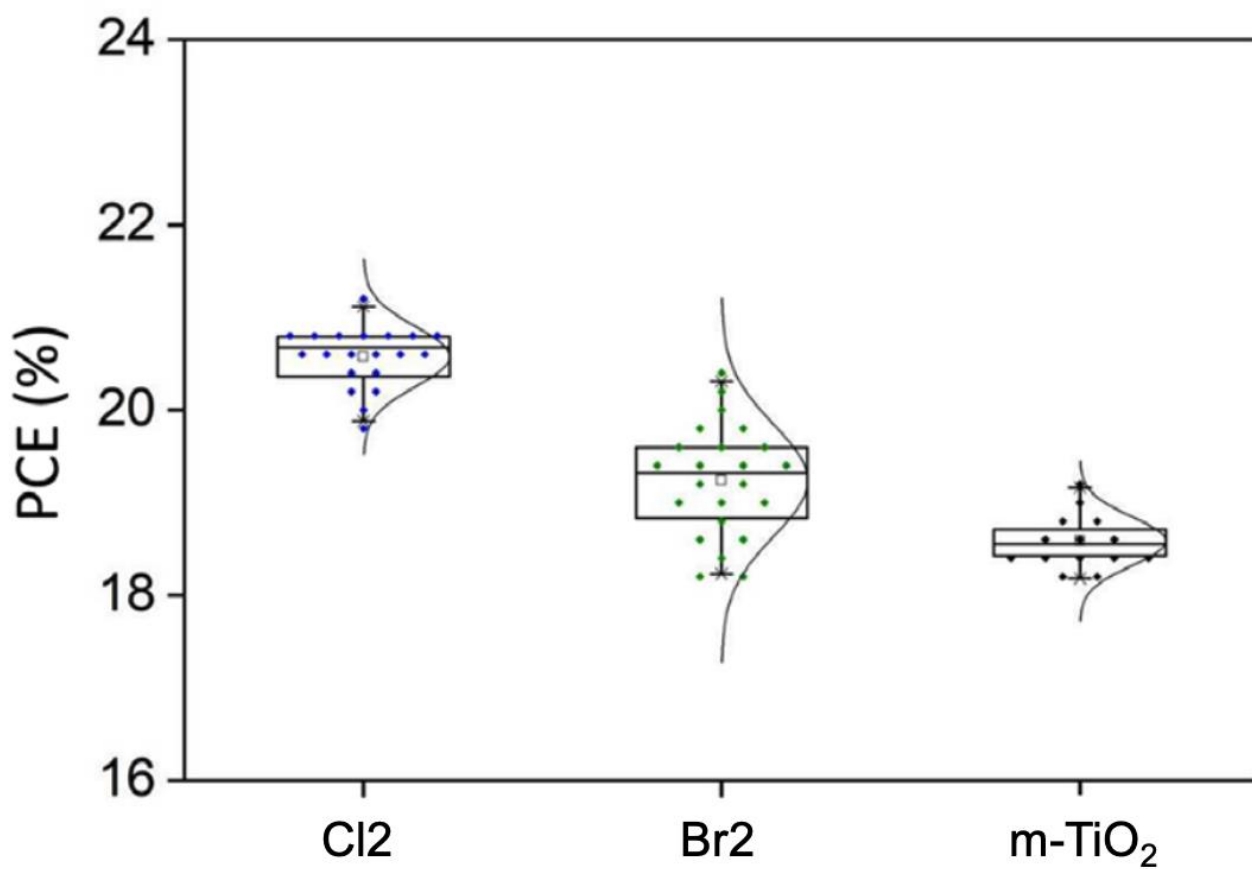
Fig S3.15 Box plot for perovskite devices employing Cl2, Br2 and m-TiO2 BETL configurations

6.3   Appendix to Chapter 4

6.3.1 Experimental

Sample preparation

Samples for characterization were prepared starting with a FTO substrate. The samples were sonicated in diluted detergent (1:4), water and isopropanol for 20, 10 and 5 min, respectively. Next, the samples were ozone treated for 15 min. A perovskite precursor composed of three cations $(FAPbI_3)_{0.85}(CsPbI_3)_{0.05}(MAPbI_2Cl)_{0.10}$ with excess PbI_2 was prepared by dissolving 1.436 M of lead iodide, 1.26 M of formamidinium iodide, 0.07 M of cesium iodide and 0.07 mg of methylammonium chloride in a 4:1 volumetric solution of DMSO:DMF. Spin-coating was performed through a two-step program running at 1000 and 3000 RPM for 12 and 30 s, respectively. 20 s into the second step a diethyl ether anti-solvent was dispensed. The samples were transferred to a 100 ℃ annealing plate after spin-coating and left for 1 h to allow optimal crystallization. The 2D perovskite solutions were spin-coated directly onto the 3D perovskite films at 3000 RPM for 15 s using three different isopropanol solutions (0.05 M n-octyl ammonium iodide for OAI, 0.05 M of propylammonium iodide for PAI and 0.05M of propylammonium iodide and n-octylammonium iodide mixture for OAI+PAI).

Device fabrication

Perovskite solar cell devices were fabricated to obtain performance parameters (JV and stability measurements.) Between each step, the samples were ozone-treated for 15 minutes. The fabrication was started by sonicating laser scribed FTO glass in diluted detergent (1:4), water, isopropanol, and acetone baths for 20, 10, 5 and 5 min, respectively. The compact TiO_2 layer was fabricated on top of the FTO by a spray pyrolysis procedure using a precursor solution (1.2 mL titanium diisopropoxide bis(acetylacetonate) in 20 mL of ethanol) at 450 ℃ annealing temperature. The mesoporous TiO_2 precursor solution was prepared by dissolving 0.381 g of TiO_2 paste in an 5 mL ethanol solution. Thereafter, the precursor was spin-coated at 2600 RPM and thermally processed through an annealing recipe (150, 250, 350, 450 and 500 ℃ for 5, 5, 5, 10 and 20 min respectively.) The SnO_2 layer was deposited by spin-coating the precursor (12 ☐l of $SnCl_4$ in 988 ☐L of H_2O) at 3000 RPM and annealed at 190 ℃ for 1 h. The HTL was deposited on the perovskite layer by spin-coating (3000 rpm for 30 s); the HTL (spiro-OMeTAD) precursor solution was prepared by dissolving 60 mg of spiro-OMeTAD in 768 µL chlorobenzene, 24 µL 4-tert-butyl pyridine, 14 µL of bis(trifluoromethane)sulfonimide lithium in acetonitrile solution (517 mg mL^{-1}) and 11 µL of tris(2(1Hpyrazol-1-yl)-4-tert-butyl pyridine)cobalt(III) tri[bis(trifluoromethane)sulfonimide] in

acetonitrile solution (376 mg mL^{-1}). Finally, 70 nm of the gold contact layer was deposited by a thermal evaporation method.

6.3.2 Characterization

The I–V measurements were carried out using an Oriel VeraSol solar simulator (Newport Corporation) and a LCE-50 (Centronics) calibrator, carried out from 1.2 to 0 V and from 0 to 1.2 V as reverse and forward scans, respectively, using a mask of 0.0804 mm^2. The scanning step and speed were 10 mV and 50 mV s^{-1}, respectively. UV/vis spectroscopy was measured using a Lambda 950S (PerkinElmer, Inc.). PL emission spectra were obtained with Fluorolog TCSPC (HORIBA, Ltd.) and an excitation wavelength of 475 nm. Time-resolved PL spectroscopy was conducted by Fluorolog TCSPC with an excitation wavelength of 640 nm (HORIBA, Ltd.). PL mapping was performed by inVia confocal Raman microscope (Renishaw plc.). SEM images were measured by field emission scanning electron microscopy (FEI, Teneo SEM). XPS and UPS measurements were recorded on a VersaProbe II (Physical Electronics Inc.) with a monochromator and Al Kα 1486.6 eV source. The spectrum was referenced using the C-C bound component of the adventitious carbon. The maximum power tracking and the stability test were carried out by keeping samples under the 1 sun (100 mW cm^{-2}) illumination with 100% nitrogen atmosphere and 0% humidity at 25 °C. X-ray diffraction (XRD) analysis was carried out using a D8 Advance diffractometer (Bruker Corporation) with Cu Kα radiation (λKα = 1.5418 Å).

6.3.3 Supplementary Information
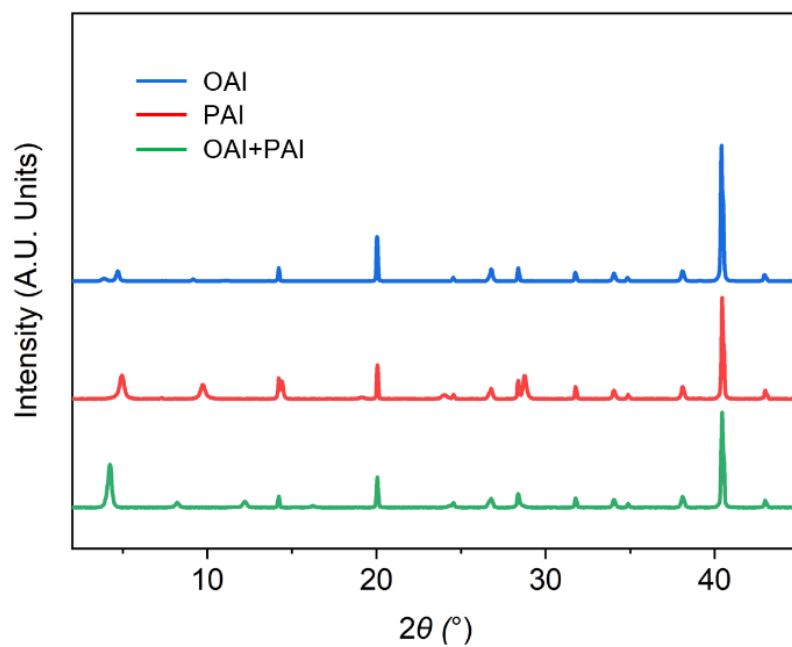
Fig S4.1 Full XRD spectra for OAI, PAI and OAI+PAI samples.
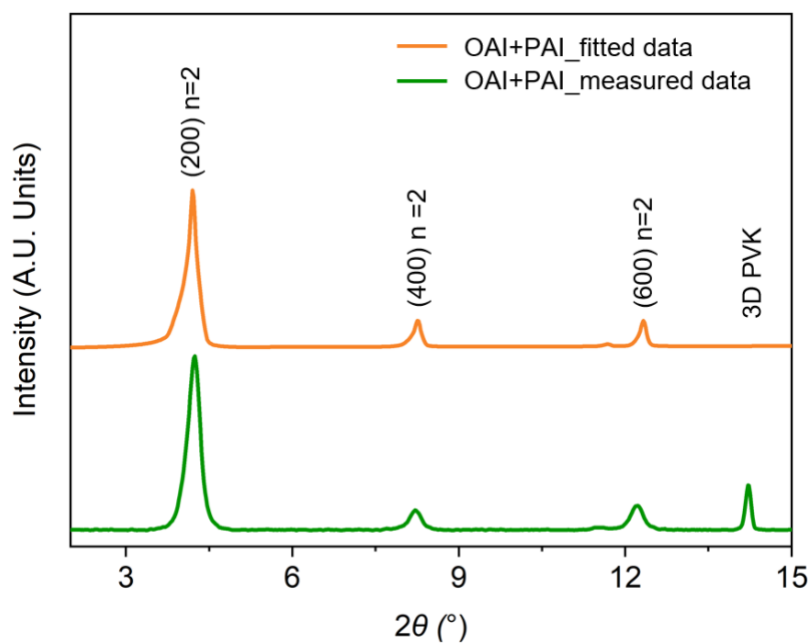
Fig S4.2Sample measured and fitted XRD spectra for OAI+PAI.

Table S4.1 Fitted crystal data for 2D Perovskite OAI+PAI

OAI+PAI
hkl Phase - 1 Lebail method
R-Bragg   99.961
Spacegroup   Pbca
Scale   1.60767e-007
Cell Mass   1.000
Cell Volume (Å^3)   3520.95291
Wt% - Rietveld   100.000
Double-Voigt|Approach
Cry size Lorentzian   194.9
k: 0.89 LVol-IB (nm)   110.417
k: 0.89 LVol-FWHM (nm)   73.443
Lattice parameters
    a (Å)   43.6386405
    b (Å)   9.0124875
    c (Å)   8.9525000

h	k	l	m	d	Th2	I
2	0	0	2	21.81932	4.04632	1.17e+005
4	0	0	2	10.90966	8.09770	5.32e+004
1	1	0	4	8.82622	10.01358	3.88e-042
3	1	0	4	7.66119	11.54116	6.23e+003
6	0	0	2	7.27311	12.15925	1.03e+005
1	1	1	4	6.28525	14.07933	8.65e-041
1	-1	-1	4	6.28525	14.07933	5.09e-042
5	1	0	4	6.26969	14.11445	1.89e-041
3	1	1	4	5.82079	15.20917	2.03e-041
3	-1	-1	4	5.82079	15.20917	7.85e-043
8	0	0	2	5.45483	16.23619	1.3e-041
5	-1	-1	4	5.13554	17.25312	1.49e-041
5	1	1	4	5.13554	17.25312	7.32e-041
7	1	0	4	5.12704	17.28194	1.88e-041
0	2	0	2	4.50624	19.68497	4.25e-042
0	0	2	2	4.47625	19.81820	6.83e-042
7	-1	-1	4	4.44909	19.94042	2.29e-042
7	1	1	4	4.44909	19.94042	1.31e-042
2	2	0	4	4.41311	20.10467	3.71e-042
2	0	-2	2	4.38493	20.23524	1.06e-042
2	0	2	2	4.38493	20.23524	1.66e-042
10	0	0	2	4.36386	20.33395	9.81e-044
9	1	0	4	4.26999	20.78588	2.82e-043

Table S4.2 Fitted crystal data for 2D perovskite OAI

OAI
hkl Phase - 1 Lebail method

R-Bragg	61.680
Spacegroup	Pbca
Scale	3.35345e-006
Cell Mass	1.000
Cell Volume (Å^3)	3492.44104
Wt% - Rietveld	100.000

Double-Voigt|Approach

Cry size Lorentzian	24.3
k: 1 LVol-IB (nm)	15.445
k: 0.89 LVol-FWHM (nm)	21.592

Lattice parameters

a (Å)	44.9283527
b (Å)	9.3781457
c (Å)	8.2887991

h	k	l	m	d	Th2	I
2	0	0	2	22.46418	3.93012	572
4	0	0	2	11.23209	7.86488	1.5e-010
1	1	0	4	9.18028	9.62645	3.88e-042
3	1	0	4	7.94834	11.12288	27
6	0	0	2	7.48806	11.80895	6.21e-022
5	1	0	4	6.48814	13.63693	1.89e-041
1	-1	-1	4	6.15216	14.38550	6.79e-018
1	1	1	4	6.15216	14.38550	1.18e-043
3	-1	-1	4	5.73691	15.43288	1.04e-029
3	1	1	4	5.73691	15.43288	4.53e-033
8	0	0	2	5.61604	15.76711	4.24e-030
7	1	0	4	5.29665	16.72450	1.49e-041
5	-1	-1	4	5.10907	17.34319	7.32e-041
5	1	1	4	5.10907	17.34319	1.88e-041
0	2	0	2	4.68907	18.91026	4.25e-042
2	2	0	4	4.59014	19.32169	6.83e-042
10	0	0	2	4.49284	19.74431	2.29e-042
7	1	1	4	4.46322	19.87667	2.29e-042
7	-1	-1	4	4.46322	19.87667	3.71e-042
9	1	0	4	4.40662	20.13459	1.06e-042
4	2	0	4	4.32714	20.50839	1.66e-042
0	0	2	2	4.14440	21.42311	9.81e-044

Table S4.3 Fitted crystal data for 2D perovskite PAI

PAI
hkl Phase - 1 Lebail method
R-Bragg	99.968
Spacegroup	Pbca
Scale	1.37335e-009
Cell Mass	1.000
Cell Volume (Å^3)	3179.97927
Wt% - Rietveld	100.000

Double-Voigt|Approach
Cry size Lorentzian	67.3
k: 1 LVol-IB (nm)	42.845
k: 0.89 LVol-FWHM (nm)	59.898

Lattice parameters
a (Å)	37.7212996
b (Å)	9.1905125
c (Å)	9.1727152

h	k	l	m	d	Th2	I
2	0	0	2	18.86065	4.68140	1.42e+007
4	0	0	2	9.43032	9.37063	3.16e+007
1	1	0	4	8.92930	9.89769	8.48e-042
3	1	0	4	7.41978	11.91801	1.48e-041
1	1	1	4	6.39829	13.82935	5.16e-035
1	-1	-1	4	6.39829	13.82935	5.99e-035
6	0	0	2	6.28688	14.07566	7.03e+007
5	1	0	4	5.83123	15.18177	5.81e-042
3	-1	-1	4	5.76875	15.34718	1.89e-041
3	1	1	4	5.76875	15.34718	7.77e-042
5	-1	-1	4	4.92103	18.01130	1.14e-041
5	1	1	4	4.92103	18.01130	1.56e-040
8	0	0	2	4.71516	18.80467	4.53e-043
7	1	0	4	4.64860	19.07642	1.66e-042
0	2	0	2	4.59526	19.29998	2.29e-042
0	0	2	2	4.58636	19.33779	1.07e-042
2	2	0	4	4.46465	19.87020	6.69e-041
2	0	-2	2	4.45649	19.90697	1.31e-042
2	0	2	2	4.45649	19.90697	1.34e-042
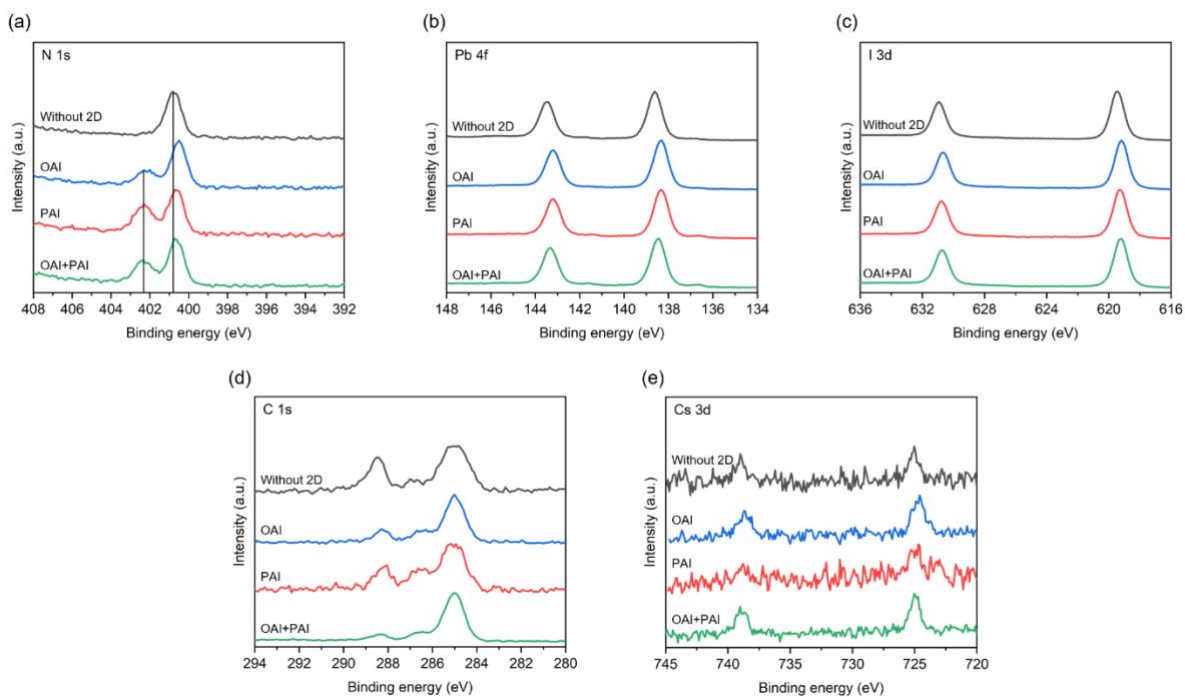
Fig S4.3 XPS spectra of (a) N 1s, (b) Pb 4f, (c) I 3d, (d) C 1s, and (e) Cs 3d for the 2D/3D samples. The 3D perovskite sample without 2D layer was used as a reference.
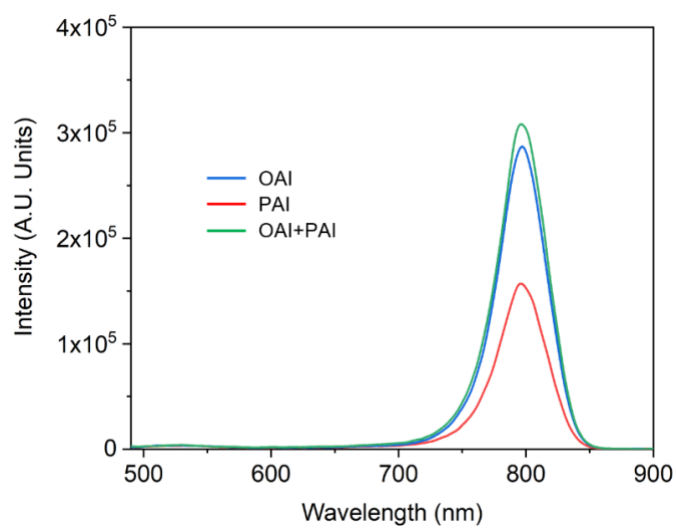
Fig S4.4 PL emission spectra for OAI, PAI, and OAI+PAI samples. The incident emission laser is from the glass side.
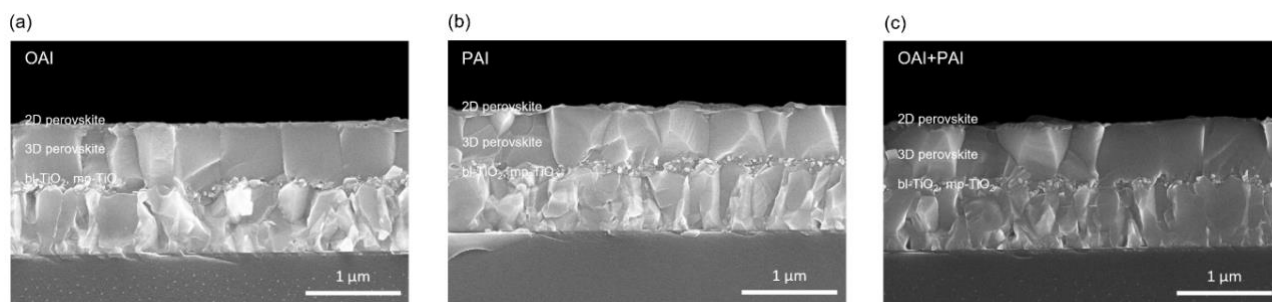
Fig S4.5 Cross-sectional scanning electron microscopy of the (a) OAI, (b) PAI and (c) OAI+PAI samples.

Table S4.4 TRPL parameters for the OAI, PAI and OAI+PAI.

	A_1	t_1	A_2	t_2
	[ns]	[ns]	[ns]	[ns]
OAI	0.273	167.9	0.630	939.6
PAI	0.461	128.1	0.497	574.8
OAI+PAI	0.240	160.6	0.632	979.5

† The equation for the fitting is $y = y0+A1\times exp(-(x-x0)/\tau a)+A2\times exp(-(x-x0)/\tau b)$.
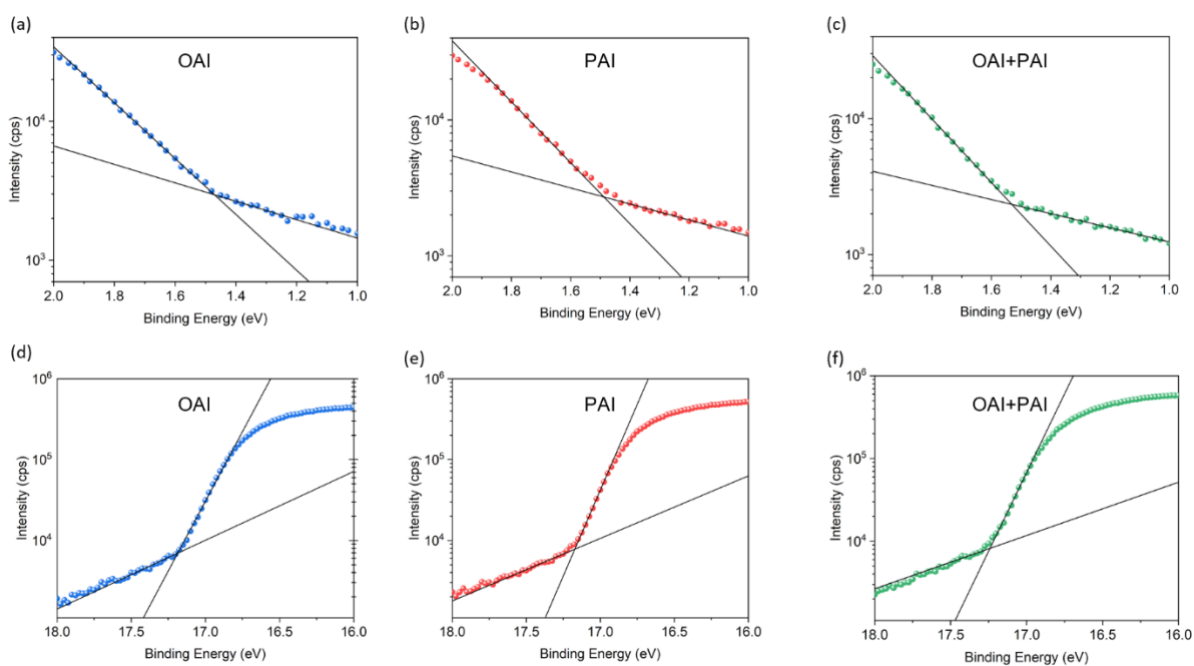
Fig S4.6 Measurement of the energy band diagram parameters. UPS spectrum edge of work function for (a) OAI, (b) PAI, and (c) OAI+PAI samples. (b) Valence band edge of perovskite layer for € PAI, (f) OAI, and (g) OAI+PAI samples.
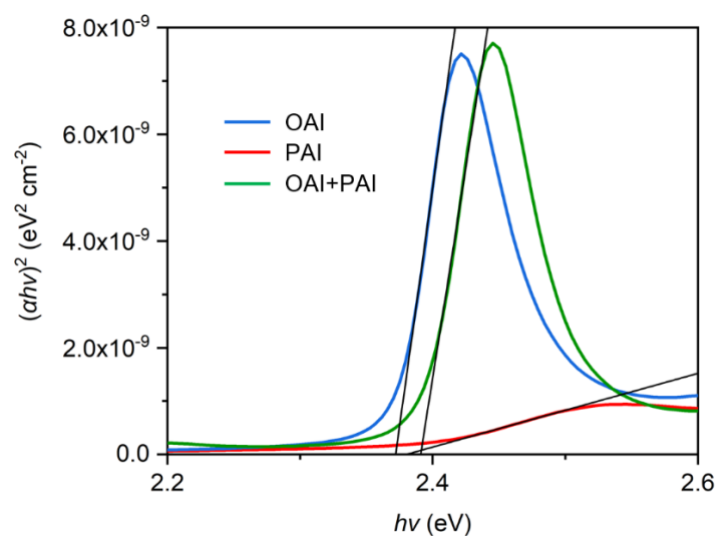
Fig S4.7 Tauc plot as obtained from UV-VIS to determine the bandgap of (a) OAI, (b) PAI, and (c) OAI+PAI samples.
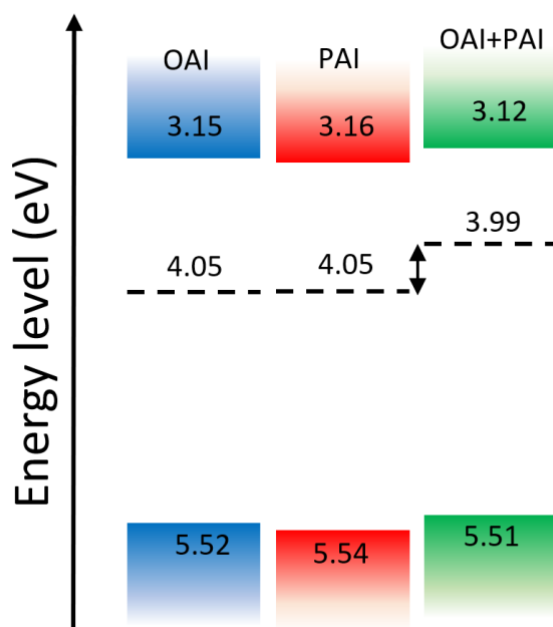
Fig S4.8 Energy band diagram for OAI, PAI and OAI+PAI samples.
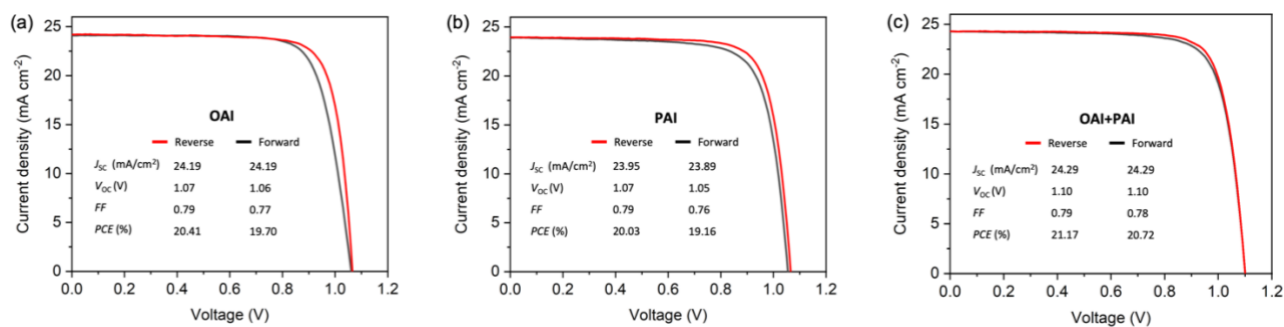
Fig S4.9 Hysteresis behavior for (a) OAI, (b) PAI and (c) OAI+PAI samples.
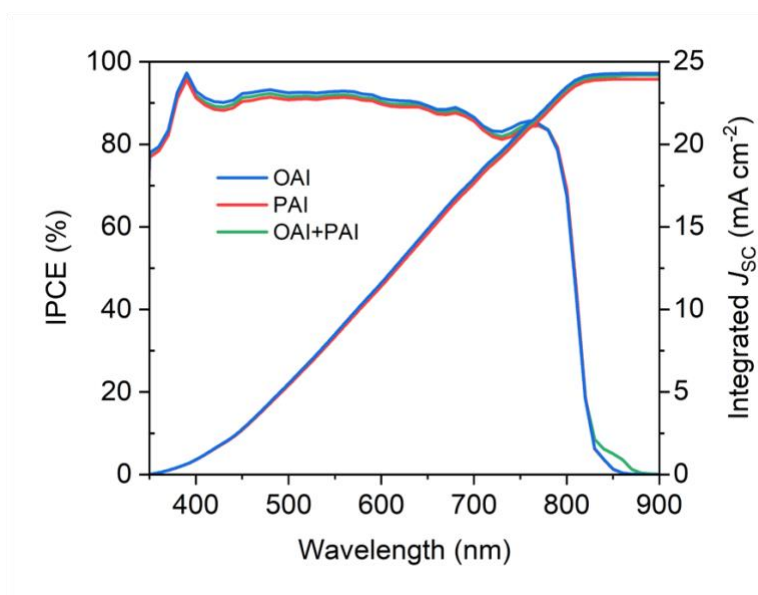
Fig S4.10 Incident photon to current efficiency (IPCE) OAI, PAI and OAI+PAI samples.

References

[1] T. Ahmad and D. Zhang, "A critical review of comparative global historical energy consumption and future demand: The story told so far," *Energy Reports*, vol. 6, pp. 1973–1991, Nov. 2020, doi: 10.1016/J.EGYR.2020.07.020.

[2] "Statistical Review of World Energy | Energy economics | Home." https://www.bp.com/en/global/corporate/energy-economics/statistical-review-of-world-energy.html (accessed Aug. 30, 2021).

[3] "Turning to renewables: Climate-safe energy solutions," */publications/2017/Nov/Turning-to-renewables-Climate-safe-energy-solutions*, Accessed: Sep. 01, 2021. [Online]. Available: /publications/2017/Nov/Turning-to-renewables-Climate-safe-energy-solutions.

[4] P. J. D. Janssen *et al.*, "Photosynthesis at the forefront of a sustainable life," *Front. Chem.*, vol. 2, pp. 1–22, Jun. 2014, doi: 10.3389/FCHEM.2014.00036.

[5] G. R. Timilsina, L. Kurdgelashvili, and P. A. Narbel, "Solar energy: Markets, economics and policies," *Renew. Sustain. Energy Rev.*, vol. 16, no. 1, pp. 449–465, Jan. 2012, doi: 10.1016/J.RSER.2011.08.009.

[6] M. Z. Jacobson and M. A. Delucchi, "Providing all global energy with wind, water, and solar power, Part I: Technologies, energy resources, quantities and areas of infrastructure, and materials," *Energy Policy*, vol. 39, no. 3, pp. 1154–1169, Mar. 2011, doi: 10.1016/J.ENPOL.2010.11.040.

[7] C. Battaglia, A. Cuevas, and S. De Wolf, "High-efficiency crystalline silicon solar cells: status and perspectives," *Energy Environ. Sci.*, vol. 9, no. 5, pp. 1552–1576, May 2016, doi: 10.1039/C5EE03380B.

[8] NREL, "Best Research-Cell Efficiencies: Rev. 04-06-2020," *Best Research-Cell Efficiency Chart | Photovoltaic Research | NREL*. 2020.

[9] H. Min *et al.*, "Perovskite solar cells with atomically coherent interlayers on SnO2 electrodes," *Nat. 2021 5987881*, vol. 598, no. 7881, pp. 444–450, Oct. 2021, doi: 10.1038/s41586-021-03964-8.

[10] G. Grancini *et al.*, "One-Year stable perovskite solar cells by 2D/3D interface engineering," *Nat. Commun. 2017 81*, vol. 8, no. 1, pp. 1–8, Jun. 2017, doi: 10.1038/ncomms15684.

[11]   S. Nair, S. B. Patel, and J. V. Gohel, "Recent trends in efficiency-stability improvement in perovskite solar cells," *Mater. Today Energy*, vol. 17, p. 100449, Sep. 2020, doi: 10.1016/J.MTENER.2020.100449.

[12]   B. J. Morgan and G. W. Watson, "Polaronic trapping of electrons and holes by native defects in anatase <span class," *Phys. Rev. B*, vol. 80, no. 23, p. 233102, Dec. 2009, doi: 10.1103/PhysRevB.80.233102.

[13]   H. J. Snaith and M. Grätzel, "Enhanced charge mobility in a molecular hole transporter via addition of redox inactive ionic dopant: Implication to dye-sensitized solar cells," *Appl. Phys. Lett.*, vol. 89, no. 26, p. 262114, Dec. 2006, doi: 10.1063/1.2424552.

[14]   J. Burschka, F. Kessler, M. K. Nazeeruddin, and M. Grätzel, "Co(III) Complexes as p-Dopants in Solid-State Dye-Sensitized Solar Cells," *Chem. Mater.*, vol. 25, no. 15, pp. 2986–2990, Aug. 2013, doi: 10.1021/CM400796U.

[15]   J. (John G. . Andrews and N. A. (Nicholas A. Jelley, "Energy science : principles, technologies, and impacts," pp. 184–197, 2013.

[16]   A. Kojima, K. Teshima, Y. Shirai, and T. Miyasaka, "Organometal Halide Perovskites as Visible-Light Sensitizers for Photovoltaic Cells," *J. Am. Chem. Soc.*, vol. 131, no. 17, pp. 6050–6051, May 2009, doi: 10.1021/JA809598R.

[17]   H.-S. Kim *et al.*, "Lead Iodide Perovskite Sensitized All-Solid-State Submicron Thin Film Mesoscopic Solar Cell with Efficiency Exceeding 9%," *Sci. Reports 2012 21*, vol. 2, no. 1, pp. 1–7, Aug. 2012, doi: 10.1038/srep00591.

[18]   P. Roy, N. Kumar Sinha, S. Tiwari, and A. Khare, "A review on perovskite solar cells: Evolution of architecture, fabrication techniques, commercialization issues and status," *Sol. Energy*, vol. 198, pp. 665–688, Mar. 2020, doi: 10.1016/J.SOLENER.2020.01.080.

[19]   M. Nakamura, K. Yamaguchi, Y. Kimoto, Y. Yasaki, T. Kato, and H. Sugimoto, "Cd-Free Cu(In,Ga)(Se,S)2 thin-film solar cell with record efficiency of 23.35%," *IEEE J. Photovoltaics*, vol. 9, no. 6, pp. 1863–1867, Nov. 2019, doi: 10.1109/JPHOTOV.2019.2937218.

[20]   D. B. Mitzi, C. A. Feild, W. T. A. Harrison, and A. M. Guloy, "Conducting tin halides with a layered organic-based perovskite structure," *Nat. 1994 3696480*, vol. 369, no. 6480, pp. 467–469, 1994, doi: 10.1038/369467a0.

[21]   G. Kieslich, S. Sun, and A. K. Cheetham, "Solid-state principles applied to organic–inorganic perovskites: new tricks for an old dog," *Chem. Sci.*, vol. 5, no. 12, pp. 4712–4715, Oct. 2014, doi: 10.1039/C4SC02211D.

[22]   Z. Li *et al.*, "Scalable fabrication of perovskite solar cells," *Nat. Rev. Mater. 2018 34*, vol. 3, no. 4, pp. 1–20, Mar. 2018, doi: 10.1038/natrevmats.2018.17.

[23]   Z. Li *et al.*, "Ink Engineering of Inkjet Printing Perovskite," *ACS Appl. Mater. Interfaces*, vol. 12, no. 35, pp. 39082–39091, Sep. 2020, doi: 10.1021/ACSAMI.0C09485.

[24]   Xuejie Zhu *et al.*, "Superior stability for perovskite solar cells with 20% efficiency using vacuum co-evaporation," *Nanoscale*, vol. 9, no. 34, pp. 12316–12323, Aug. 2017, doi: 10.1039/C7NR04501H.

[25]   J. You *et al.*, "Low-Temperature Solution-Processed Perovskite Solar Cells with High Efficiency and Flexibility," doi: 10.1021/nn406020d.

[26]   K. X. Steirer *et al.*, "Defect Tolerance in Methylammonium Lead Triiodide Perovskite," *ACS Energy Lett.*, vol. 1, no. 2, pp. 360–366, Aug. 2016, doi: 10.1021/ACSENERGYLETT.6B00196.

[27]   J. Kang and L.-W. Wang, "High Defect Tolerance in Lead Halide Perovskite CsPbBr3," *J. Phys. Chem. Lett.*, vol. 8, no. 2, pp. 489–493, Jan. 2017, doi: 10.1021/ACS.JPCLETT.6B02800.

[28]   S. D. Stranks *et al.*, "Electron-Hole Diffusion Lengths Exceeding 1 Micrometer in an Organometal Trihalide Perovskite Absorber," *Science (80-.).*, vol. 342, no. 6156, pp. 341–344, Oct. 2013, doi: 10.1126/SCIENCE.1243982.

[29]   W. Ning *et al.*, "Long Electron–Hole Diffusion Length in High-Quality Lead-Free Double Perovskite Films," *Adv. Mater.*, vol. 30, no. 20, p. 1706246, May 2018, doi: 10.1002/ADMA.201706246.

[30]   Michael Saliba *et al.*, "Cesium-containing triple cation perovskite solar cells: improved stability, reproducibility and high efficiency," *Energy Environ. Sci.*, vol. 9, no. 6, pp. 1989–1997, Jun. 2016, doi: 10.1039/C5EE03874J.

[31]   X. Liu, J. Yi, and Z. Ku, "Novel quadruple-cation absorber for universal hysteresis elimination for high efficiency and stable perovskite solar cells," 2017, doi: 10.1039/C7EE02634J.

[32] K. A. Bush *et al.*, "Compositional Engineering for Efficient Wide Band Gap Perovskites with Improved Stability to Photoinduced Phase Segregation," *ACS Energy Lett.*, vol. 3, no. 2, pp. 428–435, Feb. 2018, doi: 10.1021/ACSENERGYLETT.7B01255.

[33] H. Lu, A. Krishna, S. M. Zakeeruddin, M. Grätzel, and A. Hagfeldt, "Compositional and Interface Engineering of Organic-Inorganic Lead Halide Perovskite Solar Cells," *iScience*, vol. 23, no. 8, p. 101359, Aug. 2020, doi: 10.1016/J.ISCI.2020.101359.

[34] E. A. Alharbi *et al.*, "Formation of High-Performance Multi-Cation Halide Perovskites Photovoltaics by δ-CsPbI3/δ-RbPbI3 Seed-Assisted Heterogeneous Nucleation," *Adv. Energy Mater.*, vol. 11, no. 16, p. 2003785, Apr. 2021, doi: 10.1002/AENM.202003785.

[35] F. O. Saouma, D. Y. Park, S. H. Kim, M. S. Jeong, and J. I. Jang, "Multiphoton Absorption Coefficients of Organic–Inorganic Lead Halide Perovskites CH3NH3PbX3 (X = Cl, Br, I) Single Crystals," *Chem. Mater.*, vol. 29, no. 16, pp. 6876–6882, Aug. 2017, doi: 10.1021/ACS.CHEMMATER.7B02110.

[36] R. X. Yang, J. M. Skelton, E. L. da Silva, J. M. Frost, and A. Walsh, "Spontaneous Octahedral Tilting in the Cubic Inorganic Cesium Halide Perovskites CsSnX3 and CsPbX3 (X = F, Cl, Br, I)," *J. Phys. Chem. Lett.*, vol. 8, no. 19, pp. 4720–4726, Oct. 2017, doi: 10.1021/ACS.JPCLETT.7B02423.

[37] L. Protesescu *et al.*, "Nanocrystals of Cesium Lead Halide Perovskites (CsPbX3, X = Cl, Br, and I): Novel Optoelectronic Materials Showing Bright Emission with Wide Color Gamut," *Nano Lett.*, vol. 15, no. 6, pp. 3692–3696, Jun. 2015, doi: 10.1021/NL5048779.

[38] L. K. Ono, E. J. Juarez-Perez, and Y. Qi, "Progress on Perovskite Materials and Solar Cells with Mixed Cations and Halide Anions," *ACS Appl. Mater. Interfaces*, vol. 9, no. 36, pp. 30197–30246, Sep. 2017, doi: 10.1021/ACSAMI.7B06001.

[39] R. Prasanna *et al.*, "Band Gap Tuning via Lattice Contraction and Octahedral Tilting in Perovskite Materials for Photovoltaics," *J. Am. Chem. Soc.*, vol. 139, no. 32, pp. 11117–11124, Aug. 2017, doi: 10.1021/JACS.7B04981.

[40] M. R. Filip, G. E. Eperon, H. J. Snaith, and F. Giustino, "Steric engineering of metal-halide perovskites with tunable optical band gaps," *Nat. Commun. 2014 51*, vol. 5, no. 1, pp. 1–9, Dec. 2014, doi: 10.1038/ncomms6757.

[41] K. Momma and F. Izumi, "VESTA 3 for three-dimensional visualization of crystal, volumetric and morphology data," *urn:issn:0021-8898*, vol. 44, no. 6, pp. 1272–1276, Oct. 2011, doi:

10.1107/S0021889811038970.

[42] D. Luo, R. Su, W. Zhang, Q. Gong, and R. Zhu, "Minimizing non-radiative recombination losses in perovskite solar cells," *Nat. Rev. Mater. 2019 51*, vol. 5, no. 1, pp. 44–60, Nov. 2019, doi: 10.1038/s41578-019-0151-y.

[43] C. Wehrenfennig, G. E. Eperon, M. B. Johnston, H. J. Snaith, and L. M. Herz, "High Charge Carrier Mobilities and Lifetimes in Organolead Trihalide Perovskites," *Adv. Mater.*, vol. 26, no. 10, pp. 1584–1589, Mar. 2014, doi: 10.1002/ADMA.201305172.

[44] J. B. Patel, R. L. Milot, A. D. Wright, L. M. Herz, and M. B. Johnston, "Formation Dynamics of CH3NH3PbI3 Perovskite Following Two-Step Layer Deposition," *J. Phys. Chem. Lett.*, vol. 7, no. 1, pp. 96–102, Jan. 2015, doi: 10.1021/ACS.JPCLETT.5B02495.

[45] J. M. Ball and A. Petrozza, "Defects in perovskite-halides and their effects in solar cells," *Nat. Energy 2016 111*, vol. 1, no. 11, pp. 1–13, Oct. 2016, doi: 10.1038/nenergy.2016.149.

[46] J. Huang, Y. Yuan, Y. Shao, and Y. Yan, "Understanding the physical properties of hybrid perovskites for photovoltaic applications," *Nat. Rev. Mater. 2017 27*, vol. 2, no. 7, pp. 1–19, Jul. 2017, doi: 10.1038/natrevmats.2017.42.

[47] L. M. Herz, "Charge-Carrier Dynamics in Organic-Inorganic Metal Halide Perovskites," 2016, doi: 10.1146/annurev-physchem-040215-112222.

[48] C. Ran, J. Xu, W. Gao, C. Huang, and S. Dou, "Defects in metal triiodide perovskite materials towards high-performance solar cells: origin, impact, characterization, and engineering," *Chem. Soc. Rev.*, vol. 47, no. 12, pp. 4581–4610, Jun. 2018, doi: 10.1039/C7CS00868F.

[49] F. Wang, S. Bai, W. Tress, A. Hagfeldt, and F. Gao, "Defects engineering for high-performance perovskite solar cells," *npj Flex. Electron. 2018 21*, vol. 2, no. 1, pp. 1–14, Aug. 2018, doi: 10.1038/s41528-018-0035-z.

[50] D. W. de Quilettes *et al.*, "Impact of microstructure on local carrier lifetime in perovskite solar cells," *Science (80-.).*, vol. 348, no. 6235, pp. 683–686, May 2015, doi: 10.1126/SCIENCE.AAA5333.

[51] P. Jia *et al.*, "The Trapped Charges at Grain Boundaries in Perovskite Solar Cells," *Adv. Funct. Mater.*, p. 2107125, 2021, doi: 10.1002/ADFM.202107125.

[52] K. Yao *et al.*, "Plasmon-induced trap filling at grain boundaries in perovskite solar cells," *Light*

Sci. Appl. 2021 101, vol. 10, no. 1, pp. 1–12, Oct. 2021, doi: 10.1038/s41377-021-00662-y.

[53] J.-S. Park, J. Calbo, Y.-K. Jung, L. D. Whalley, and A. Walsh, "Accumulation of Deep Traps at Grain Boundaries in Halide Perovskites," *ACS Energy Lett.*, vol. 4, no. 6, pp. 1321–1327, Jun. 2019, doi: 10.1021/ACSENERGYLETT.9B00840.

[54] M. Liu, M. B. Johnston, and H. J. Snaith, "Efficient planar heterojunction perovskite solar cells by vapour deposition," *Nat. 2013 5017467*, vol. 501, no. 7467, pp. 395–398, Sep. 2013, doi: 10.1038/nature12509.

[55] N. J. Jeon, J. H. Noh, Y. C. Kim, W. S. Yang, S. Ryu, and S. Il Seok, "Solvent engineering for high-performance inorganic–organic hybrid perovskite solar cells," *Nat. Mater. 2014 139*, vol. 13, no. 9, pp. 897–903, Jul. 2014, doi: 10.1038/nmat4014.

[56] J.-H. Im, I.-H. Jang, N. Pellet, M. Grätzel, and N.-G. Park, "Growth of CH3NH3PbI3 cuboids with controlled size for high-efficiency perovskite solar cells," *Nat. Nanotechnol. 2014 911*, vol. 9, no. 11, pp. 927–932, Aug. 2014, doi: 10.1038/nnano.2014.181.

[57] Q. Chen *et al.*, "Controllable Self-Induced Passivation of Hybrid Lead Iodide Perovskites toward High Performance Solar Cells," *Nano Lett.*, vol. 14, no. 7, pp. 4158–4163, Jul. 2014, doi: 10.1021/NL501838Y.

[58] F. Liu *et al.*, "Is Excess PbI2 Beneficial for Perovskite Solar Cell Performance?," *Adv. Energy Mater.*, vol. 6, no. 7, p. 1502206, Apr. 2016, doi: 10.1002/AENM.201502206.

[59] T. J. Jacobsson *et al.*, "Unreacted PbI2 as a Double-Edged Sword for Enhancing the Performance of Perovskite Solar Cells," *J. Am. Chem. Soc.*, vol. 138, no. 32, pp. 10331–10343, Aug. 2016, doi: 10.1021/JACS.6B06320.

[60] S.-H. Turren-Cruz, A. Hagfeldt, and M. Saliba, "Methylammonium-free, high-performance, and stable perovskite solar cells on a planar architecture," *Science (80-.).*, vol. 362, no. 6413, pp. 449–453, Oct. 2018, doi: 10.1126/SCIENCE.AAT3583.

[61] B. Roose, K. Dey, Y.-H. Chiang, R. H. Friend, and S. D. Stranks, "Critical Assessment of the Use of Excess Lead Iodide in Lead Halide Perovskite Solar Cells," *J. Phys. Chem. Lett.*, vol. 11, no. 16, pp. 6505–6512, Aug. 2020, doi: 10.1021/ACS.JPCLETT.0C01820.

[62] C. Roldán-Carmona *et al.*, "High efficiency methylammonium lead triiodide perovskite solar cells: the relevance of non-stoichiometric precursors," *Energy Environ. Sci.*, vol. 8, no. 12, pp. 3550–3556, Nov. 2015, doi: 10.1039/C5EE02555A.

[63] N. K. Noel *et al.*, "Enhanced Photoluminescence and Solar Cell Performance via Lewis Base Passivation of Organic–Inorganic Lead Halide Perovskites," *ACS Nano*, vol. 8, no. 10, pp. 9815–9821, Oct. 2014, doi: 10.1021/NN5036476.

[64] G. Yang, P. Qin, G. Fang, and G. Li, "A Lewis Base-Assisted Passivation Strategy Towards Highly Efficient and Stable Perovskite Solar Cells," *Sol. RRL*, vol. 2, no. 8, p. 1800055, Aug. 2018, doi: 10.1002/SOLR.201800055.

[65] R. J. E. Westbrook *et al.*, "Lewis Base Passivation Mediates Charge Transfer at Perovskite Heterojunctions," *J. Am. Chem. Soc.*, vol. 143, no. 31, pp. 12230–12243, Aug. 2021, doi: 10.1021/JACS.1C05122.

[66] P. Caprioglio *et al.*, "Bi-functional interfaces by poly(ionic liquid) treatment in efficient pin and nip perovskite solar cells," *Energy Environ. Sci.*, vol. 14, no. 8, pp. 4508–4522, Aug. 2021, doi: 10.1039/D1EE00869B.

[67] M. Li *et al.*, "Interface Modification by Ionic Liquid: A Promising Candidate for Indoor Light Harvesting and Stability Improvement of Planar Perovskite Solar Cells," *Adv. Energy Mater.*, vol. 8, no. 24, p. 1801509, Aug. 2018, doi: 10.1002/AENM.201801509.

[68] W. Zhang *et al.*, "Interface Engineering of Imidazolium Ionic Liquids toward Efficient and Stable CsPbBr3 Perovskite Solar Cells," *ACS Appl. Mater. Interfaces*, vol. 12, no. 4, pp. 4540–4548, Jan. 2020, doi: 10.1021/ACSAMI.9B20831.

[69] H. Kanda *et al.*, "Light Stability Enhancement of Perovskite Solar Cells Using 1H,1H,2H,2H-Perfluorooctyltriethoxysilane Passivation," *Sol. RRL*, vol. 5, no. 3, p. 2000650, Mar. 2021, doi: 10.1002/SOLR.202000650.

[70] B. Chaudhary *et al.*, "Poly(4-Vinylpyridine)-Based Interfacial Passivation to Enhance Voltage and Moisture Stability of Lead Halide Perovskite Solar Cells," *ChemSusChem*, vol. 10, no. 11, pp. 2473–2479, Jun. 2017, doi: 10.1002/CSSC.201700271.

[71] N. K. Noel *et al.*, "Interfacial charge-transfer doping of metal halide perovskites for high performance photovoltaics," *Energy Environ. Sci.*, vol. 12, no. 10, pp. 3063–3073, Oct. 2019, doi: 10.1039/C9EE01773A.

[72] W. Nie *et al.*, "Critical Role of Interface and Crystallinity on the Performance and Photostability of Perovskite Solar Cell on Nickel Oxide," *Adv. Mater.*, vol. 30, no. 5, p. 1703879, Feb. 2018, doi: 10.1002/ADMA.201703879.

[73] P. Tiwana, P. Docampo, M. B. Johnston, H. J. Snaith, and L. M. Herz, "Electron Mobility and Injection Dynamics in Mesoporous ZnO, SnO2, and TiO2 Films Used in Dye-Sensitized Solar Cells," *ACS Nano*, vol. 5, no. 6, pp. 5158–5166, Jun. 2011, doi: 10.1021/NN201243Y.

[74] D. O. Scanlon *et al.*, "Band alignment of rutile and anatase TiO2," *Nat. Mater. 2013 129*, vol. 12, no. 9, pp. 798–801, Jul. 2013, doi: 10.1038/nmat3697.

[75] M. F. M. Noh *et al.*, "The architecture of the electron transport layer for a perovskite solar cell," *J. Mater. Chem. C*, vol. 6, no. 4, pp. 682–712, Jan. 2018, doi: 10.1039/C7TC04649A.

[76] M. A. Green, A. Ho-Baillie, and H. J. Snaith, "The emergence of perovskite solar cells," *Nat. Photonics 2014 87*, vol. 8, no. 7, pp. 506–514, Jun. 2014, doi: 10.1038/nphoton.2014.134.

[77] M. Liu, M. Endo, A. Shimazaki, A. Wakamiya, and Y. Tachibana, "Identifying an Optimum Perovskite Solar Cell Structure by Kinetic Analysis: Planar, Mesoporous Based, or Extremely Thin Absorber Structure," *ACS Appl. Energy Mater.*, vol. 1, no. 8, pp. 3722–3732, Aug. 2018, doi: 10.1021/ACSAEM.8B00515.

[78] S.-W. Lee *et al.*, "UV Degradation and Recovery of Perovskite Solar Cells," *Sci. Reports 2016 61*, vol. 6, no. 1, pp. 1–10, Dec. 2016, doi: 10.1038/srep38150.

[79] Guangda Niu, Wenzhe Li, Fanqi Meng, Liduo Wang, Haopeng Dong, and Yong Qiu, "Study on the stability of CH 3 NH 3 PbI 3 films and the effect of post-modification by aluminum oxide in all-solid-state hybrid solar cells," *J. Mater. Chem. A*, vol. 2, no. 3, pp. 705–710, Dec. 2013, doi: 10.1039/C3TA13606J.

[80] J. Nowotny *et al.*, "Defect chemistry and defect engineering of TiO2-based semiconductors for solar energy conversion," *Chem. Soc. Rev.*, vol. 44, no. 23, pp. 8424–8442, Nov. 2015, doi: 10.1039/C4CS00469H.

[81] Q. Jiang *et al.*, "Enhanced electron extraction using SnO2 for high-efficiency planar-structure HC(NH2)2PbI3-based perovskite solar cells," *Nat. Energy 2016 21*, vol. 2, no. 1, pp. 1–7, Nov. 2016, doi: 10.1038/nenergy.2016.177.

[82] T. Leijtens, G. E. Eperon, S. Pathak, A. Abate, M. M. Lee, and H. J. Snaith, "Overcoming ultraviolet light instability of sensitized TiO2 with meso-superstructured organometal tri-halide perovskite solar cells," *Nat. Commun.*, 2013, doi: 10.1038/ncomms3885.

[83] X. Xu *et al.*, "Highly efficient planar perovskite solar cells with a TiO2/ZnO electron transport bilayer," *J. Mater. Chem. A*, vol. 3, no. 38, pp. 19288–19293, 2015, doi: 10.1039/c5ta04239a.

[84] J. Yang, B. D. Siempelkamp, E. Mosconi, F. De Angelis, and T. L. Kelly, "Origin of the Thermal Instability in CH3NH3PbI3 Thin Films Deposited on ZnO," *Chem. Mater.*, vol. 27, no. 12, pp. 4229–4236, Jun. 2015, doi: 10.1021/ACS.CHEMMATER.5B01598.

[85] H. Ren, X. Zou, J. Cheng, T. Ling, X. Bai, and D. Chen, "Facile Solution Spin-Coating SnO2 Thin Film Covering Cracks of TiO2 Hole Blocking Layer for Perovskite Solar Cells," *Coatings 2018, Vol. 8, Page 314*, vol. 8, no. 9, p. 314, Sep. 2018, doi: 10.3390/COATINGS8090314.

[86] Y. Wang, L. Yang, C. Dall'Agnese, G. Chen, A. J. Li, and X. F. Wang, "Spray-coated SnO2 electron transport layer with high uniformity for planar perovskite solar cells," *Front. Chem. Sci. Eng. 2020 151*, vol. 15, no. 1, pp. 180–186, Mar. 2020, doi: 10.1007/S11705-020-1917-X.

[87] Y. Ko *et al.*, "Self-Aggregation-Controlled Rapid Chemical Bath Deposition of SnO2 Layers and Stable Dark Depolarization Process for Highly Efficient Planar Perovskite Solar Cells," *ChemSusChem*, vol. 13, no. 16, pp. 4051–4063, Aug. 2020, doi: 10.1002/CSSC.202000501.

[88] Q. Jiang, X. Zhang, and J. You, "SnO2: A Wonderful Electron Transport Layer for Perovskite Solar Cells," *Small*, vol. 14, no. 31, p. 1801154, Aug. 2018, doi: 10.1002/SMLL.201801154.

[89] Y. Li *et al.*, "Mesoporous SnO2 nanoparticle films as electron-transporting material in perovskite solar cells," *RSC Adv.*, vol. 5, no. 36, pp. 28424–28429, Mar. 2015, doi: 10.1039/C5RA01540E.

[90] E. H. Anaraki *et al.*, "Highly efficient and stable planar perovskite solar cells by solution-processed tin oxide," *Energy Environ. Sci.*, vol. 9, no. 10, pp. 3128–3134, 2016, doi: 10.1039/c6ee02390h.

[91] I. C. Smith, E. T. Hoke, D. Solis-Ibarra, M. D. McGehee, and H. I. Karunadasa, "A Layered Hybrid Perovskite Solar-Cell Absorber with Enhanced Moisture Stability," *Angew. Chemie Int. Ed.*, vol. 53, no. 42, pp. 11232–11235, Oct. 2014, doi: 10.1002/ANIE.201406466.

[92] H. Tsai *et al.*, "High-efficiency two-dimensional Ruddlesden–Popper perovskite solar cells," *Nat. 2016 5367616*, vol. 536, no. 7616, pp. 312–316, Jul. 2016, doi: 10.1038/nature18306.

[93] D. H. Cao, C. C. Stoumpos, O. K. Farha, J. T. Hupp, and M. G. Kanatzidis, "2D Homologous Perovskites as Light-Absorbing Materials for Solar Cell Applications," *J. Am. Chem. Soc.*, vol. 137, no. 24, pp. 7843–7850, Jun. 2015, doi: 10.1021/JACS.5B03796.

[94] K. Du *et al.*, "Two-Dimensional Lead(II) Halide-Based Hybrid Perovskites Templated by

Acene Alkylamines: Crystal Structures, Optical Properties, and Piezoelectricity," *Inorg. Chem.*, vol. 56, no. 15, pp. 9291–9302, Aug. 2017, doi: 10.1021/ACS.INORGCHEM.7B01094.

[95] Y. Chen, Y. Sun, J. Peng, J. Tang, K. Zheng, and Z. Liang, "2D Ruddlesden–Popper Perovskites for Optoelectronics," *Adv. Mater.*, vol. 30, no. 2, p. 1703487, Jan. 2018, doi: 10.1002/ADMA.201703487.

[96] C. C. Stoumpos *et al.*, "Ruddlesden–Popper Hybrid Lead Iodide Perovskite 2D Homologous Semiconductors," *Chem. Mater.*, vol. 28, no. 8, pp. 2852–2867, May 2016, doi: 10.1021/ACS.CHEMMATER.6B00847.

[97] L. N. Quan *et al.*, "Ligand-Stabilized Reduced-Dimensionality Perovskites," *J. Am. Chem. Soc.*, vol. 138, no. 8, pp. 2649–2655, Mar. 2016, doi: 10.1021/JACS.5B11740.

[98] G. Grancini and M. K. Nazeeruddin, "Dimensional tailoring of hybrid perovskites for photovoltaics," *Nat. Rev. Mater. 2018 41*, vol. 4, no. 1, pp. 4–22, Nov. 2018, doi: 10.1038/s41578-018-0065-0.

[99] Y. Huang *et al.*, "Stable Layered 2D Perovskite Solar Cells with an Efficiency of over 19% via Multifunctional Interfacial Engineering," *J. Am. Chem. Soc.*, vol. 143, no. 10, pp. 3911–3917, Mar. 2021, doi: 10.1021/JACS.0C13087.

[100] K. T. Cho *et al.*, "Selective growth of layered perovskites for stable and efficient photovoltaics †," 2018, doi: 10.1039/c7ee03513f.

[101] A. Q. Alanazi *et al.*, "Atomic-Level Microstructure of Efficient Formamidinium-Based Perovskite Solar Cells Stabilized by 5-Ammonium Valeric Acid Iodide Revealed by Multinuclear and Two-Dimensional Solid-State NMR," *J. Am. Chem. Soc.*, vol. 141, no. 44, pp. 17659–17669, Nov. 2019, doi: 10.1021/JACS.9B07381.

[102] N. Wei *et al.*, "5-Ammonium Valeric Acid Iodide to Stabilize MAPbI3 via a Mixed-Cation Perovskite with Reduced Dimension," *J. Phys. Chem. Lett.*, vol. 11, no. 19, pp. 8170–8176, Oct. 2020, doi: 10.1021/ACS.JPCLETT.0C02528.

[103] T. Zhang *et al.*, "Stable and Efficient 3D-2D Perovskite-Perovskite Planar Heterojunction Solar Cell without Organic Hole Transport Layer," *Joule*, vol. 2, no. 12, pp. 2706–2721, Dec. 2018, doi: 10.1016/J.JOULE.2018.09.022.

[104] Y. Zou, Y. Cui, H.-Y. Wang, Q. Cai, C. Mu, and J.-P. Zhang, "Highly efficient and stable 2D–

3D perovskite solar cells fabricated by interfacial modification," *Nanotechnology*, vol. 30, no. 27, p. 275202, Apr. 2019, doi: 10.1088/1361-6528/AB10F3.

[105] Y. Lin *et al.*, "Enhanced Thermal Stability in Perovskite Solar Cells by Assembling 2D/3D Stacking Structures," *J. Phys. Chem. Lett.*, vol. 9, no. 3, pp. 654–658, Feb. 2018, doi: 10.1021/ACS.JPCLETT.7B02679.

[106] A. H. Proppe *et al.*, "Multication perovskite 2D/3D interfaces form via progressive dimensional reduction," *Nat. Commun. 2021 121*, vol. 12, no. 1, pp. 1–9, Jun. 2021, doi: 10.1038/s41467-021-23616-9.

[107] M. S. Abbas *et al.*, "Orientationally engineered 2D/3D perovskite for high efficiency solar cells," *Sustain. Energy Fuels*, vol. 4, no. 1, pp. 324–330, Dec. 2019, doi: 10.1039/C9SE00817A.

[108] S. Jeong *et al.*, "Cyclohexylammonium-Based 2D/3D Perovskite Heterojunction with Funnel-Like Energy Band Alignment for Efficient Solar Cells (23.91%)," *Adv. Energy Mater.*, p. 2102236, 2021, doi: 10.1002/AENM.202102236.

[109] A. A. Sutanto *et al.*, "2D/3D perovskite engineering eliminates interfacial recombination losses in hybrid perovskite solar cells," *Chem*, vol. 7, no. 7, pp. 1903–1916, Jul. 2021, doi: 10.1016/J.CHEMPR.2021.04.002.

[110] R. Wang, M. Mujahid, Y. Duan, Z. Wang, J. Xue, and Y. Yang, "A Review of Perovskites Solar Cell Stability," *Adv. Funct. Mater.*, vol. 29, no. 47, p. 1808843, Nov. 2019, doi: 10.1002/adfm.201808843.

[111] S. Thampy, W. Xu, and J. W. P. Hsu, "Metal Oxide-Induced Instability and Its Mitigation in Halide Perovskite Solar Cells," *J. Phys. Chem. Lett.*, vol. 12, no. 35, pp. 8495–8506, Sep. 2021, doi: 10.1021/ACS.JPCLETT.1C02371.

[112] S. Ito, S. Tanaka, K. Manabe, and H. Nishino, "Effects of surface blocking layer of Sb2S3 on nanocrystalline TiO2 for CH3NH3PbI3 perovskite solar cells," *J. Phys. Chem. C*, vol. 118, no. 30, pp. 16995–17000, 2014, doi: 10.1021/jp500449z.

[113] N. Ahn *et al.*, "Trapped charge-driven degradation of perovskite solar cells," *Nat. Commun.*, vol. 7, no. 1, p. 13422, Dec. 2016, doi: 10.1038/ncomms13422.

[114] H. J. Jung, D. Kim, S. Kim, J. Park, V. P. Dravid, and B. Shin, "Stability of Halide Perovskite Solar Cell Devices: In Situ Observation of Oxygen Diffusion under Biasing," *Adv. Mater.*, vol.

30, no. 39, p. 1802769, Sep. 2018, doi: 10.1002/ADMA.201802769.

[115] J. Ji *et al.*, "Two-Stage Ultraviolet Degradation of Perovskite Solar Cells Induced by the Oxygen Vacancy-Ti4+ States," *iScience*, vol. 23, no. 4, p. 101013, Apr. 2020, doi: 10.1016/J.ISCI.2020.101013.

[116] Y. You, W. Tian, L. Min, F. Cao, K. Deng, and L. Li, "TiO 2 /WO 3 Bilayer as Electron Transport Layer for Efficient Planar Perovskite Solar Cell with Efficiency Exceeding 20%," *Adv. Mater. Interfaces*, vol. 7, no. 1, p. 1901406, Jan. 2020, doi: 10.1002/admi.201901406.

[117] Y. Lee *et al.*, "Efficient Planar Perovskite Solar Cells Using Passivated Tin Oxide as an Electron Transport Layer," *Adv. Sci.*, vol. 5, no. 6, Jun. 2018, doi: 10.1002/ADVS.201800130.

[118] M. Abuhelaiqa *et al.*, "Stable perovskite solar cells using tin acetylacetonate based electron transporting layers," *Energy Environ. Sci.*, vol. 12, no. 6, pp. 1910–1917, 2019, doi: 10.1039/c9ee00453j.

[119] Y. Lee *et al.*, "Enhanced charge collection with passivation of the tin oxide layer in planar perovskite solar cells," *J. Mater. Chem. A*, vol. 5, no. 25, pp. 12729–12734, Jun. 2017, doi: 10.1039/C7TA04128D.

[120] H. Kanda *et al.*, "Band-bending induced passivation: high performance and stable perovskite solar cells using a perhydropoly(silazane) precursor," *Energy Environ. Sci.*, vol. 13, no. 4, pp. 1222–1230, Apr. 2020, doi: 10.1039/C9EE02028D.

[121] H. Kanda *et al.*, "Gradient band structure: high performance perovskite solar cells using poly(bisphenol A anhydride-co-1,3-phenylenediamine)," *J. Mater. Chem. A*, vol. 8, no. 33, pp. 17113–17119, Aug. 2020, doi: 10.1039/D0TA05496H.

[122] N. Ahn *et al.*, "Trapped charge-driven degradation of perovskite solar cells," *Nat. Commun. 2016 71*, vol. 7, no. 1, pp. 1–9, Nov. 2016, doi: 10.1038/ncomms13422.

[123] P. Hang *et al.*, "An Interlayer with Strong Pb-Cl Bond Delivers Ultraviolet-Filter-Free, Efficient, and Photostable Perovskite Solar Cells," *iScience*, vol. 21, pp. 217–227, Nov. 2019, doi: 10.1016/j.isci.2019.10.021.

[124] N. Shibayama, H. Kanda, T. W. Kim, H. Segawa, and S. Ito, "Design of BCP buffer layer for inverted perovskite solar cells using ideal factor," *APL Mater.*, vol. 7, no. 3, p. 031117, Mar. 2019, doi: 10.1063/1.5087796.

[125] Q. Jiang *et al.*, "Surface passivation of perovskite film for efficient solar cells," *Nat. Photonics*, vol. 13, no. 7, pp. 460–466, Jul. 2019, doi: 10.1038/s41566-019-0398-2.

[126] P. Liu *et al.*, "Interfacial electronic structure at the CH3NH3PbI3/MoOx interface," *Appl. Phys. Lett.*, vol. 106, no. 19, p. 193903, May 2015, doi: 10.1063/1.4921339.

[127] W. Ke *et al.*, "Low-Temperature Solution-Processed Tin Oxide as an Alternative Electron Transporting Layer for Efficient Perovskite Solar Cells," *J. Am. Chem. Soc.*, vol. 137, no. 21, pp. 6730–6733, Jun. 2015, doi: 10.1021/JACS.5B01994.

[128] Ç. Kılıç and A. Zunger, "Origins of Coexistence of Conductivity and Transparency in SnO2," *Phys. Rev. Lett.*, vol. 88, no. 9, p. 095501, Feb. 2002, doi: 10.1103/PhysRevLett.88.095501.

[129] D. won Choi and J. S. Park, "Highly conductive SnO2 thin films deposited by atomic layer deposition using tetrakis-dimethyl-amine-tin precursor and ozone reactant," *Surf. Coatings Technol.*, vol. 259, no. PB, pp. 238–243, 2014, doi: 10.1016/J.SURFCOAT.2014.02.012.

[130] X. Chen, L. Li, Y. Xu, Y. Zhang, and G. Li, "Electron competitive migration regulating for dual maxima of water photolysis †," 2016, doi: 10.1039/c5ra23361e.

[131] Y. Lee *et al.*, "Efficient Planar Perovskite Solar Cells Using Passivated Tin Oxide as an Electron Transport Layer," *Adv. Sci.*, vol. 5, no. 6, Jun. 2018, doi: 10.1002/advs.201800130.

[132] Y. Lee *et al.*, "Enhanced charge collection with passivation of the tin oxide layer in planar perovskite solar cells," *J. Mater. Chem. A*, vol. 5, no. 25, pp. 12729–12734, Jun. 2017, doi: 10.1039/C7TA04128D.

[133] R. López and R. Gómez, "Band-gap energy estimation from diffuse reflectance measurements on sol–gel and commercial TiO2: a comparative study," *J. Sol-Gel Sci. Technol. 2011 611*, vol. 61, no. 1, pp. 1–7, Sep. 2011, doi: 10.1007/S10971-011-2582-9.

[134] T. Bu *et al.*, "Universal passivation strategy to slot-die printed SnO2 for hysteresis-free efficient flexible perovskite solar module," *Nat. Commun. 2018 91*, vol. 9, no. 1, pp. 1–10, Nov. 2018, doi: 10.1038/s41467-018-07099-9.

[135] C. Zuo *et al.*, "Crystallisation control of drop-cast quasi-2D/3D perovskite layers for efficient solar cells," *Commun. Mater. 2020 11*, vol. 1, no. 1, pp. 1–10, Jun. 2020, doi: 10.1038/s43246-020-0036-z.

[136] Y.-W. Jang *et al.*, "Intact 2D/3D halide junction perovskite solar cells via solid-phase in-plane

growth," *Nat. Energy 2021 61*, vol. 6, no. 1, pp. 63–71, Jan. 2021, doi: 10.1038/s41560-020-00749-7.

[137] C. Ma *et al.*, "2D/3D perovskite hybrids as moisture-tolerant and efficient light absorbers for solar cells," *Nanoscale*, vol. 8, no. 43, pp. 18309–18314, Nov. 2016, doi: 10.1039/C6NR04741F.

[138] J.-W. Lee *et al.*, "2D perovskite stabilized phase-pure formamidinium perovskite solar cells," *Nat. Commun. 2018 91*, vol. 9, no. 1, pp. 1–10, Aug. 2018, doi: 10.1038/s41467-018-05454-4.

[139] Z. Chen *et al.*, "Stable Sn/Pb-Based Perovskite Solar Cells with a Coherent 2D/3D Interface," *iScience*, vol. 9, pp. 337–346, Nov. 2018, doi: 10.1016/J.ISCI.2018.11.003.

[140] A. Mei *et al.*, "Stabilizing Perovskite Solar Cells to IEC61215:2016 Standards with over 9,000-h Operational Tracking," *Joule*, vol. 4, no. 12, pp. 2646–2660, Dec. 2020, doi: 10.1016/J.JOULE.2020.09.010.

[141] J. Chen, J.-Y. Seo, and N.-G. Park, "Simultaneous Improvement of Photovoltaic Performance and Stability by In Situ Formation of 2D Perovskite at (FAPbI3)0.88(CsPbBr3)0.12/CuSCN Interface," *Adv. Energy Mater.*, vol. 8, no. 12, p. 1702714, Apr. 2018, doi: 10.1002/AENM.201702714.

[142] H. Ren *et al.*, "Efficient and stable Ruddlesden–Popper perovskite solar cell with tailored interlayer molecular interaction," *Nat. Photonics 2020 143*, vol. 14, no. 3, pp. 154–163, Jan. 2020, doi: 10.1038/s41566-019-0572-6.

[143] X. Gao *et al.*, "Ruddlesden–Popper Perovskites: Synthesis and Optical Properties for Optoelectronic Applications," *Adv. Sci.*, vol. 6, no. 22, p. 1900941, Nov. 2019, doi: 10.1002/ADVS.201900941.

[144] M. C. Weidman, A. J. Goodman, and W. A. Tisdale, "Colloidal Halide Perovskite Nanoplatelets: An Exciting New Class of Semiconductor Nanomaterials," *Chem. Mater.*, vol. 29, no. 12, pp. 5019–5030, Jun. 2017, doi: 10.1021/ACS.CHEMMATER.7B01384.

[145] B.-E. Cohen, Y. Li, Q. Meng, and L. Etgar, "Dion–Jacobson Two-Dimensional Perovskite Solar Cells Based on Benzene Dimethanammonium Cation," *Nano Lett.*, vol. 19, no. 4, pp. 2588–2597, Apr. 2019, doi: 10.1021/ACS.NANOLETT.9B00387.

[146] M. Saliba *et al.*, "Incorporation of rubidium cations into perovskite solar cells improves

photovoltaic performance," *Science (80-.).*, vol. 354, no. 6309, pp. 206–209, Oct. 2016, doi: 10.1126/SCIENCE.AAH5557.

[147] N. J. Jeon *et al.*, "Compositional engineering of perovskite materials for high-performance solar cells," *Nat. 2015 5177535*, vol. 517, no. 7535, pp. 476–480, Jan. 2015, doi: 10.1038/nature14133.

[148] Lin Fu *et al.*, "A fluorine-modulated bulk-phase heterojunction and tolerance factor for enhanced performance and structure stability of cesium lead halide perovskite solar cells," *J. Mater. Chem. A*, vol. 6, no. 27, pp. 13263–13270, Jul. 2018, doi: 10.1039/C8TA02899K.

[149] I. Spanopoulos *et al.*, "Uniaxial Expansion of the 2D Ruddlesden–Popper Perovskite Family for Improved Environmental Stability," *J. Am. Chem. Soc.*, vol. 141, no. 13, pp. 5518–5534, Apr. 2019, doi: 10.1021/JACS.9B01327.

[150] J. M. Hoffman *et al.*, "From 2D to 1D Electronic Dimensionality in Halide Perovskites with Stepped and Flat Layers Using Propylammonium as a Spacer," *J. Am. Chem. Soc.*, vol. 141, no. 27, pp. 10661–10676, Jul. 2019, doi: 10.1021/JACS.9B02846.

[151] Y. Hua *et al.*, "Identification of the Band Gap Energy of Two-dimensional $(OA)_2(MA)_{n-1}Pb_nI_{3n+1}$ Perovskite with up to 10 Layers," *J. Phys. Chem. Lett.*, vol. 10, pp. 7025–7030, 2019, doi: 10.1021/ACS.JPCLETT.9B02823.

[152] Ming-Chun Tang *et al.*, "Unraveling the compositional heterogeneity and carrier dynamics of alkali cation doped 3D/2D perovskites with improved stability," *Mater. Adv.*, vol. 2, no. 4, pp. 1253–1262, Mar. 2021, doi: 10.1039/D0MA00967A.

[153] P. Chen, Y. Bai, S. Wang, M. Lyu, J.-H. Yun, and L. Wang, "In Situ Growth of 2D Perovskite Capping Layer for Stable and Efficient Perovskite Solar Cells," *Adv. Funct. Mater.*, vol. 28, no. 17, p. 1706923, Apr. 2018, doi: 10.1002/ADFM.201706923.

[154] T. Ming Koh *et al.*, "Enhancing moisture tolerance in efficient hybrid 3D/2D perovskite photovoltaics," *J. Mater. Chem. A*, vol. 6, no. 5, pp. 2122–2128, Jan. 2018, doi: 10.1039/C7TA09657G.

[155] H. Kim *et al.*, "Optimal Interfacial Engineering with Different Length of Alkylammonium Halide for Efficient and Stable Perovskite Solar Cells," *Adv. Energy Mater.*, vol. 9, no. 47, p. 1902740, Dec. 2019, doi: 10.1002/AENM.201902740.

[156] M. J. Paik, Y. Lee, H. S. Yun, S. U. Lee, S. T. Hong, and S. Il Seok, "TiO2 Colloid-Spray

Coated Electron-Transporting Layers for Efficient Perovskite Solar Cells," *Adv. Energy Mater.*, vol. 10, no. 39, p. 2001799, Oct. 2020, doi: 10.1002/AENM.202001799.

[157] V. L. Pool *et al.*, "Thermal engineering of FAPbI3 perovskite material via radiative thermal annealing and in situ XRD," *Nat. Commun. 2017 81*, vol. 8, no. 1, pp. 1–8, Jan. 2017, doi: 10.1038/ncomms14075.

Curriculum Vitae

Mousa Abuhelaiqa

Sion 1950, Switzerland

https://www.linkedin.com/in/mousa-abuhelaiqa/

mousa.abuhelaiqa@epfl.ch

https://www.researchgate.net/profile/Mousa-Abuhelaiqa

Education

07.2017 - 12.2021 **Materials Science and Engineering PhD**

Swiss Federal Institute of Technology, Lausanne (EPFL)

Thesis: Interface and Composition Engineering of High Performing
Perovskite solar cells

09.2015 - 09.2016 **Materials for Energy and Environment MSc**

University College London (UCL)

Thesis: Atomic Layer Deposition of Mesoporous TiO_2 on SBA15

08.2010 - 05.2015 **Mechanical Engineering BSc**

Texas A&M University at Qatar

Patented Capstone Design: Air Suspension Device and Air Suspension
System

Technical Skills

Characterization

Scanning electron microscopy (SEM), IV characteristics, powder x-ray diffraction (XRD), ultraviolet
photoelectron spectroscopy (UPS), x-ray photoelectron spectroscopy (XPS), Ultraviolet-visible
spectroscopy (UV-Vis), photoluminescence (PL), thermogravimetric analysis (TGA), nitrogen
porosimetry, ellipsometry.

Software

MATLAB, Microsoft Office, OriginLab Pro, Solidworks, Sketchup, Python, Mathematica
VESTA.

Professional Certifications

Diploma in French Language Studies (DELF) B1, French Ministry of Education
PRINCE2 Foundation Certification in Project Management, AXELOS

Publications, conferences, and patents

1. **Published article: M. Abuhelaiqa**, N. Shibiyuma, X. Gao, H. Kanda, M. Nazeeruddin, "SnO_2/TiO_2 Electron Transporting Bilayers: A Route to Light Stable Perovskite Solar Cells," ACS Applied Energy Materials, **2021**.

2. **Published article:** H. Kanda, O. Usiobo, C. Momblona, **M. Abuhelaiqa** *et al*, "Light stability enhancement of Perovskite Solar Cells Using 1H, 1H, 2H, 2H-perfluorooctyltriethoxysilane Passivation," Solar RRL, **2020**, 2000650, 1-7.

3. **Published article:** H. Kanda, N. Shibiyama, **M. Abuhelaiqa** *et al*, "Gradient band structure: high performance perovskite solar cells using poly(bisphenol A anhydride-*co*-1,3-phenylenediamine)," Journal of Materials Chemistry A, **2020**, 8, 17113-17119.

4. **Published article:** H. Kanda, N. Shibiyama, A. Huckaba, Y. Lee, S. Paek, N. Klipfel, C. Roldan, V. Queloz, G. Granici, Y. Zhang, **M. Abuhelaiqa** *et al*, "Band-bending induced passivation: high performance and stable perovskite solar cells using a perhydropoly(silazane) precurcor," Energy & Enviornmental Science, 2019, 12, 1910-1917.

5. **Published article: M. Abuhelaiqa** et al, "Stable perovskite solar cells using tin acetylacetonate based electron transporting layers," Energy & Enviornmental Science, **2019**, 12, 1910-1917.

6. **Poster presentation: M. Abuhelaiqa** "Passivated SnO_2 electron transporting layers based on acetylacetonate complexes" 4th International Conference on Perovskite Solar Cells and Optoelectronics, Lausanne, Switzerland, **2019.**

7. **Conference Presentation:** S. Paek, H. Kanda, Y. Zhang, H. Kim, Y. Lee, K. Cho, **M. Abuhelaiqa** et al "Stable perovskite solar cells by compositional and interface engineering," Materials Research Society of Serbia, Herceg Novi, Montenegro, **2019**.

8. **Accepted patent:** Al-Nuaimi, **M. Abuhelaiqa** *et al*, "Air suspension device and air suspension system." **2019**, Pub. No. WO/2019/203672.

9. **Conference paper and presentation:** J. Mondal, B. Azzam, **M. Abuhelaiqa** *et al*, "Active Tuned Mass Damper." 23rd Mediterranian Conference on Control and Automation (MED), **2015**, 1192-1197, Torremolinos, Spain.

Languages

Arabic: native language coherency

Engish: advanced coherency (C2)

French: upper-intermediate coherency (B2)